DESIGN AND DEVELOPMENT OF SYNTHETIC METHODOLOGIES FOR THE PREPARATION OF POROUS MATERIALS WITH ADVANCED FUNCTIONALITIES

A Dissertation

by

ERIC EMIL LEONHARDT

Submitted to the Office of Graduate and Professional Studies of
Texas A&M University
in partial fulfillment of the requirements for the degree of

DOCTOR OF PHILOSOPHY

Chair of Committee,	Karen L. Wooley
Committee Members,	Lei Fang
	Hong-Cai Zhou
	Jodie L. Lutkenhaus
Head of Department,	Simon W. North

May 2019

Major Subject: Chemistry

ABSTRACT

This work details the development of synthetic methodologies for the realization of porous materials with intricate design and meticulous control. A systematic approach is presented for the design and preparation of materials derived from cyclodextrins, tailored for advanced applications through synthetic control of the precursor functionality and linkage chemistry, and for the control of topography of porous materials through the utilization of sacrificial polymeric porogens. Two examples of these functional porous cyclodextrin-based materials are described, illustrating the efficacy of this approach in the preparation of materials with targeted activities and functionalities, and an example of the use of polymeric porogens to predictably induce porosity in thin films is presented.

The first example is a cyclodextrin polyimide (CDPI), designed for unique, flow-through molecular separation applications. These materials boasted high surface areas, extraordinary chemical and thermal stability, an ability to permit concurrent target compound immobilization and eluent mobility, and facile processing and utilization as bulk materials or films and coatings.

The second example is a cyclodextrin polyester (CDPE), devised for the loading and assembly of a polymeric hemostatic agent into bioabsorbable composite wound dressings. These materials demonstrated our ability to finely tune functionality of the material through control of the linkage chemistry, with full degradation observed under conditions emulating physiological milieu. Cyclodextrin polyesters were used as

sacrificial carriers for the assembly of chitosan into nanofibrous mats with high surface area. These composites exhibited remarkable hemostatic performance, when tested *in vivo* against commercial hemostatic dressings, and excellent biocompatibilities, with degradation observed after delivery to the wound site.

Lastly, we outlined a top-down technique for induced, tailored porosity in a chosen host material through the synthetic development of sacrificial polymeric porogen agents. Acid-sensitive bottlebrush polymers were blended and cast into films with a miscible, inert matrix polymer and selectively extracted, yielding thin films with imprinted surface topographies that could be predetermined through control of the brush topology.

ACKNOWLEDGEMENTS

CONTRIBUTORS AND FUNDING SOURCES

Contributors

This work was supervised by a dissertation committee consisting of Professor Karen L. Wooley (advisor) of the Departments of Chemistry, Chemical Engineering, and Materials Science and Engineering; Prof. Lei Fang (committee member) of the Departments of Chemistry and Materials Science and Engineering; Prof. Hong-Cai Zhou (committee member) of the Departments of Chemistry and Materials Science and Engineering; and Prof. Jodie. L. Lutkenhaus (committee member) of the Department of Chemical Engineering.

This work was facilitated through use of the Texas A&M Laboratory for Synthetic Biologic Interactions and the Texas A&M University Materials Characterization Facility.

In Chapter II, SEM images were obtained by Dr. Linda S. McCorkle at the Ohio Aerospace Institute and Nari Kang of the Department of Materials Science and Engineering at Texas A&M University. Gas sorption isotherms were obtained by Sai Che of the Department of Chemistry at Texas A&M University. Solid-state NMR spectra were obtained by Dr. Vladimir I. Bakhmutov of the Department of Chemistry at Texas A&M University. Supercritical drying of samples was performed by Dr. Stephanie Vivod of the NASA Glenn Research Center. Equipment for sorption studies was provided by Michael Flynn of the NASA Ames Research Center. Additional

equipment was provided by Dr. Tiffany S. Williams of the NASA Glenn Research Center and Dr. Mary Ann Meador of the NASA Glenn Research Center.

In Chapter III, SEM images were obtained by Yordanos Bisrat of the Materials Characterization Facility at Texas A&M University and Nari Kang of the Department of Materials Science and Engineering at Texas A&M University. *In vivo* studies were performed by Dr. Mahmoud Elsabahy of the Department of Chemistry at Texas A&M University and the Department of Pharmaceutics and Assiut International Center of Nanomedicine at Al-Rajhy Liver Hospital of Assiut University, with design input from Dr. Mostafa A. Hamad of the Department of Surgery of the Faculty of Medicine at Assiut University. Solid-state NMR spectra were obtained by Dr. Vladimir I. Bakhmutov of the Department of Chemistry at Texas A&M University. PXRD data was obtained by Dr. Joseph H. Reibenspies of the Department of Chemistry at Texas A&M University.

In Chapter IV, cluster SIMS data was obtained by Dr. Michael Eller. Film thickness measurements were performed by Nari Kang.

All other work conducted for this dissertation was completed independently.

Funding Sources

NOMENCLATURE

AA	Acrylic acid
AcOH	Acetic acid
Ac_2O	Acetic anhydride
AFM	Atomic force microscopy
AIBN	Azobisisobutyronitrile
ATR	Attenuated total reflectance
BBY	Bismarck brown Y
BET	Brunauer–Emmett–Teller
BPDA	3,3'4,4'-Biphenyltetracarboxylic acid dianhydride
CD	Cyclodextrin
CDPE	Cyclodextrin polyester
CDPI	Cyclodextrin polyimide
CG	Cardiogreen
CHMA	Cyclohexyl methacrylate
CP-MAS	Cross-polarization magic angle spinning
DCM	Dichloromethane
DLS	Dynamic light scattering
DMF	Dimethylformamide
DMSO	Dimethylsulfoxide
ECPMA	1-Ethylcyclopentyl methacrylate

Et$_3$N	Triethylamine
FG	Functional group
FNa	Fluorescein sodium
FTIR	Fourier-transform infrared
HCl	Hydrochloric acid
KOH	Potassium hydroxide
MeOH	Methanol
MV2B	Methyl violet 2B
NLDFT	Nonlocal density functional theory
NMP	N-methylpyrrolidinone
NMR	Nuclear magnetic resonance
PMDA	Pyromellitic dianhydride
PPh$_3$	Triphenylphosphine
PPIX	Protoporphyrin IX
PTSA	p-Toluenesulfonic acid
PVDF	Polyvinylidene fluoride
PXRD	Powder X-ray diffraction
RhB	Rhodamine B
RB	Rose Bengal
RPM	Rotations per minute
SEC	Size-exclusion chromatography
SEM	Scanning electron microscopy

SIMS	Secondary ion mass spectrometry
SS	Solid-state
TMAH	Tetramethylammonium hydroxide
UV-Vis	Ultraviolet-visible
UV-O_3	Ultraviolet-ozone

TABLE OF CONTENTS

LIST OF FIGURES

LIST OF TABLES

CHAPTER I

INTRODUCTION

1.1   Porous Materials Today

One of the most remarkable characteristics of the physical world is the vast amount of void space, extending far beyond the boundaries of what is directly observable. The overwhelming majority of the universe, as we understand today, is effectively vacuum, with as much as 90% of its composition attributed to empty space.[1] At the other extreme, the apparent volume of the atom that can be attributed to its substituent subatomic particles is strikingly low.[2] Between these two points exists a broad scale of void space that is accessible by particulate matter, termed porosity, and is therefore particularly relevant to materials of the natural world, affecting important properties such as permeability and density. Materials with porosity on all scales can be found in nature, from honeycomb and sponges to cuttlebone[3] and zeolites.[4] Nanoporous materials, which can be further subdivided into microporous (average pore size <2 nm), mesoporous (2–50 nm), and macroporous (50–1000 nm) materials, are critical to an expansive range of industries, spanning micro- and optoelectronics,[5] molecular separations[6-7] and storage,[8-11] biomedicine,[12] environmental remediation,[13] and food packaging,[14] insulating,[15] and dielectric materials.[16] Nanoporous materials are therefore among the most widely studied of all materials, and a far-reaching interdisciplinary

effort has been devoted to the development of new porous materials with novel functionalities that will enable specialized, targeted applications.

The manifestation of porosity in materials can be broadly categorized into two categories: inherent porosity and induced porosity. Inherent porosity, which is permanent and intrinsic to the architecture of the molecular network structure, is demonstrated in materials such as in metal–organic frameworks (MOFs),[17] covalent organic frameworks (COFs),[18-19] and polymers of intrinsic microporosity (PIMs).[20] Induced porosity, generated in compatible materials by various processing techniques, can be achieved by the addition of porogens,[21] carbonization,[22] foaming,[23] and others.[24] In the pursuit of novel, advanced functional materials, synthetic polymer chemistry provides a critical vantage point at the interface between the synthesis of new, inherently porous materials and the development of novel techniques to induce porosity. Furthermore, it provides a basis to evaluate the viability of the subsequent utilization of these materials.

While there is a perpetual investigation at the frontier of chemistry to devise new materials and methods, scrutiny must be placed on compatibility with existing industrial processing methods and feasibility of scale to develop economically practicable solutions to real market needs. Concurrently, there is a strong emphasis on technologies with increased sustainability, and materials comprising naturally derived building blocks from renewable feedstocks are thus an attractive target. This work aims to address the need for functional porous materials by solutions that are scalable and processable, with sustainable production and performance, and is divided into two main sub-directives:

a)the establishment of systematic synthetic methodologies for the production of functional, porous materials derived from cyclodextrins and b)the development of top-down techniques for induced, tailored porosity in materials by the synthesis of novel polymeric porogen agents. Through these methods, we expected to achieve a synthetic platform facilitating the preparation of functional, porous materials with finely tuned structures, chemical properties, and activities.

1.2   Functional, Porous Materials Derived from Cyclodextrins

Cyclodextrins are a group of naturally derived, macrocyclic sugars that provide a versatile synthetic platform *via* selective functionalization of their many primary and secondary hydroxyl groups.   These hollow cyclodextrins can, themselves, be conceptualized as porous, and have long been studied for their interesting properties and sorption behavior. Of particular interest is the seven-membered isomer, β-cyclodextrin (Figure I.1), which is the most studied isomer for its sorptive activity. As the most abundant of the cyclodextrins, it is also the most cost-effective at *ca.* 1 USD kg^{-1}.[25] These toroidal compounds have a hydrophilic shell that encompasses a hydrophobic interior, imparting the sub-nanometer cavities with a powerful affinity for guest molecules with shape and chemical specificity. This feature has been utilized in the reversible capture of target compounds, which has proven useful for the immobilization of air and waterborne contaminants and in the chromatographic separation of isomers and homologues.[26-28] This work focuses on the use of the β-cyclodextrin isomer as an

3

active building block, as the most cost-effective template for proof-of-concept, but is also relevant to the 6- and 8-membered isomers (α and γ, respectively).
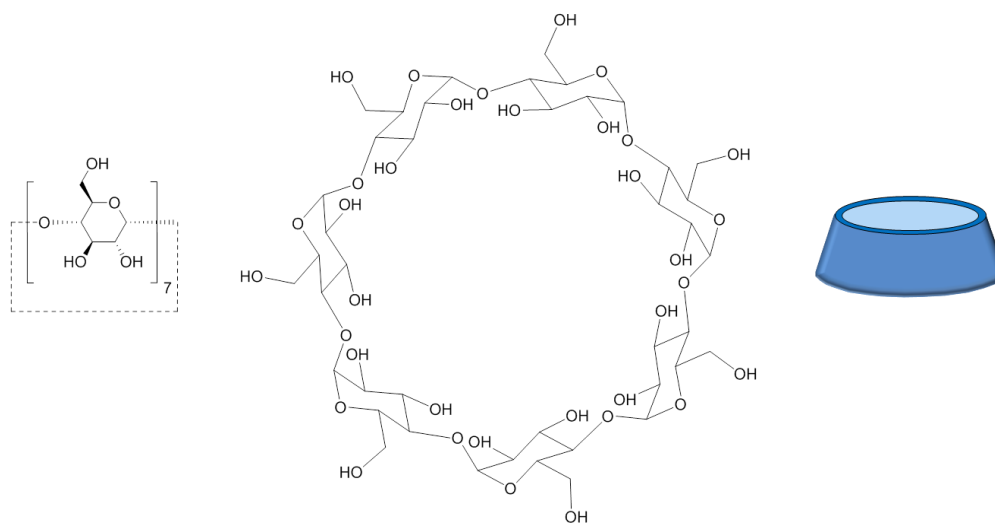
Figure I.1. Structural representations of β-cyclodextrin (left, middle) and illustrated depiction of its toroidal character (right).

Many synthetic strategies have been employed for the incorporation of cyclodextrin into polymeric materials as grafted pendant groups,[29] as initiators[30-31] and as monomers in both step-growth[32] and chain-growth polymerizations.[33] The host–guest activity of the cyclodextrin provides the resulting polymers with unique activities, and has found utility in self-healing coatings,[33] drug-delivery,[34] environmental remediation,[25] and others.[35] In some cases, this inclusion complex-forming behavior, itself, is used in the macromolecular assembly of these materials, where cyclodextrins are threaded with linear polymers and end-capped to form psuedorotaxanes[36] (Figure I.2) or slide-ring gels[37] with robust and interesting mechanical properties. As such, cyclodextrins offer marked versatility in both the functionality and assembly of polymeric materials.

The selective installation of functional groups provides a method to finely tune the host selectivity of these cyclodextrins,[38] and the introduction of polymerizable moieties enables the formation of polymers with predetermined chemical linkages and macromolecular architectures. To this end, the appropriate synthetic toolkit is critical in obtaining cyclodextrin-derived materials with diverse structures and tailored chemical properties. Of the multitude of potential materials, those with inherent and permanent
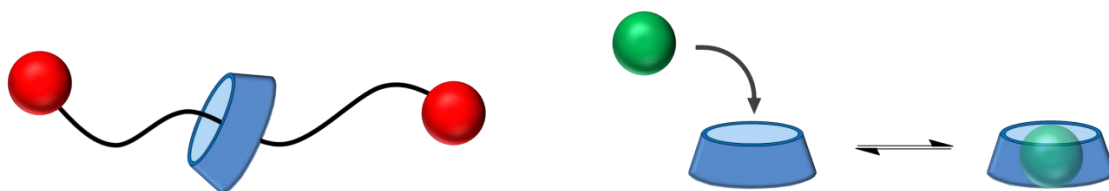
Figure I.2. Simplified illustration of select, interesting properties of cyclodextrins: polymer-threading and end-capping to form pseudorotaxanes (left) and reversible inclusion complex formation with compatible molecular hosts (right).

porosity are of considerable interest and are particularly elusive. The inclusion of cyclodextrin into a porous framework was demonstrated to greatly enhance its efficacy of action, enhancing the rate of contaminant immobilization in sorbents for water purification by increasing the availability of the active sites within the material.[25] However, the realization of such materials presents unique challenges both synthetically and in their subsequent processing and utilization. To maximize functionality, the concentration of cyclodextrin in the material should also be maximized, necessitating the construction of the porous framework from the cyclodextrin itself, rather than as a pendant group or additive. This work seeks to outline synthetic strategies to devise hierarchically porous, processable, cyclodextrin-based polymeric materials, and to

5

demonstrate their efficacy for environmental remediation and biomedical applications, among others.

1.3   Polymeric Porogen Agents for Introduction of Porosity in Thin Films

Though the development of novel, inherently porous materials is a critical and necessary directive, overarching control of the pore topography in these materials is often a significant challenge. Typically, only discrete morphologies are allowed by the molecular network architecture of each material, and though modification of the monomer geometries can yield fine control over the pore shapes and dimensions, the need to develop unique formulations for each minor adjustment to the pore topography can prove taxing. Furthermore, control of the overall porosity, or the volume fraction of the material corresponding to void space, of the resulting materials is limited. The use of sacrificial pore forming agents, in which a sacrificial component is blended with a chosen matrix and selectively extracted to yield an imprinted network of voids, offers the ability to tailor both the pore morphology and overall porosity of a chosen matrix material through control of the shape and weight fraction of the added porogen. To this end, a material can be designed from a chosen matrix polymer, with its porosity then tailored through the use of sacrificial porogens without the need for further modifications to the matrix polymer.

The use of porogenic agents has been widely studied, in which the morphology of the material is templated through control of the sacrificial porogen. This imprinting

strategy is particularly attractive for thin films, in which the topography is integral to their application as dielectric materials,[39-41] antireflective coatings,[42-43] membranes,[44] and transistor nanotemplates.[45-47] A great range of pore size control is possible, from the use of large spherical pores generated from dendritic porogens[48] to sub-2 nm pores generated from cyclodextrins,[49-51] and shape control is also possible, in which the topology of the sacrificial porogen is imprinted with reasonable fidelity.[52] The porosity can be controlled through the amount of porogen added,[53] with one key caveat: selective extraction of the porogen from the matrix generally necessitates some degree of phase incompatibility between the two domains that can cause heterogeneity in precursor films, resulting in a deviation from the expected topographies at larger concentrations of porogen, as complex morphologies arise.[53]

The use of a miscible porogen has been explored to great effect,[54] in which precursors were cast into homogeneous films before cross-linking of the matrix, then allowing selective removal of the non-cross-linked component. This approach, analogous to the negative tone techniques widely used in photoresist technology,[55] enables kinetic trapping of the porogen in the miscible state before chemical modification of the matrix and selective removal of the sacrificial porogenic domain. Positive tone systems, where chemical modification is, instead, performed on the porogenic domain to modulate its solubility, may be even more attractive as it enables use on many different matrix polymers. Earlier work in our group has detailed the synthesis of architecturally-intricate bottlebrush polymers that are capable of controlled alignment and solubility modulation through reactive monomer units. These bottlebrush

7

systems are expected to provide a powerful tool for the introduction of tailored porosity in host materials, where homogeneous distribution of these brushes throughout an inert matrix allows the formation of predictable topographies through control of the volume fraction, molecular topology, and chemical properties of the sacrificial brush domain.

CHAPTER II

β-CYCLODEXTRIN-DERIVED MONOLITHIC, HIERARCHICALLY POROUS

POLYIMIDES DESIGNED FOR VERSATILE MOLECULAR SEPARATION

APPLICATIONS[*]

2.1   Introduction

Cyclodextrins have long been studied in the field of separation science,[28, 56-61] and have gained considerable attention recently for their performance in environmental remediation-based applications.[25-26, 62-63] These naturally derived cyclic sugars are well known to reversibly form inclusion complexes with suitable guests, and reversibly bind compounds with shape and chemical specificity in their hydrophobic cavities.[56] Of these, the seven-membered β-cyclodextrin is both the most abundant and studied isomer for water treatment applications, in which organic model contaminants can be captured and removed from water and subsequently released when rinsed with an adequate solvent, thus easily regenerating the active cavities.[62] In an industry dominated by activated carbon, in which the single largest barrier of its use lies in the difficulty associated with its regeneration,[64] a large interdisciplinary effort has been devoted to the investigation of new materials with unique sorption and desorption mechanisms.[65]

Cyclodextrins have been employed similarly in a wide range of other separation-based applications, such as in the encapsulation of odorous compounds from air[27] and the separation of positional isomers and enantiomers,[28] resulting in an extensive drive to develop cyclodextrin-based materials. Of particular interest is their incorporation into porous materials, which increases the availability of the active cyclodextrin moieties and aids diffusion of the mobile phase through the material, therefore enhancing their separation efficiency.[25, 66] However, current literature methods to produce porous cyclodextrin-linked polymers can require long reaction times, up to 2 d, and custom-synthesized cross-linkers. Most importantly, the resulting product is an insoluble powder, a hindrance in its use in particular applications, such as coatings and energy-efficient membrane-based separations.

Cyclodextrin incorporation into film-based materials has been achieved by physical blending,[67-71] surface modification,[72-74] chemical incorporation into the polymeric precursors,[75] or a combination thereof.[76] By these preparation methods, however, the resulting concentrations of the active cyclodextrin groups have remained relatively low, thereby reducing their effect in the resulting material. Continuous films formed entirely from cyclodextrins and a small-molecule linker by an interfacial polymerization process have been reported recently.[77-78] Although these materials didn't exhibit the traditional mode of selectivity by contaminant immobilization within the cyclodextrin groups, compounds capable of travelling through the cavity were allowed to pass. By this process, these materials offer an alternative mechanism of shape and size-specific discrimination for molecular sieving applications.

It was hypothesized that a monolithic cyclodextrin-derived material with hierarchical porosity would impart the advantages of a moldable material while maintaining the interesting contaminant immobilization behavior, by simultaneously allowing inclusion-complex formation and flow of the mobile phase throughout the solid matrix. Moreover, the direct connection of cyclodextrins *via* imide-based linkers was expected to afford high concentrations of the active cyclodextrin cavities distributed throughout a porous matrix material, as cross-linked polyimides are known to form highly porous gels that can be cast in molds or as films and can be produced on a large scale.[79-83] Polyimides, having extraordinary chemical, thermal, and physical robustness, are also attractive because they have been previously demonstrated to exhibit mesoporosity[81-82] and are widely used in separation technologies—currently constituting the largest class of organic solvent-resistant nanofiltration membranes.[84-85] The selective conversion of the primary alcohols in cyclodextrins to amines[86] was targeted as a route to establish polyimides upon reaction with anhydride groups. The seven-membered isomer (β-CD-NH$_2$), and similar members of this group of cyclodextrin derivatives, has been investigated with respect to separation technologies, demonstrating similar sorption activity to the native β-cyclodextrin.[38, 87-89] Materials comprising β-CD-NH$_2$ have been afforded by supramolecular assembly[90-91] and grafting-to approaches.[92] Recently, the direct copolymerization of β-CD-NH$_2$ has been reported in the formation of an imine-linked covalent organic framework.[93] Other polymer-forming amine-functionalized cyclodextrin derivatives have been studied, such as tethered monomers,[94-95] monofunctional initiators,[96] and symmetric difunctionalized β-cyclodextrin[97]—however,

11

difficulty in obtaining isolated regioisomers prohibits their large-scale production. Thus, β-CD-NH$_2$ was deemed the most suitable building block in the pursuit of a cyclodextrin-based polyimide.

2.2 Results and Discussion

In this work, it was found that the easily obtained peraminated β-CD-NH$_2$ could be readily polymerized with pyromellitic dianhydride (PMDA) to rapidly form a highly cross-linked network when solubilized in polar aprotic solvents with the addition of a small amount of acetic acid (0.35 mL per 100 mg β-CD-NH$_2$) (Figure II.1). Gels were obtained in as little as 1 min, and partial chemical imidization could then be achieved by soaking the gel in a mixture of acetic anhydride (Ac$_2$O) and triethylamine (Et$_3$N). Initial qualitative screening studies indicated that the relative stoichiometries of β-CD-NH$_2$ to pyromellitic dianhydride affected the ability to produce well-defined cross-linked gel materials. At too low anhydride:amine, gelation did not occur and at too high anhydride:amine, the reaction mixture quickly underwent phase segregation to result in inhomogeneous domains of cross-linked material interspersed with undissolved and unreacted pyromellitic dianhydride powder. However, at a β-CD-NH$_2$ to pyromellitic dianhydride stoichiometry of 2.75:1, which corresponded to 5.5 anhydrides per 7 amines, a balance was attained between homogeneous mixing and formation of a continuous cross-linked gel. The resulting cyclodextrin polyimide (CDPI) was prepared in bulk, in cylindrical molds from 12 *wt.* % solutions in NMP and acetic acid (11:5 *v/v*) with 2.75 *equiv*. PMDA. After gelation, the samples were briefly heated to 70 °C for 10

12

min to further encourage cross-linking before soaking the solid gels in a small amount of

DMF/Ac$_2$O/Et$_3$N (8:2:5 *v/v*) for 1.5 h to promote imidization. Gels were exchanged into

clean DMF, followed by methanol to remove unreacted reagent and byproducts.

Samples could then be dried supercritically with carbon dioxide or exchanged into water

and lyophilized for characterization.
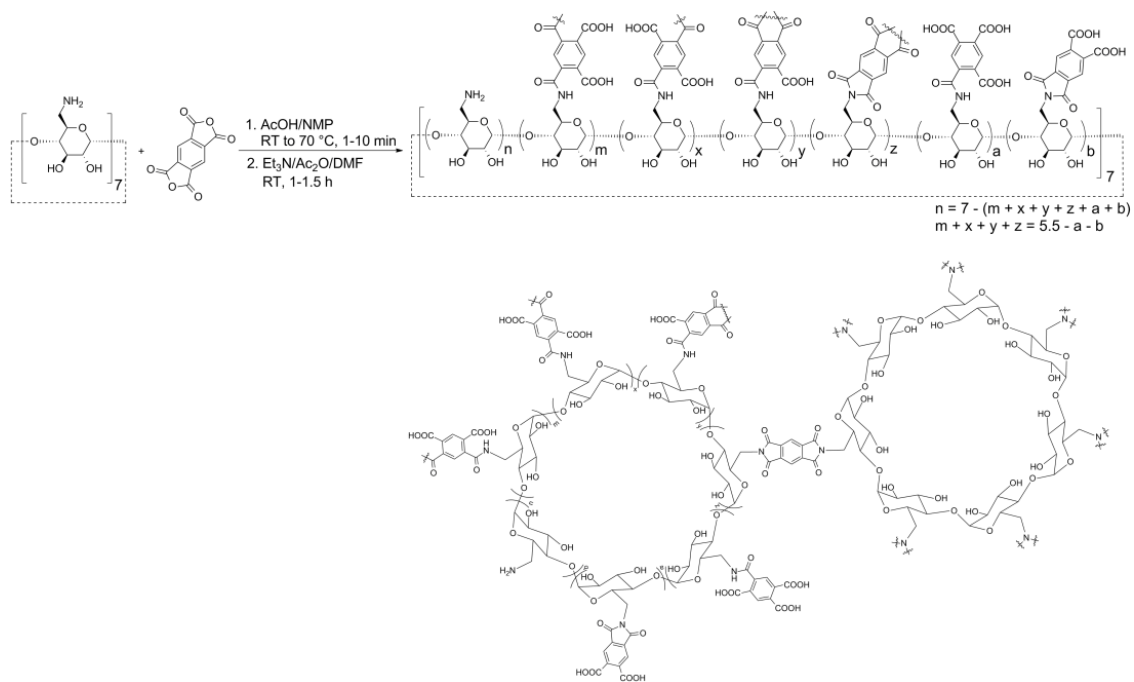
Figure II.1. Overview of the synthesis of CDPI (top) with an expanded illustration of
the diversity of potential linkages and structural components (bottom).

Analysis of nitrogen adsorption/desorption at 77 K (Figure II.2) of CDPI

revealed a Langmuir surface area of 155 m^2 g^{-1} and a Type IV isotherm, indicating the

presence of mesoporosity in the material signified by the sorption/desorption hysteresis.

The pore size distribution, calculated by nonlocal density functional theory modeling

13

(NLDFT), indicated a peak at the lower bound of detection, centered at 1.5 nm, as well as a broad distribution of mesopores. We reason that π–π stacking of the PMDA linkages in the hyperbranched network may result in the formation of mesoporous channels, such as those seen in other mesoporous polyimides, with relatively broader pore size distributions than those exhibited by linear polyimides having more well-defined packing. Large macroporous voids generated by the evacuation of the mesh space of the gel network could be viewed by scanning electron microscopy (SEM) (Figure II.3), confirming the desired hierarchical porosity of the material. In contrast to the mesoporosity of CDPI, determined by the polymer structure, its macroporosity is primarily dictated by the gel structure, controlled by the relative amount of solvent used during preparation. Gels prepared at lower weight fractions yielded materials with a higher theoretical total porosity at the cost of increasing fragility, and thus 12 *wt.* % was chosen to optimize porosity while ensuring sufficient mechanical strength of the material to allow handling without fracturing. Though the large macropores were not expected to
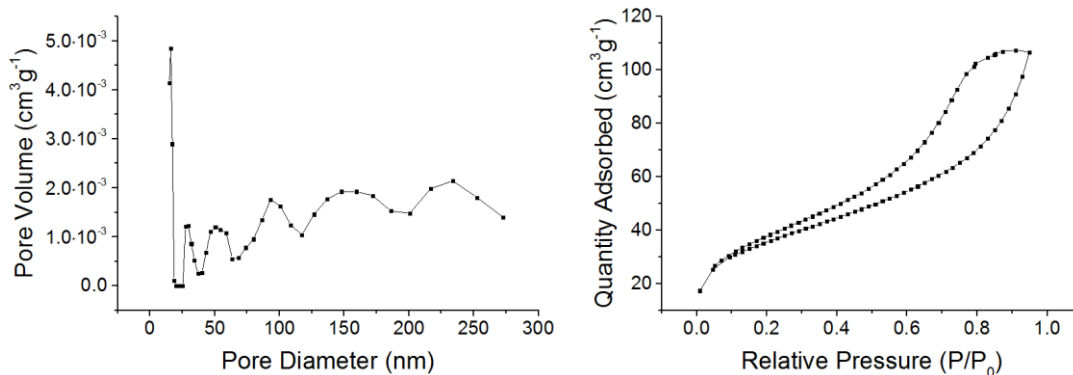
Figure II.2. N_2 sorption/desorption isotherm at 77 K (left) and NLDFT pore size distribution (right) for CDPI.

14

directly contribute to sorption activity, they were desired to provide ample mobility in the continuous framework as target compounds interact with the mesoporous channels and cyclodextrin cavities.
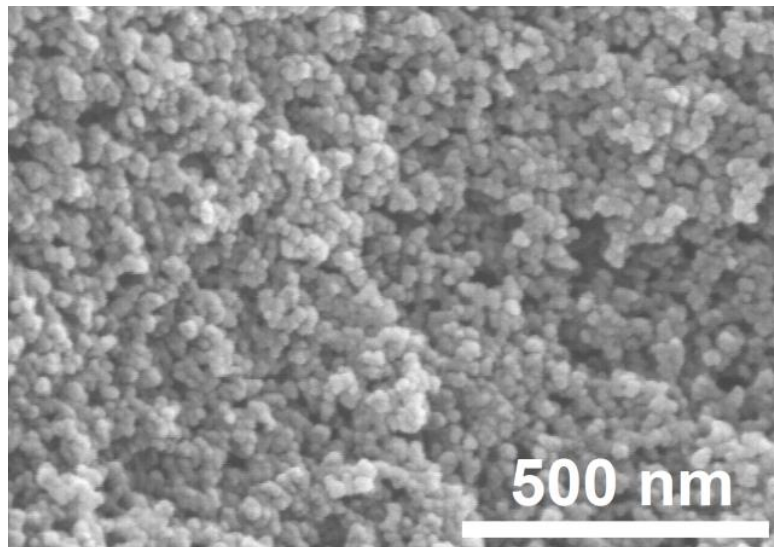
Figure II.3. SEM image of CDPI.

Solid-state characterization techniques were employed to investigate the chemical composition of CDPI. Examination of the Fourier-transfer infrared (FTIR) spectrum (Figure II.4) revealed the presence of both the imide linkage at 1723 cm^{-1} as well as the ring-opened amic acid linkage at 1653 cm^{-1}, indicating incomplete imidization of the network—typical of chemical curing methods.[98] Though these more chemically labile linkages could promote sensitivity to hydrolysis, the material exhibited excellent chemical stability. CDPI was found to be macroscopically stable indefinitely in water, 4 M HCl aqueous solution, and all tested organic solvents. However, the bulk

material underwent slow disintegration in 4 M KOH aqueous solution over the course of 2 d, forming a suspension of small particles.

To validate the utility of CDPI for molecular separations, liquid-phase adsorption was studied for several model compounds at a concentration of 1 mg CDPI per mL of feed solution to analyze performance of the material as a sorbent (Figure II.5). As cyclodextrins are known to bind with hydrophobic guests in aqueous solutions, several shape-compatible water soluble dyes with hydrophobic aryl groups were chosen for analysis: Bismarck brown Y (BBY), methyl violet 2B (MV2B), and rhodamine B (RhB). Similar to previous examples of porous cyclodextrin polymers,[25] the rate of adsorption was found to be extraordinarily fast, with over 80% uptake efficiency achieved in 15 s and equilibrium achieved in as little as 2 min, reinforcing the notion that the availability of cyclodextrin groups within the porous framework facilitates sorption performance. Adsorption isotherms, used to predict the maximum adsorption capacity and to attempt to quantify the role of cyclodextrin groups in the immobilization of model compounds, were fit to the Langmuir model (Table II.1):[65]

$$q_e = \frac{Q_0 b C_e}{1 + b C_e} \quad (1)$$

where q_e (mg g^{-1}) is the adsorbate concentration at equilibrium; Q_0 (mg g^{-1}) is the maximum monolayer coverage capacity; b (dm^3 mg^{-1}) is the Langmuir isotherm constant; and C_e (ppm) is the equilibrium concentration of the adsorbate measured by UV-vis spectroscopy. Interestingly, despite CDPI exhibiting a similar molar adsorption capacity for each dye when accounted for molecular weight, adsorption of BBY and MV2B at lower concentrations was relatively more effective. The relative capacities for

16

molecules of dye adsorbed per molecules of cyclodextrin suggested by this model are 2.4, 2.6, and 2.4 for BBY, MV2B, and RhB, respectively—implying contaminant uptake beyond inclusion complex formation alone, conceivably by hydrogen bonding or physical adsorption in the mesoporous channels of the material, as has been observed in other cyclodextrin-based sorbent materials.[60] The maximum RhB absorption capacity (621 mg g^{-1}) was significantly larger than that of many activated carbons (*ca*. 35 mg g^{-1}),[99] and was comparable with covalent organic frameworks (625 mg g^{-1}) of relatively larger surface areas than CDPI.[100] Regeneration of the saturated material could be easily achieved by rinsing with a small amount of methanol followed by rinsing with water, resulting in the disappearance of color from the material. No substantial loss in performance was observed after four regeneration cycles (Figure II.6).

Adsorption of other various model compounds were also explored (Table II.2). As seen in similar materials, the charge of the model compound studied seemed to play a significant role in uptake selectivity.[77] It was found that CDPI exhibited a strong preference for cationic adsorbates, with modest adsorption of the neutral toluene species and almost no adsorption for the studied anionic dyes. This sorption behavior is distinct from the selectivity displayed by native β-CD-NH$_2$,[38] perhaps due to the presence of amic acid groups in the material influencing the ionic behavior. Peculiarly, protoporphyrin IX (PPIX) disodium salt, chosen as a model compound with sufficient steric bulk to prevent entry into the cavity of the cyclodextrin groups, was the only anionic compound that was adsorbed by CDPI, albeit with significant less uptake than the studied neutral and cationic species. This discrepancy may be due to the increased

likelihood for the relatively bulkier PPIX molecules becoming immobilized in other sites of the porous network over the smaller anionic adsorbates.

Table II.1. Adsorption isotherm parameters for Langmuir model.

Dye	Q_0 (mg g^{-1})	b (dm^3 mg^{-1})	R_L^2
BBY	554	0.13	0.966
MV2B	559	0.20	0.937
RhB	621	0.01	0.992

The versatility afforded by the casting process of CDPI is a key advantage in augmenting the scope of cyclodextrin-derived materials, *e.g.* separations in film and coating-based settings. To demonstrate the potential for molecular separations in the film-state, CDPI was cast as a film, *ca.* 20 µm thick, and analyzed as a liquid filtration membrane (Figure II.7). The gel was applied to a microfiltration support (PVDF, 5.0 µm pore size) and pressed with a rubber roller to uniformly coat the surface with a thin layer. The physically supported films were imidized analogously to the bulk monolithic samples by soaking for 1 h in the curing solution after briefly heating for 1 min at 70 °C. To quantify permeance and adsorption, separation experiments were performed in a dead-end configuration, braced by a porous metal disk in a stainless steel stirred cell (effective membrane area 14.6 cm^2). The coated membranes revealed dramatically diminished solvent permeances when compared with the native ultrafiltration support, and remained stable at feed pressures up to 4.8 bar without a measureable change in flux over the duration of experiments (up to 4 h), suggesting resistance to crack formation

and disintegration during use. Though the polymer contained both hydrophobic and hydrophilic domains, the films demonstrated a strong preference for hydrophilic solvents, water (6.5 L m^{-2} h^{-1} bar^{-1}) and methanol (8.8 L m^{-2} h^{-1} bar^{-1}), over nonpolar solvents, such as *n*-hexane (0.3 L m^{-2} h^{-1} bar^{-1}). Permeance appeared to be dependent to a lesser degree upon solvent viscosity, with a lower viscosity reasonably corresponding to a higher flux for solvents with similar polarity indices (Figure II.8, Table II.4). In dye separation experiments, complete adsorption of RhB at environmentally relevant feed concentrations was demonstrated, with no detectable RhB observed in the volume of filtrate collected (150 mL). At higher feed concentrations, however, breakthrough could be observed as the vacant adsorption sites were depleted in the material, as expected (Figure II.9).

In addition to liquid-phase separations, CDPI was also expected to exhibit gas-phase adsorption of target compounds. Even at ambient pressures, mobility of gas throughout the macroporous framework was expected, considering the much smaller mean free path of air relative to the dimensions of the macropores. When exposed for 4 h to toluene vapors, 59 mg g^{-1} was loaded into the material, corresponding to 1.2 toluene molecules adsorbed per cyclodextrin group, thus demonstrating the potential to interact with airborne contaminants, necessary for the immobilization of odorous compounds from air, gas chromatography, and other applications.

In summary, we have demonstrated the preparation of a β-cyclodextrin-derived monolithic material with hierarchical porosity and excellent chemical stability that can be cast as monolithic molds or as thin films by convenient and scalable processes. Their

potential for molecular separations was confirmed by rapid gas and liquid-phase adsorption of model compounds, and the separation activity of the material was demonstrated to operate both in bulk and when cast as a supported membrane coating. It is expected that the versatility and chemical stability imparted by this robust, porous polyimide framework, with functionality provided by its large cyclodextrin concentration, will facilitate the expanded implementation of cyclodextrin-derived materials in a diverse range of separation applications, *e.g.* chemical sensing, chromatographic separation, and environmental remediation.
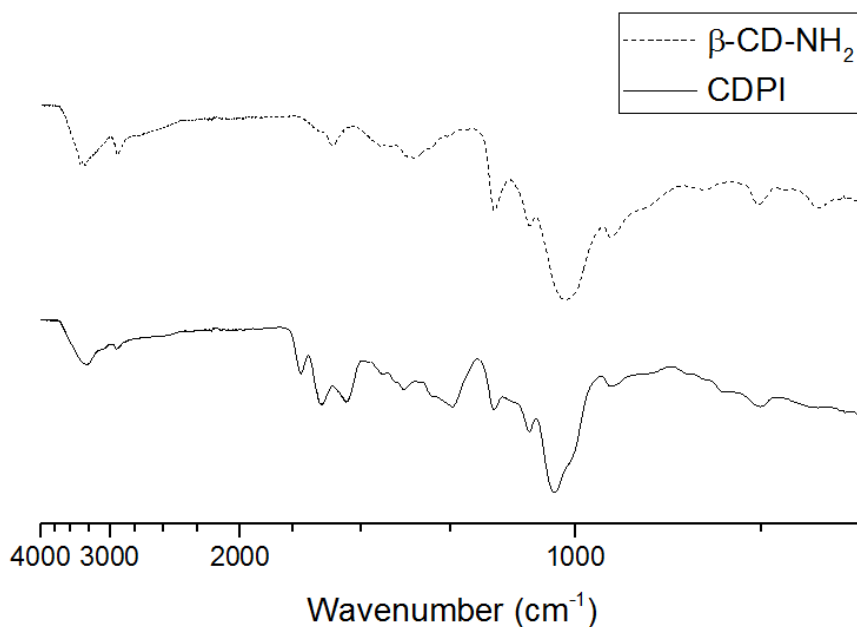
Figure II.4. FTIR transmittance spectra of β-CD-NH$_2$ and CDPI.
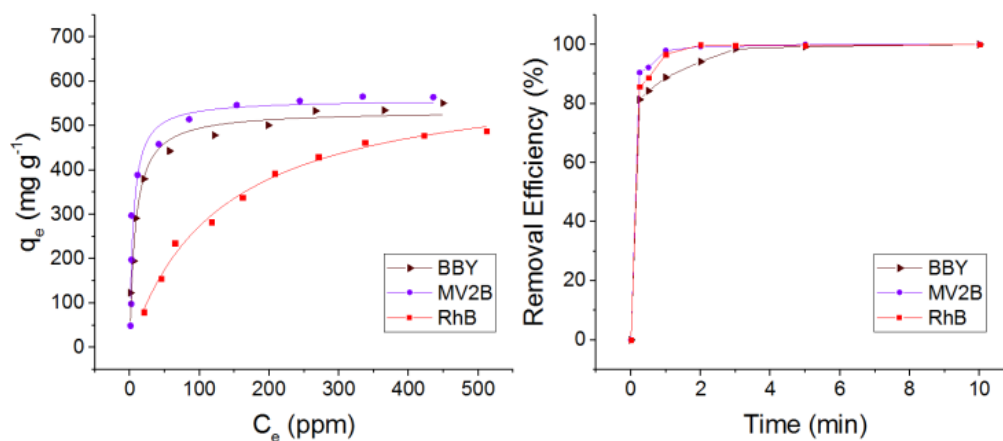
Figure II.5. Adsorption of model compounds at concentrations of 1 mg mL^{-1} in aqueous solutions fit to the Langmuir model (left) and rate of uptake at 1 mg mL^{-1} in 400 ppm aqueous feed solutions (right).
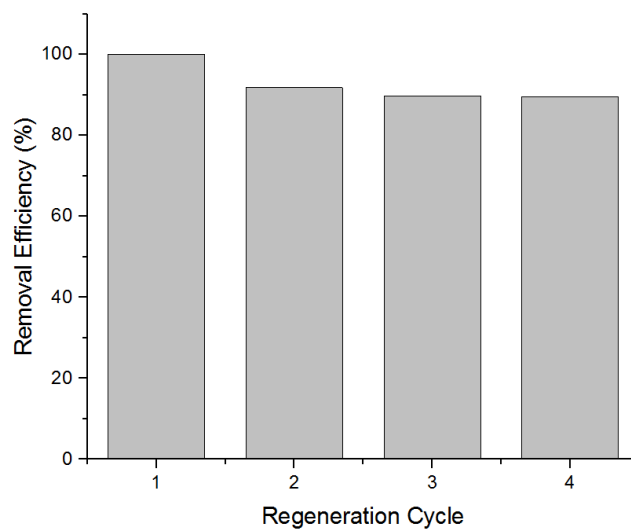
Figure II.6. Efficiency of removal of RhB from 400 ppm aqueous feed solutions by CDPI after repeated regeneration cycles.
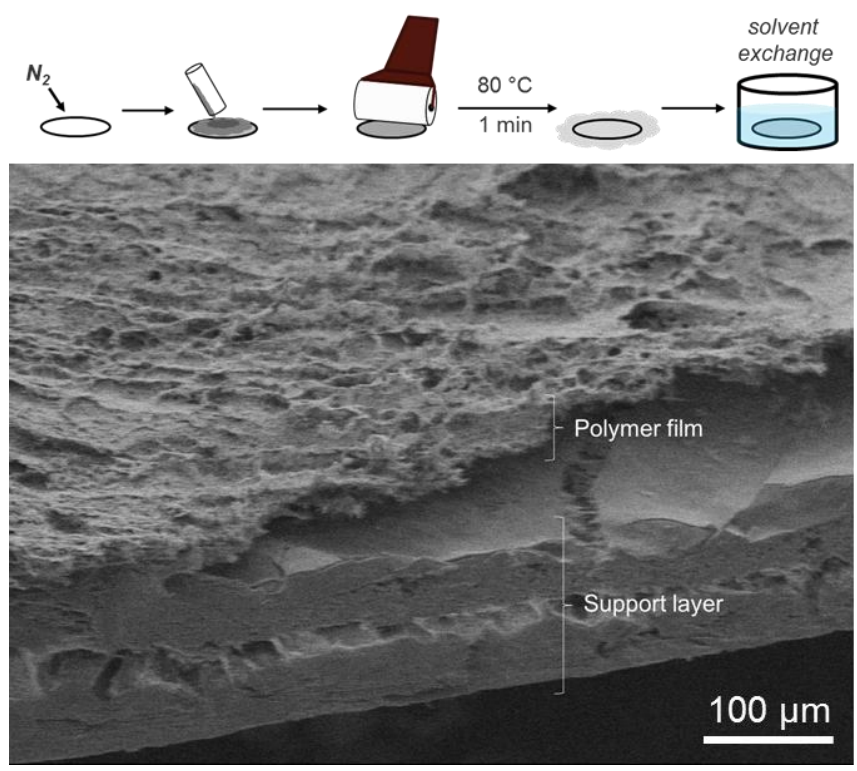
Figure II.7. Schematic overview of CDPI film casting (top) and cross-section SEM image of supported CDPI film (bottom).
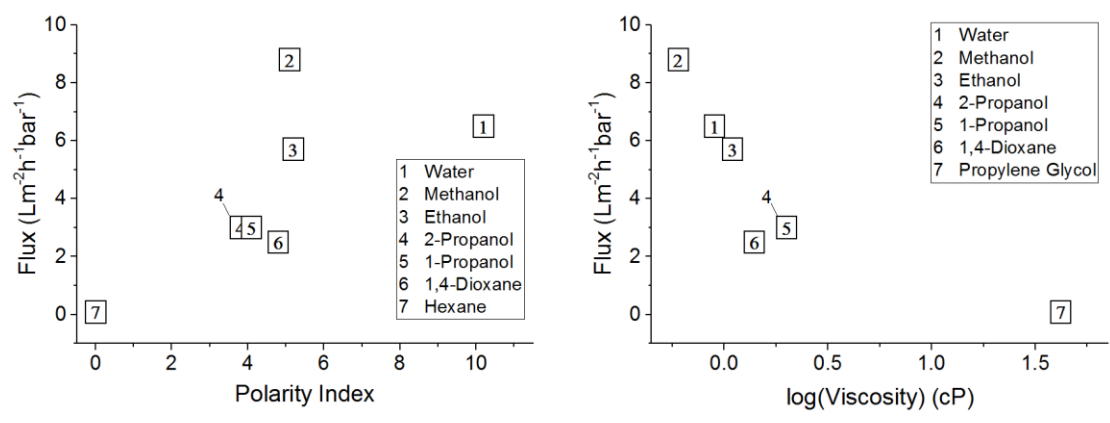
Figure II.8. Relationship of film permeance with solvent polarity (left) and relationship of permeance with viscosity for solvents of similar polarity (right).
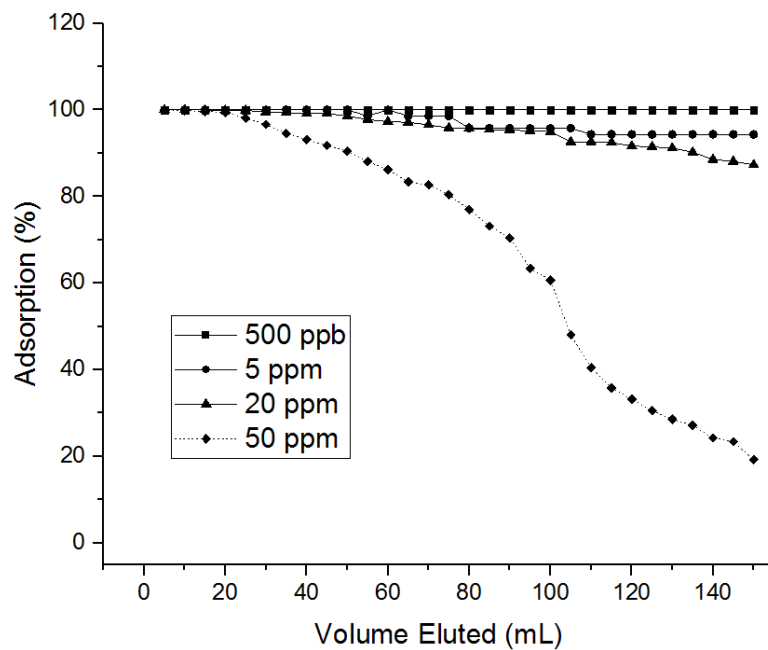
Figure II.9. Adsorption of RhB in aqueous solutions by CDPI films at various feed concentrations.
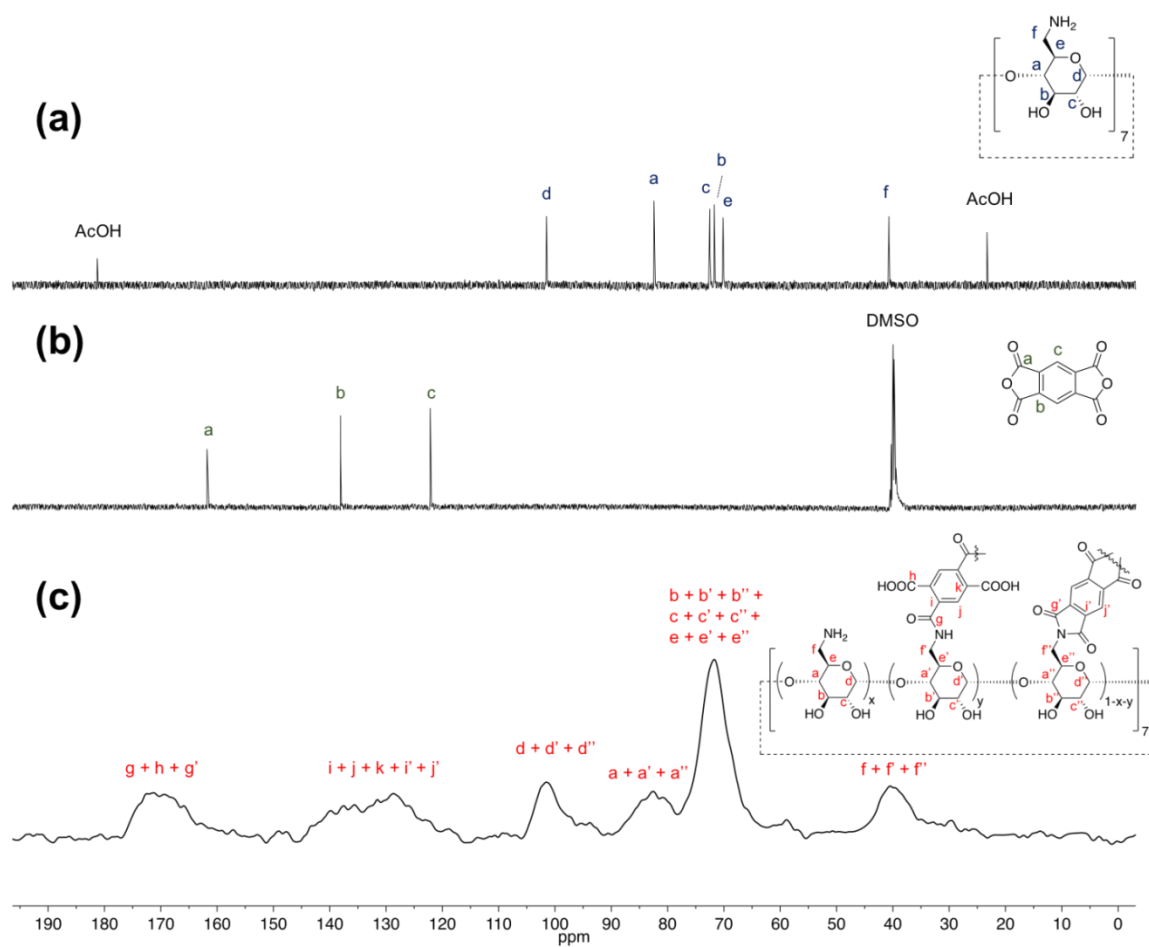
Figure II.10. (a) ^{13}C NMR (126 MHz) spectrum of β-CD-NH$_2$ in D$_2$O; (b) ^{13}C NMR (126 MHz) spectrum of PMDA in DMSO-d_6; and (c) ^{13}C CP-MAS NMR (101 MHz) spectrum of CDPI.
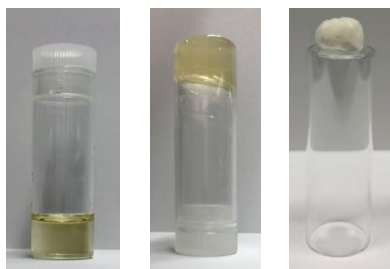
Figure II.11. Images of CDPI as a sol (left), gel (middle), and lyophilized gel (right).

24
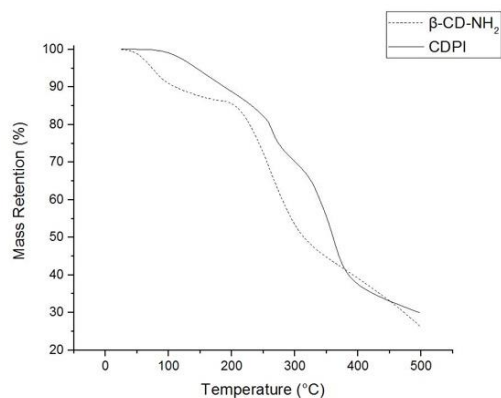
Figure II.12. TGA traces of β-CD-NH$_2$ and CDPI.
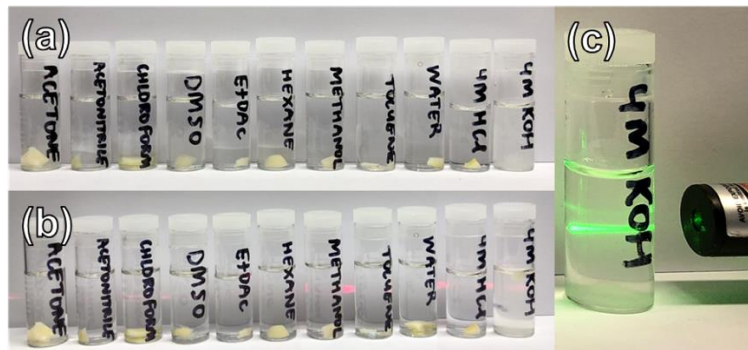
Figure II.13. Determination of solvent resistance of CDPI: (a) image taken after exposure to solvent for 30 d; (b) image taken after illuminating from the left by a red laser to demonstrate solution clarity for all samples, with the exception of the 4 M KOH aqueous solution; (c) a closer look at the Tyndall effect demonstrated for a green laser path through the 4 M KOH aqueous solution, with visible disintegrated material at the bottom of the vial.
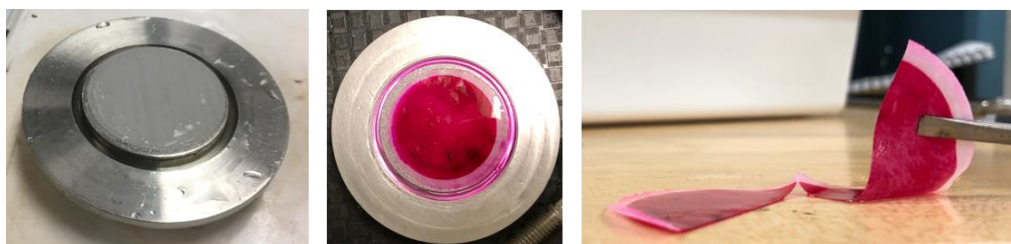
Figure II.14. Images of CDPI supported film before (left) and after (middle, right) RhB adsorption study.

25

Table II.2. Summary of adsorption behavior exhibited by bulk CDPI.
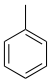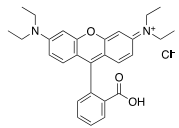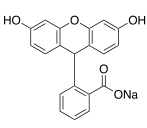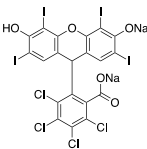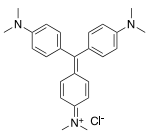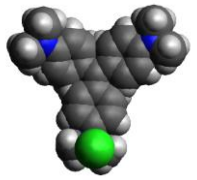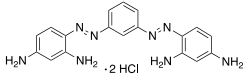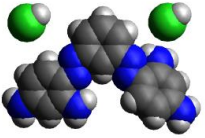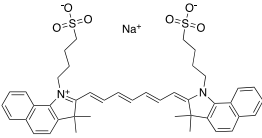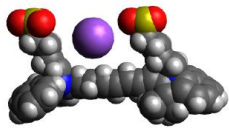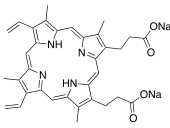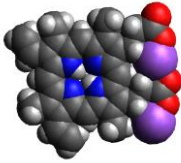
Adsorbate	Structure	3D Model	Charge	Adsorption (C_0)
Toluene			0	46% (340 ppm)
RhB			+1	78% (200 ppm)
FNa			-1	0% (200 ppm)
RB			-2	0% (200 ppm)
MV2B			+1	99% (200 ppm)
BBY			+2	99% (200 ppm)
CG			-1	0% (200 ppm)

Table II.2 Continued

Adsorbate	Structure	3D Model	Charge	Adsorption (C_0)
PPIX			-2	15% (50 ppm)

2.3 Experimental Section

2.3.1 Materials

Pyromellitic dianhydride (PMDA), bromine, sodium azide, Bismarck brown Y (BBY), rhodamine B (RhB), methyl violet 2B (MV2B), protoporphyrin IX (PPIX) disodium salt, cardiogreen (CG), rose bengal (RB), fluorescein sodium (FNa), , triethylamine (Et₃N), acetic anhydride (Ac₂O), glacial acetic acid (AcOH), ammonium hydroxide solution (28 *wt.* % in water), sodium methoxide (25 *wt.* % in methanol), *N*-methylpyrrolidinone (NMP), methanol (MeOH), ethanol, 1-propanol, 2-propanol, propylene glycol, 1,4-dioxane, *n*-hexane, diethyl ether (Et₂O), and anhydrous dimethylformamide (DMF) were obtained from Sigma Aldrich and used as received unless otherwise specified. Triphenyl phosphine (PPh₃) and β-cyclodextrin (β-CD-OH) were obtained from TCI America and used as received unless otherwise specified. Polyvinylidene fluoride (PVDF, 5.0 μm pore size) hydrophilic porous supports were obtained from EMD Millipore. Film release paper (silicone finish, 5 mil thickness) was

purchased from Gardco. Nanopure water (18.2 MΩ cm) was acquired from an EMD Millipore Milli-Q water filtration system.

2.3.2 Characterization

Solution-state ^{1}H and ^{13}C NMR spectra were collected on a Varian Inova 500 spectrometer at room temperature. Solid-state cross-polarization magic angle spinning (CP-MAS) ^{13}C NMR was performed on a Bruker Avance 400 spectrometer with a 4 mm rotor at a spin rate of 8.8 kHz. Instruments were interfaced to a LINUX computer using VNMR-J software. Spectra were processed with MestReNova version 9.0.1-13254 by Mestrelab Research S.L. Attenuated total reflection Fourier-transform infrared spectroscopy (ATR-FTIR) was performed on a Shimadzu IR-Prestige-21 spectrometer at a 1.0 cm^{-1} resolution. Ultraviolet-visible (UV-Vis) absorption spectra were collected on a Shimadzu UV-2550 spectrophotometer from 400–700 nm with polystyrene or quartz cuvettes at a 0.5 nm resolution. Thermogravimetric analysis (TGA) was performed on a Mettler Toledo TGA 2 with a heating rate of 10 °C min^{-1} under argon atmosphere. Nitrogen adsorption-desorption isotherms were measured using a Micromeritics ASAP 2020 system at 77 K. Samples were activated for 8 h at 70 °C under reduced pressure prior to analysis. Pore size distributions were modeled by nonlocal density functional theory (NLDFT) and surface areas were calculated according to the Langmuir model. Scanning electron microscopy (SEM) images of the bulk material were obtained on a Hitachi S-4700 field emission (FE) microscope after gold sputtering of the sample.

28

SEM images of films were collected on a JEOL JSM-7500F FE-SEM equipped with a high brightness conical FE gun and a low aberration conical objective lens after platinum/palladium sputtering of the sample. Elemental analysis was performed at Midwest Microlab, LLC in Indianapolis, IN.

2.3.3 Synthesis and Sorption Studies

Synthesis of per-6-bromo-β-cyclodextrin (β-CD-Br): Preparation of β-CD-Br was performed according to a modified literature procedure.[86] Prior to use, β-CD-OH was dried overnight at 70 °C under reduced pressure. In a flame-dried round-bottom flask equipped with a stir bar, PPh_3 (78.6 g, 0.300 mol) was dissolved in 400 mL anhydrous DMF. The solution was cooled on an ice bath before the slow addition of bromine (47.9 g, 0.599 mol) in 60 mL anhydrous DMF by syringe. The mixture was vigorously stirred until complete dissolution and allowed to warm to room temperature before the addition of β-CD-OH (17.0 g, 15.0 mmol) in one portion. The solution was heated to 73 °C on an oil bath and allowed to stir for 24 h, with careful monitoring to ensure that the temperature did not reach above 75 °C. After cooling to room temperature, the solution was concentrated to *ca.* 200 mL under reduced pressure. Sodium methoxide solution (25 *wt.* % in methanol) was then slowly added until a pH of 9 was obtained. The product was collected by precipitation into a large excess of cold methanol, followed by thoroughly rinsing with methanol. The product was dried at 70 °C under reduced pressure for 24 h, yielding a fluffy, colorless powder (22.4 g, 94.8%

yield). Characterization data was consistent with published data;[86] ^{1}H NMR data are provided for example. ^{1}H NMR (500 MHz, DMSO-d_6, ppm) δ 6.03 (d, J = 6.5 Hz, 7H), 5.90 (d, J = 2.0 Hz, 7H), 4.98 (d, J = 3.5 Hz, 7H), 4.00 (d, J = 9.5 Hz, 7H), 3.82 (t, J = 9.5 Hz, 7H), 3.70–3.60 (m, 14H), 3.40–3.32 (m, 14H).

Synthesis of per-6-azido-β-cyclodextrin (β-CD-N$_3$): Preparation of β-CD-N$_3$ was performed according to a modified literature procedure.[86] In a flame-dried round-bottom flask equipped with a stir bar, β-CD-Br (21.0 g, 13.3 mmol) was dissolved in 400 mL anhydrous DMF, forming a colorless solution. Sodium azide (12.1 g, 186 mmol) was added in one portion, resulting in the rapid evolution of a yellow color. The suspension was stirred at 40 °C on an oil bath for 24 h, before allowing to cool to room temperature. The mixture was carefully concentrated to *ca*. 200 mL of solution under reduced pressure before pouring into a large excess of water. The solids were collected, thoroughly rinsed with water, and dried at 70 °C under reduced pressure for 24 h, yielding a colorless powder (16.6 g, 95.1% yield). Characterization data was consistent with published data;[86] ^{1}H NMR data are provided for example. ^{1}H NMR (500 MHz, DMSO–d_6, ppm) δ 5.91 (d, J = 6.5 Hz, 7H), 5.77 (s, 7H), 4.91 (d, J = 3.5 Hz, 7H), 3.83–3.69 (m, 14H), 3.64–3.54 (m, 14H), 3.41–3.30 (m, 14H).

Synthesis of per-6-amino-β-cyclodextrin (β-CD-NH$_2$): Preparation of β-CD-NH$_2$ was performed according to a modified literature procedure.[86] In a flame-dried round-bottom flask equipped with a stir bar, β-CD-N$_3$ (15.0 g, 11.4 mmol) was dissolved in 250 mL anhydrous DMF. After dissolution, PPh$_3$ (42.2 g, 161 mmol) was added slowly, with sufficient venting. The solution was allowed to stir at room temperature for 2 h,

before the slow addition of 72 mL ammonium hydroxide (28 *wt.* % in water). The

solution was allowed to stir for 16 h, with the slow formation of a colorless precipitate.

The mixture was then diluted with 250 mL methanol, and the solids were collected and

further rinsed with methanol. The product was then rinsed thoroughly with Et_2O and

dried under reduced pressure at 70 °C, yielding a fine, colorless powder (11.8 g, 91.0%

yield). To prepare a sample for analysis by solution-state NMR spectroscopy, *ca.* 40 mg

of solids were suspended in 2.0 mL deuterated water before the addition of one drop

AcOH. The mixture was stirred until dissolution. Characterization data was consistent

with published results.[86] ^{1}H NMR (500 MHz, D_2O, ppm) δ 5.13 (d, J = 3.5 Hz, 7H),

3.99–3.88 (m, 14H), 3.68 (dd, J = 3.5 Hz, J = 10 Hz, 7H), 3.58–3.49 (m, 7H), 3.23 (dd, J

= 3.5 Hz, J = 13.5 Hz, 7H), 3.10–3.02 (m, 7H). ^{13}C NMR (126 MHz, D_2O, ppm) δ

101.51, 82.41, 72.50. 71.72, 70.15, 40.69. FTIR (cm^{-1}): 3631–3016, 2974–2834, 1657,

1598, 1439, 1414, 1366, 1338, 1298, 1254, 1218, 1152, 1082, 1017, 944, 888, 816, 754,

723, 691. TGA: 50–120 ℃, 11% mass loss; 205–315 ℃, 40% mass loss; 315–500 °C,

23% mass loss; 26% mass remaining above 500 ℃.

Preparation of CDPI in cylindrical molds: To a shell vial was added β-CD-NH_2

(0.500 g, 0.443 mmol), followed by 1.75 glacial acetic acid and 3.88 mL NMP. The

mixture was sonicated until complete dissolution before the addition of PMDA (266 mg,

1.22 mmol) in one portion. The mixture was quickly vortexed until dissolution, upon

which gelation rapidly occurred. The gel was then heated to 70 °C on a hot plate for 10

min, before carefully breaking the vial to remove the gel. The solid gel was then soaked

in a solution of 2.5 mL Ac_2O, 3.7 mL Et_3N and 5 mL DMF for 1.5 h. The liquids were

then removed by pipette and discarded, and the gel was soaked in 100 mL fresh DMF for 1 h to allow for solvent exchange. This was repeated two additional times with DMF, followed by exchange into methanol by the same process, repeated five times. In preparation of samples for scanning electron microscopy, the gel was dried by supercritical carbon dioxide extraction to better preserve its macroporous structure, and was then cut with a razor blade to image the interior of the sample. For all other studies, the gel was exchanged into water five times and dried by lyophilization. To determine chemical resistance, samples were cut with a razor blade and submerged in the chosen solution and allowed to stand for 30 d. For analysis by NMR, samples were milled in a conical burr grinder. For all other studies, samples were cut to size with a razor blade. ^{13}C CP-MAS NMR (101 MHz, spin rate 8.8 kHz, ppm) δ 177.68–162.92, 146.19–120.65, 106.16–91.51, 90.53–62.43, 50.62–35.08. FTIR (cm^{-1}): 3672–2996, 2996–2840, 2486, 1781, 1717, 1637, 1550, 1487, 1436, 1397, 1370, 1295, 1245, 1153, 1083, 1036, 946, 885, 840, 817, 794, 752, 696. TGA: 80–250 ℃, 19% mass loss; 255–280 ℃, 6% mass loss; 285–330 ℃, 7% mass loss; 330–390 ℃, 30% mass loss; 390–500 ℃, 10% mass loss; 28% mass remaining above 500 ℃. Anal. calcd. for $(C_6H_{12}NO_4)_{1.5} \cdot (C_6H_{10}NO_4)_{5.5} \cdot (C_{10}H_2O_4)_{2.75} \cdot (H_2O)_{12}$: C, 45.37; H, 4.96; N, 5.33. Found: C, 45.24; H, 5.13; N, 5.26. $S_{Langmuir}$ (N$_2$ adsorption, 77 K) 155 m^2 g^{-1}.

Preparation of CDPI films: Prior to use, PVDF microfiltration supports were cleaned under flow of nitrogen. In a small vial, β-CD-NH$_2$ (0.100 g, 0.0886 mmol) was dissolved in 0.35 mL glacial acetic acid and 0.77 mL NMP. The mixture was sonicated until total dissolution, upon which PMDA (53 mg, 0.24 mmol) was added in one portion.

The mixture was vortexed until homogeneous and quickly applied to the porous support between two sheets of film release paper before phase separation and hardening of the gel. The film was pressed with a rubber roller and then baked on a hot plate at 70 °C for 1 min. After cooling to room temperature, excess film around the edges of the porous support was removed with a razor blade, and the membranes were submerged in a solution of 2.5 mL Ac_2O and 3.7 mL Et_3N in 10 mL DMF for 1 h. Membranes were then exchanged into 100 mL fresh DMF, followed by exchange into fresh methanol three times, and storage in methanol. For SEM imaging, films were then exchanged into water, freeze-fractured, and dried by lyophilization. By this method, films of 20 ± 2 μm thickness were produced on the 120 ± 10 μm support layer (manufacturer specification: 125 μm), measured by SEM.

Preparation of standard solutions: Toluene standard solutions were prepared by the addition of 1 drop of toluene to a known mass of water. The theoretical concentration was calculated by mass and confirmed by UV absorbance at 268 nm. A PPIX standard solution was prepared by the addition of 50.0 mg of the disodium salt to 1.000 kg water to obtain a concentration of 50.0 ppm. For all other solutions, 1.000 g of the desired compound was added to a glass bottle, followed by 1.000 kg water to obtain a 1000 ppm stock solution. The solution was allowed to stand for 4 h before diluting with water by mass to the desired concentration.

Dye adsorption isotherm studies: To a small vial containing 10.0 mg CDPI was added 10.0 mL of the chosen dye solution by calibrated pipette. After standing 1 h in the dark, the liquid was removed by pipette and analyzed by UV-Vis spectroscopy.

33

Adsorbate concentration was quantified by the absorbance intensity at the selected wavelength (Table II.3). Maximum adsorption capacity, Q_0 (mg g^{-1}), was calculated according to the Langmuir model for compounds BBY, MV2B, and RhB. Conversion to the molar adsorption capacity when accounting for molar mass of the dye (BBY: 393.96 Da; MV2B: 419.31 Da; and RhB: 479.02 Da) could then be used to determine the number of dye molecules adsorbed per cyclodextrin unit at equilibrium with a theoretical CDPI cyclodextrin content of 0.609 mmol g^{-1}. Experiments were repeated in triplicate to confirm reproducibility.

Table II.3. Selected wavelengths for concentration quantification.

Adsorbate	Wavelength (nm)
Toluene	268
RhB	440, 554[†]
FNa	530
RB	512
MV2B	420
BBY	468[†], 556.5
CG	419
PPIX	591

[†]For dilute (<50 ppm) concentrations

Rate of uptake studies: To a small vial containing 10.0 mg CDPI was added 10.0 mL of the chosen dye solution (400 ppm feed concentration) by calibrated pipette. The liquid was removed by pipette at the corresponding time points and analyzed by UV-Vis

spectroscopy, with 15 s being the shortest time in which the liquid could be withdrawn by pipette. Absorbance values according to Table II.3 were used to quantify the dye concentration, and experiments were repeated in triplicate to ensure reproducibility.

Sorbent regeneration studies: To a vial containing 50.0 mg CDPI was added 50.0 mL of 400 ppm RhB solution by pipette. After standing 1 h in the dark, the liquid was removed by pipette and analyzed by UV-Vis spectroscopy, with absorbance at 440 nm used to quantify dye concentration. The material was then soaked for 4 h three times in 50 mL MeOH, followed by soaking for 1 h twice in 50 mL water and dried by lyophilization. Four regeneration cycles were performed, each analyzed analogously at 1 mg mL^{-1}, and experiments were performed in triplicate to ensure reproducibility.

Membrane separation studies: Membranes were analyzed in a dead-end configuration on a Sterlitech stainless steel stirred cell (effective membrane area 14.6 cm^2) with a nitrogen feed pressure of 3.4 bar. Membranes were soaked in an excess of the desired solvent of study for an hour prior to use to ensure solvent exchange. To quantify membrane flux, the mass of filtrate was measured in 5 min intervals for 30 min for each solvent studied. For dye adsorption experiments of films, filtrate was collected in 5.0 mL aliquots for 150.0 mL and analyzed by UV-Vis spectroscopy to determine dye concentration. RhB, concentration was quantified by absorbance at 554 nm. These studies were also performed on uncoated supports that were soaked in the curing solution for 1 h and rinsed with methanol to emulate preparation conditions for the coated membranes. For these uncoated supports, it was found that permeances for all solvents tested were too large to accurately measure on the testing apparatus, and no

RhB adsorption was observed. Experiments were repeated in triplicate to confirm reproducibility.

Vapor adsorption studies: 15.0 mg of CDPI was added to a 2-dram shell vial and tared on a microbalance. The vial was then placed without capping next to an open vial of *ca.* 15 mL toluene on a hot plate under a glass dish (Figure II.15). A small rubber septum was used to elevate the sample from the heating surface. After 4 h at 70 °C, the vial was removed and allowed to stand at room temperature for 5 min. Toluene adsorption was quantified by the increase in mass, and this experiment was repeated five times to ensure reproducibility.
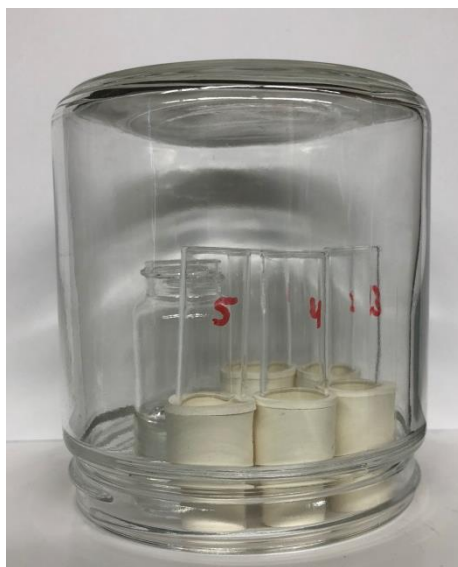
Figure II.15. Experimental setup for toluene vapor adsorption studies.

CHAPTER III

ABSORBABLE HEMOSTATIC HYDROGELS COMPRISING COMPOSITES OF

SACRIFICIAL TEMPLATES AND HONEYCOMB-LIKE NANOFIBROUS MATS

OF CHITOSAN[*]

3.1   Introduction

Hemorrhage is a leading cause of death in traumatic injuries,[101] the fourth-leading cause of death in the United States with a total cost of 671 billion USD in 2013.[102] Mitigating blood loss is, therefore, a vital initiative, serving as the impetus for the development of diverse hemostatic technologies and biomaterials for emergency scenarios, not only in both civilian and military traumatic settings, but also during variable therapeutic interventions.[103]   Hemostatic agents derived from chitosan, a naturally-derived polysaccharide produced from the deacetylation of chitin, have been widely studied for their fast-acting and localized hemostatic effects.[104] Chitosan is also well known for its antimicrobial properties, and its protection against a wide range of bacteria enhances its appeal as a bandage, where it has found use as the active component in a number of commercial wound dressings, including HemCon[®], Chitodine[®], TraumaDEX[®], Celox™, and others.[104-106] The efficacy of chitosan-based

hemostatic agents has been established in significantly improving survival rates and the reduction of blood loss, by accelerating and strengthening blood clots.[107-108] As these technologies rely on a high surface area to promote interaction with platelets and coagulation factors, maximizing the surface area of these chitosan-based materials is a critical initiative for improving their effectiveness.[109] Reported methods to increase the surface area of chitosan-based biomaterials include micellization[110] and incorporation into porous templates.[111-112] The incorporation of chitosan into a template, serving as a delivery vessel, is an especially attractive option, as it simplifies administration. However, products that rely on the loading of chitosan into non-degradable carriers (*e.g.* gauze) necessitate further procedures to remove the bandage and may lead to potential complications,[113] thus rationalizing the development of physiologically-benign, absorbable chitosan delivery agents.

Absorbable hemostatic dressings, such as Surgicel®, Curaspon®, and others, are generally composed of gelatin, oxidized regenerated cellulose, collagen, *etc.*[114-116] Although, in principle, chitosan is a degradable material, chitosan hemostatic powder is not considered bioabsorbable, as it forms large aggregates, generally requires acidic conditions for dissolution, and, therefore, must be removed from the wound before surgical repair.[117] Nanoscale assembly of chitosan may aid in enhancement of the hemostatic efficiency and prevention of aggregate formation in physiological milieu; although, such assembly by the loading of chitosan into bioabsorbable templates is challenging. Macroporous templates have been employed in the assembly of chitosan materials with high surface area for wound healing[118] and other applications,[119-120]

however, no nanoscale features were observed in these examples, even when nanostructured templates were employed, such as oxidized nanofibrillar cellulose.[121] As the self-assembly of chitosan has been demonstrated to be heavily dependent upon ionic interactions,[122] it was hypothesized that a porous framework capable of such interactions may enable the nanoscale assembly of chitosan within the interstices of a framework.

In this work, hydrolytically-degradable, macroporous saccharide hydrogels were targeted as the sacrificial template. It was hypothesized that these organic frameworks containing sites for ionic interactions would enable the loading and subsequent assembly of chitosan within the microstructured matrix, resulting in an easily-administered chitosan bandage with high surface area, and enhanced hemostatic efficiency. A macrocyclic oligosaccharide, β-cyclodextrin, was selected as the primary building block of the hydrogel, as its facile incorporation into porous materials has been established in the literature,[25, 93, 123] and the hypothesized chemical compatibility between the saccharide-derived host and guest was expected to facilitate chitosan loading into the matrix. We have recently demonstrated the preparation of porous, chemically-resistant polyimide gels from an aminated β-cyclodextrin derivative, cross-linked with a dianhydride linker.[123] It was envisioned, in this work, that native hydroxylic β-cyclodextrin could be analogously cross-linked with a dianhydride to yield a polyester-linked porous gel, capable of hydrolytic degradation under physiological conditions. To this end, a hyperbranched cyclodextrin polyester (CDPE) crosslinked hydrogel was designed, utilizing the polyol functionality of β-cyclodextrin to form a polyester framework. The degradation of the prepared hydrogels was studied by proton nuclear

magnetic resonance (^{1}H NMR) spectroscopy, and the assembly of chitosan within the matrix was evaluated by scanning electron microscopy (SEM), following chitosan loading into the hydrogels and template removal. The hemostatic efficiency and biocompatibility of the composite chitosan-loaded CDPE (CDPE-Cs) hydrogels were then examined *in vivo*, in several animal models.

3.2   Results and Discussion

CDPE networks were readily formed by the reaction between β-cyclodextrin and a dianhydride linker (3 equiv.) in dimethylsulfoxide (DMSO), when catalyzed by an organic base (triethylamine, 3 equiv.) (Figure III.1). Reagents were combined in a flask before transfer into shallow, cylindrical molds. Following a short heating period at 70 °C, to induce gelation, the resulting transparent gel was removed and cut to desired shapes with a razor blade. Several dianhydrides were screened, and 3,3',4,4'-biphenyl-tetracarboxylic dianhydride (BPDA) was found to offer the greatest compatibility with the mold-casting process. Dianhydrides, such as pyromellitic dianhydride (PMDA), with greater solubility in the solvent system used induced a rapid increase in viscosity, causing difficulty during transfer to the molds. Gels were formulated at 16 *wt.*%, calculated by the mass of solids as a fraction of the total system mass. Gels with lower weight fractions were expected to yield greater porosities and, therefore, larger chitosan loading capacities, though at the cost of increasing fragility. However, at weight fractions below 14 *wt.*%, gelation did not occur. Therefore, 16 *wt.*% was chosen to

provide gels that could be easily formed and handled, while facilitating the desired chitosan loading behavior.
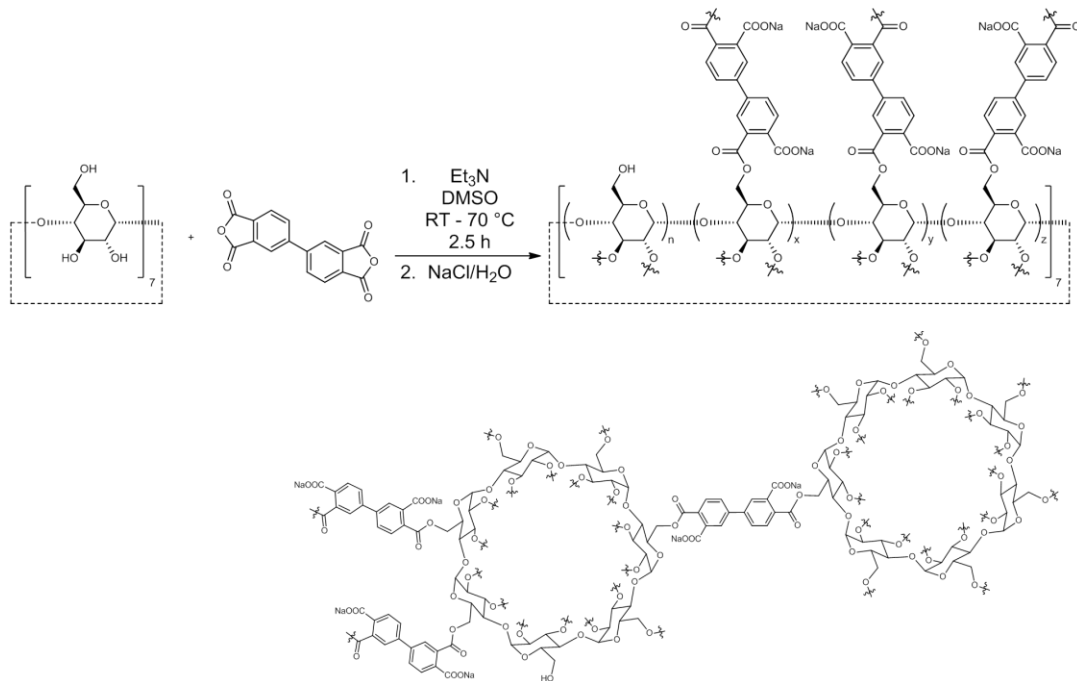
Figure III.1. Overview of the synthesis of CDPE (top) with an expanded illustration of the diversity of potential linkages and structural components (bottom).

The gels were thoroughly washed with DMSO to remove soluble, insufficiently-crosslinked components and remaining reagents, followed by exchange into aqueous sodium chloride solution to convert ammonium carboxylate groups to their respective sodium salts. The gels were then exchanged into and stored in water. The resulting hydrogels could then be further used in their hydrated form, or dried by lyophilization for characterization. CDPE displayed stability when stored in hydrated form over a period of 2 weeks, however, full dissolution was observed in a concentrated potassium hydroxide (KOH) aqueous solution within *ca.* 1 min, confirming the base-sensitivity of

the ester linkages, as designed. When lyophilized and placed in an excess of phosphate-buffered saline (PBS) at 37 °C, the gel degraded into water-soluble byproducts over the course of 7 d, as monitored by ^{1}H NMR spectroscopy (Figure III.2a, III.5b). Turbidity measurements of the resulting solution confirmed solution clarity by full transmittance at 450 nm, and dynamic light scattering (DLS) measurements indicated the degradation of CDPE into a narrow distribution of small particles, with diameters centered around ca 2.7 nm (Figure III.2b).
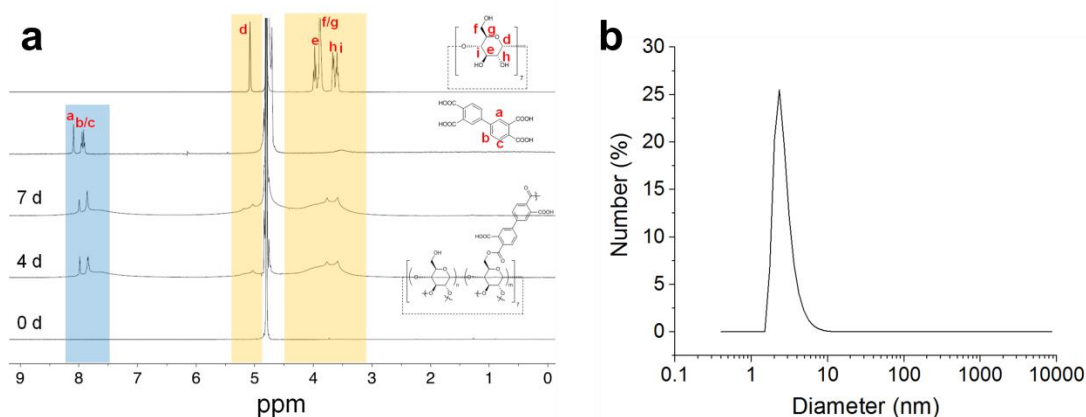
Figure III.2. Overview of the degradation of CDPE in PBS. (a) ^{1}H NMR (500 MHz, in PBS D$_2$O solution) spectra of the CDPE template at selected time points, showing degradation over 7 d. (b) Particle size distribution of CDPE template solution in PBS after 7 d, measured by DLS.

When viewed by SEM, CDPE exhibited a porous, complex morphology (Figure III.4b). To examine the ability of these CDPE templates to load and assemble chitosan, samples were submerged in a 1 *wt.*% solution of chitosan (Figure III.3a), prepared in 1% aqueous acetic acid with 5 M aqueous sodium hydroxide added dropwise until a pH of

5.5 was reached. Over the course of 7 d, chitosan was allowed to migrate into the gel, and the samples gradually became slightly less transparent (Figure III.3b). CDPE templates displayed stability in the chitosan solution, remaining intact for the duration of the loading process, and control studies indicated only minor degradation of the template in 1% acetic acid over 7 d, as observed by ^{1}H NMR spectroscopy (Figure III.5).

To probe the morphology of the loaded chitosan, the composite CDPE-Cs gel was lyophilized and rinsed with 5 M aqueous sodium hydroxide solution to remove the sacrificial CDPE template, yielding a monolithic mat of chitosan (Figure III.3c). The mass loss during template removal was *ca.* 81%, suggesting that the templated chitosan mat represented *ca.* 19% of the total dry mass of the CDPE-Cs composite gel. The resulting templated chitosan monoliths were sufficiently durable to enable handling without fracturing, and were stable in water. However, the material could be fully dissolved in trifluoroacetic acid, with sonication. The physical structure of the templated chitosan mat was probed by SEM, revealing a porous, sponge-like material of highly-entangled fibers (Figure III.4d,e, f), with diameters of 9.2 ± 3.7 nm (Figure III.4g).
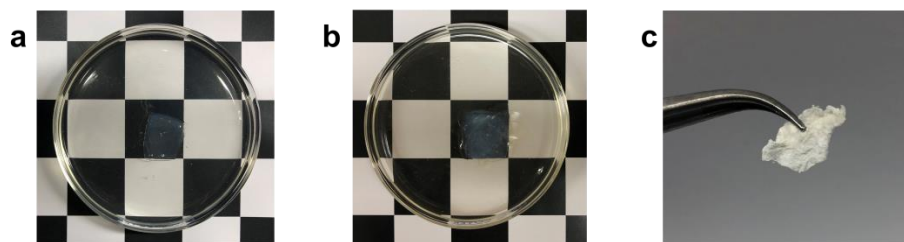
Figure III.3. Overview of the preparation of CDPE-Cs hydrogels and templated chitosan mats. (a) CDPE hydrogels upon initial immersion in 1 *wt.* % chitosan solution. (b) CDPE hydrogels after 7 d to allow chitosan loading. (c) Chitosan mats after lyophilization and template removal by rinsing with alkaline solution.
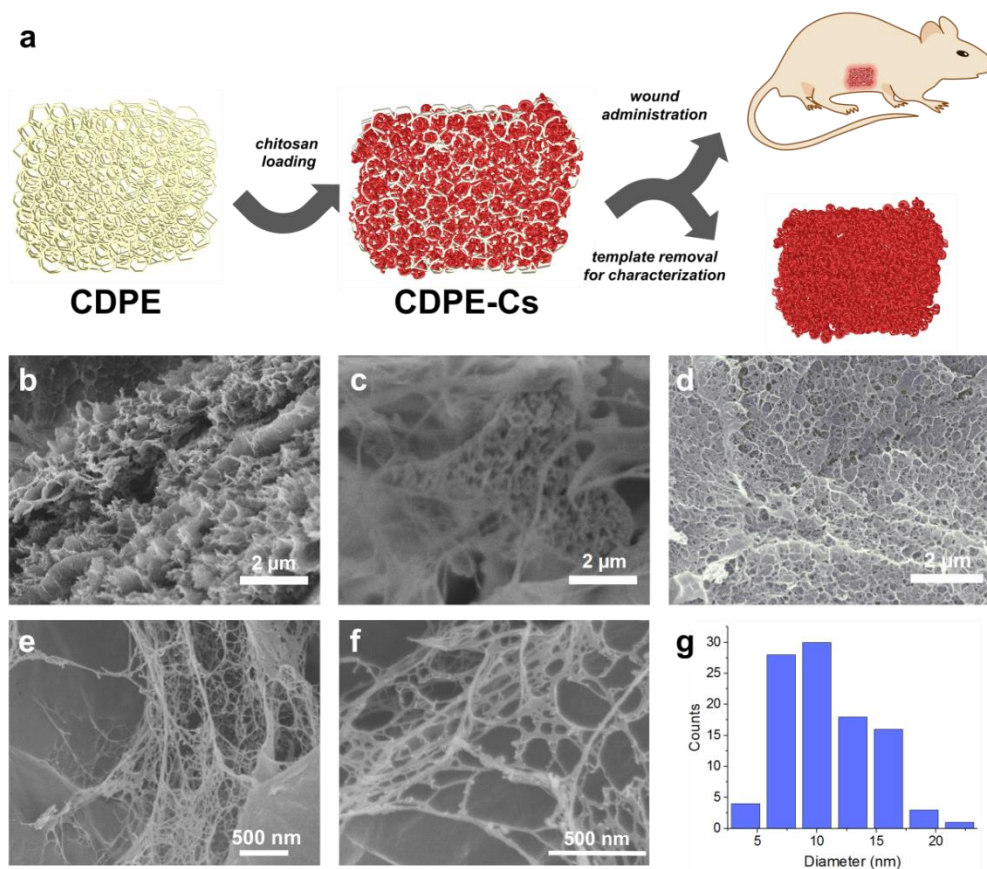
Figure III.4. CDPE template, CDPE-Cs composite gel, and templated chitosan material exhibit amorphous, macroporous morphology. (a) Simplified illustration of the chitosan templating process, administration of CDPE-Cs to wound site, and template removal for imaging. (b) SEM image of CDPE after drying by lyophilization, showing complex, porous surface morphology. (c) SEM image of chitosan-loaded composite CDPE-Cs gel after lyophilization. (d) SEM image of templated chitosan material, displaying a honeycomb-like structure. (e–f) Magnified SEM images of nanofibrillar domains in the templated chitosan, with a web-like morphology within the network cavities. (g) Histogram plot showing the distribution of fiber diameters observed by SEM.

The CDPE template, loaded CDPE-Cs hydrogel, and templated chitosan after template removal were characterized individually by both solution- and solid-state techniques to probe their chemical compositions. Absorption at 1710 and 1603 cm^{-1} in the infrared (IR) absorption spectrum of the CDPE template confirmed the presence of

44
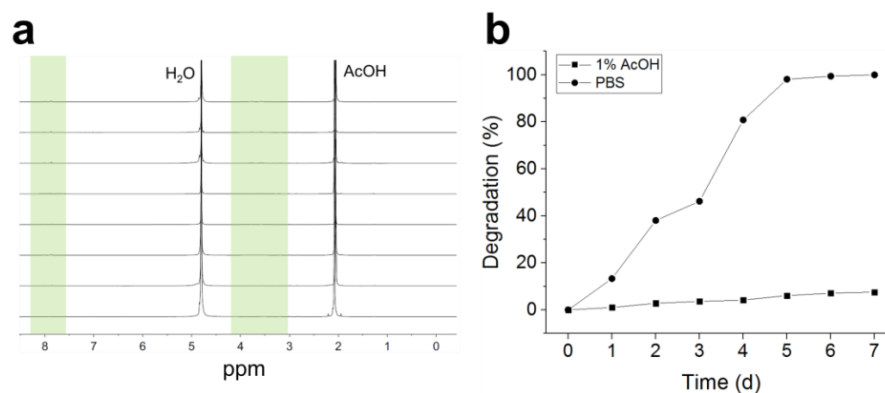
Figure III.5. Overview of CDPE stability in 1% aqueous AcOH. (a) ^{1}H NMR (500 MHz) spectra of CDPE template, in 1% acetic acid solution in D_2O, over 7 d. (b) Degradation of CDPE template in PBS and 1% acetic acid aqueous solution, as measured by the cumulative signal increase observed by ^{1}H NMR spectroscopy. For the sample in 1% AcOH, the degree of degradation was calculated using the acetic acid peak as an internal reference. For the sample in PBS, the degree of degradation was normalized to the signal integration at 7 d.

ester linkages and carboxylate groups, respectively (Figure III.6a). The characteristic backbone vibration of β-cyclodextrin at 1032 cm^{-1} was also observed, indicating that the integrity of the macrocyclic backbone of cyclodextrin was maintained. Upon chitosan loading, the appearance of absorption bands at 2853, 1653, and 894 cm^{-1}, corresponding to chitosan, was observed. Upon template removal, it was revealed that the absorption intensity at 1571 cm^{-1}, corresponding to the N–H stretch of the primary amines, was amplified when compared with native chitosan, suggesting further deacetylation of the amine groups. When examined by ^{1}H NMR spectroscopy, the degree of deacetylation, calculated by the integration of the corresponding signals, was found to be 67%, compared with the 62% measured for the native chitosan used (Figure III.6f), confirming further deacetylation of the templated chitosan. Powder X-ray diffraction (PXRD) data indicated the amorphous character of CDPE, and the complete disappearance of peaks

45

seen in the β-cyclodextrin starting material suggest the lack of remaining crystalline β-cyclodextrin entombed in the matrix (Figure III.6d). The templated chitosan material was also found to be amorphous by PXRD (Figure III.6c).
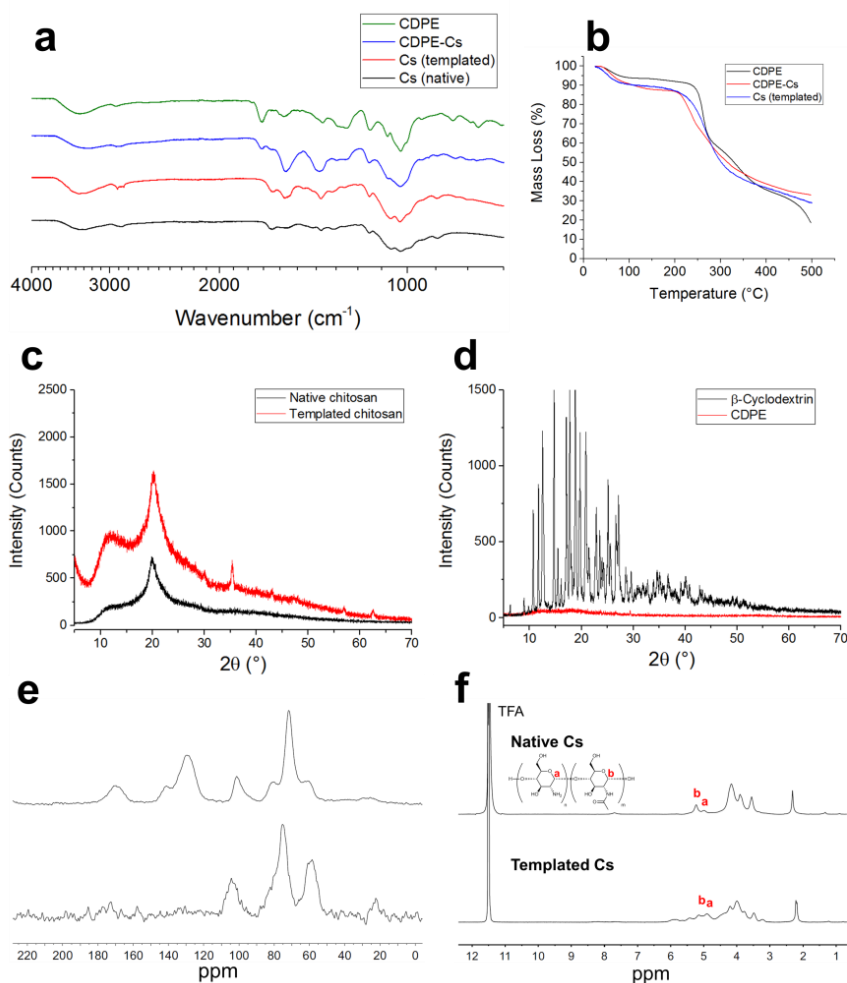
Figure III.6. Characterization data for CDPE, CDPE-Cs, and templated chitosan mats. (a) ATR-FTIR spectra of materials at each stage of the templating process. (b) TGA curves at each stage of the templating process. (c) PXRD spectra of native and templated chitosan. (d) PXRD spectra of CDPE and β-cyclodextrin. (e) ^{13}C CP-MAS NMR (101 MHz) spectrum of CDPE (top) and templated chitosan (bottom). (f) ^{1}H NMR spectra of native chitosan (top) and templated chitosan (bottom).

46

The hemostatic efficiency of the chitosan-loaded hydrogels was then evaluated *in vivo*, in acute liver punch models of rats, rabbits and pigs. Liver punches of 1 cm in diameters and 0.3 cm in depths were excised in the animals using a circular blade fixed onto a syringe, to ensure the consistency of the induced bleeding across various animals. The circular blade-fixed syringe was used to cut the hemostatic hydrogels and the controls into the same dimensions (*i.e.* 1 cm × 0.3 cm) of the injury sites. The control wound dressings included conventional gauze, blank CDPE hydrogels, Surgicel® and Curaspon®. Surgicel® and Curaspon® are commercially available absorbable hemostatic agents mainly composed of oxidized regenerated cellulose and gelatin, respectively. After injury and excision of the standardized liver tissue, initial bleeding was absorbed into a conventional wound dressing. Then, various dressings were implanted into the injury sites and checked every 30 s for bleeding. The weights of the dressings were recorded before applications of the dressings and at the end of the experiments to measure the amounts of blood loss. A heparinized rabbit model was utilized at a certain dose of heparin (*i.e.* 250 IU/kg) to achieve bleeding that would not stop spontaneously after the liver injury. Mean arterial blood pressure (MAP) was recorded, only in rabbits, *via* insertion of a 20-gauge catheter into the right carotid artery and continuous recording of MAP under general anesthesia before the liver injury and for 1 h after the injury. Blood pressure was monitored on a polygraph using a Universal Oscillograph instrument. The animals were alive for the duration of the experiment.

After application of conventional gauze to the injury sites, bleeding did not stop until the end of the experiments (10 min) in rats, rabbits, and pigs (Figure III.7a, c, e).

47

The amounts of blood loss were also the most significant from injured livers treated with the conventional gauze dressings in rats, rabbits and pigs (Figure III.7b, d, f). Furthermore, the heparinized rabbits treated with conventional gauze failed to maintain a normal MAP (Figure III.7g). All the other groups maintained a normal MAP through the duration of the experiments, with slight decreases in the MAP observed for the Surgicel® and blank CDPE hydrogel groups after the liver injury. Generally, the absorbable dressings resulted in significantly faster hemostasis and lower amounts of blood loss compared to the conventional gauze dressings, although the experimental factors were fixed, except for the type of the dressing. In rats, significantly faster hemostasis was observed in the group treated with the CDPE-Cs hydrogel as compared to Surgicel®, Curaspon®, and the blank CDPE hydrogel ($p < 0.001$). Similarly, significantly lower amounts of blood loss were also found in the group treated with the CDPE-Cs hydrogel as compared to Surgicel® ($p < 0.01$) and Curaspon® ($p < 0.05$). A similar pattern was also observed in rabbits, where the CDPE-Cs hydrogel resulted in shorter time to hemostasis ($p < 0.001$), as compared to Surgicel®, Curaspon®, and the blank CDPE hydrogel, and a lower amount of blood loss than the amounts from rabbits treated with Surgicel® ($p < 0.001$) and Curaspon® ($p < 0.05$). However, it was observed that there were increases in the time to hemostasis and amounts of blood loss as compared to the rat and pig models, which might be due to the anticoagulant effect of the heparin utilized in the rabbit models. In pigs, there were significantly faster times to hemostasis ($p < 0.01$ and $p < 0.001$) and lower amounts of blood loss ($p < 0.05$) in the CDPE-Cs hydrogel group, as compared to the Surgicel® and the blank CDPE hydrogel

groups, respectively. However, the differences in time to hemostasis and amounts of blood loss were not significant, when compared to Curaspon®, but in favor of the CDPE-Cs hydrogel treated group.

Preliminary evaluations of the biocompatibility and degradability of the dressings were performed *via* implantation of the dressings into the injured livers of rats. Photomicrographs of the livers from rats following implantation of the different hemostatic dressings for 7 d and control untreated rats are illustrated in Figure III.8. The active bleeding can be clearly seen in the animals immediately after the injury and after the application of the conventional gauze, whereas hemostasis is achieved after treatment with Curaspon®, Surgicel®, and CDPE-Cs hydrogels. After one week of implantation, visual and histological examinations of the tissues surrounding the livers were performed (Figure III.9). Complete healing was observed in the groups treated with Curaspon® and CDPE-Cs hydrogels, while a small cut was observed in the Surgicel® group. No residues were found for Curaspon®, Surgicel®, or CDPE and CDPE-Cs hydrogels after one week of implantation, indicating that complete degradation of these materials had occurred. Necrosis and tissue damage could be observed only in the group treated with the conventional gauze dressings, and as expected, the conventional gauze remained intact after one week of implantation. Normal histological structures were observed in the groups, except for the livers implanted with the conventional gauze dressings and blank CDPE hydrogels, where significant inflammation was observed (Figure III.9).
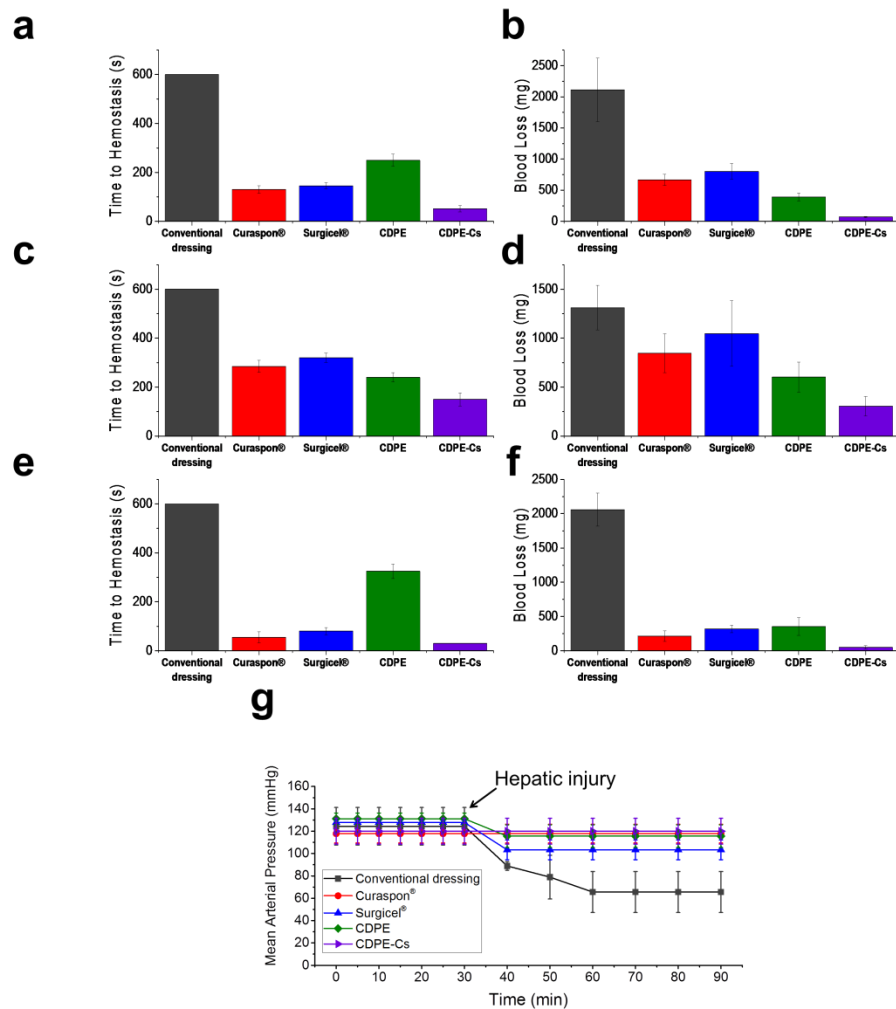
Figure III.7. *In vivo* examination of CDPE-Cs hydrogels against several controls indicated significant hemostatic efficacy of the CDPE-Cs wound dressings. Conventional dressings, Curaspon®, Surgicel®, and CDPE and CDPE-Cs hydrogels were applied immediately after induction of the liver injury and absorption of the initial bleeding from the injury sites, to determine the total time to hemostasis in rats (a), rabbits (c) and pigs (e), as measured over 10 min. The total amounts of blood loss in rats (b), rabbits (d) and pigs (f), were also measured. (g) The mean arterial pressure of the rabbits were monitored over 90 min, where the measurements over the first 30 min represent the mean arterial pressure of animals before induction of the liver injury.

50

Figure III.8. Photomicrographs of the livers from rats after treatment with selected hemostatic dressings and control untreated animals. Conventional gauze dressing, Curaspon®, Surgicel®, and cyclodextrin-chitosan (CDPE-Cs) hydrogels were applied immediately after the gauze-based absorption of the initial bleeding from the injury sites.

This work outlined the synthesis of a hyperbranched polyester hydrogel derived from β-cyclodextrin and its ability to load and assemble dissolved chitosan within its highly complex, porous network. We established the ability of the CDPE templates to degrade under physiological conditions, and further demonstrated the bioabsorbability and hemostatic efficacy of the chitosan-loaded (CDPE-Cs) composite hydrogels, when used as wound dressings, in acute liver punch models in rats, rabbits, and pigs. Significantly shorter times to hemostasis and reduced blood loss were observed in rats and rabbits, when compared to conventional gauze dressings and commercially available bioabsorbable dressings. The hemostatic property of chitosan, and the enhancement of this effect by increasing surface area, is well understood, however the assembly of chitosan into the nanofibers observed in this work is likely due to a complex array of competing factors.

Due to the intricate interplay of competing forces, a wide range of microstructures have been observed by various chitosan assembly methods, with contributions from both complexation and aggregation.[124] Chitosan is only water-

51

soluble in its polycationic form, where its deacetylated glucosamine groups must be sufficiently protonated to allow repulsive double-layer forces to overcome attractive forces.[125] It was, therefore, initially proposed that the assembly of aqueous chitosan solutions observed in the presence of certain anions was due to ionic complexation.[126] However, it was later determined that a physical gelation mechanism likely contributed to its assembly behavior, due to transfer of protons from chitosan to the anions, enabling the domination of attractive interchain forces.[125] It is expected that the assembly of chitosan within the confines of the microstructured CDPE template further convoluted its assembly behavior, and ultimately allowed access to novel structures presented in this work.

CDPE, itself, did not exhibit nanoscale features, and instead appeared as a porous matrix with micron-scale features (Figure III.4b). The templated chitosan did seem to exhibit a honeycomb-like appearance (Figure III.4d), which may be due to the packing of chitosan within the interstices of the CDPE network, however the much smaller nanofibrillar features could not have been produced by physical imprinting alone. Chitosan nanofibers and nanofibrous mats have been previously reported,[127-128] but they are typically only accessible by electrospinning, and the lowest average fiber diameters reported by these methods, *ca*. 58 nm,[129] are still larger than the *ca.* 9.2 nm fibers obtained in this work. However, nanofibers of the closely related chitin have been produced with sub-10 nm diameters, merely by precipitation into a solvent that disrupts hydrogen bonding,[130-131] and this phenomenon may provide insight into the assembly behavior observed herein. To promote the physical assembly of chitosan chains by

proton exchange and complexation phenomena, CDPE frameworks were designed with dianhydride linkers, rather than functionalities such as diacyl halides, to provide remaining carboxylate groups in the matrix sites to potentially interact with chitosan. When exchanged into water, the CDPE templates exhibited a tendency to curl slightly at the edges, despite being cast as flat, thick sheets. It was reasoned that this behavior was due to an increase in hydrogen bonding in the hydrogels, as although DMSO is a polar solvent, it does not contain an electropositive hydrogen to participate in hydrogen bonding as strongly as polar protic solvents, like water. When submerged in the chitosan solution, the CDPE hydrogels slowly uncurled to their original shape. Though some contribution to the shape restoration was likely due to the slight swelling induced by the loading of chitosan polymer chains into physical vacancies in the CDPE network, it is reasonable to expect this behavior to be, in part, due to the competition of chitosan with water for interaction with the CDPE network, which may disrupt hydrogen bonding with the solvent. Ionic exchange, or complexation, between the protonated amine groups of chitosan and carboxylate sites in the CDPE template may, then, enable the increase in attractive interchain forces of chitosan, conceivably enabling aggregation and the formation of the observed features. Therefore, although macroscopic features of the chitosan were attributed to physical templating by CDPE, the manifestation of nanofibrillar structures was ascribed to assembly of the chitosan chains within the interstices of the porous matrix, and was, correspondingly, only observed in discrete, confined regions of the network (Figure III.4e).

Degradation of the CDPE framework proceeded under alkaline conditions, through hydrolytic cleavage of the ester linkages between cyclodextrin moieties. Though ester hydrolysis can also proceed under acidic conditions, fragmentation of CDPE was not observed over 7 d when exposed to the mildly acidic chitosan solution, and only minor degradation of CDPE was observed by NMR spectroscopy and turbidity measurements in a 1% acetic acid solution over the same time period (Figure III.5). Derivatives of biphenyltetracarboxylic acid, the ring-opened form of the dianhydride linker, were formed as byproducts in the hydrolysis reaction, along with β-cyclodextrin derivatives (Figure III.2a, III.10). The byproducts were soluble in PBS, used to emulate physiological conditions, with CDPE forming a clear solution after 7 d of exposure. Although the analogous dissolution in PBS for CDPE-Cs composite hydrogels was not observed—even after 14 d—physiological degradability was observed during *in vivo* studies. Residual CDPE or CDPE-Cs hydrogels could not be observed after 1 week of implantation, likely indicating the importance of the *in vivo* microenvironment in providing for biodegradability *vs*. PBS hydrolytic stability *in vitro*. In histopathological examinations of the tissue surrounding the injury sites in rats, no inflammation was observed for the CDPE-Cs hydrogel group, suggesting biocompatibility for the wound dressing (Figure III.9).

In summary, the appearance of nanoscale features in chitosan mats by assembly within a β-cyclodextrin-derived hydrogel carrier template is reported. The assembled chitosan exhibited a honeycomb-like macroscopic morphology, and heavily entangled nanofibers, with diameters 9.2 ± 3.7 nm, were observed within the cavities of the

54

structures. The CDPE carriers were designed to degrade hydrolytically under physiological conditions, and the efficacy of chitosan-loaded CDPE-Cs hydrogels as wound dressings in several animal models was demonstrated, in which shorter times to hemostasis and reduced blood loss were observed. These composite hydrogels are expected to provide a chitosan-based hemostatic technology, with a novel, degradable delivery vessel, as biocompatible and bioabsorbable wound dressings for the reduction of blood loss in trauma scenarios.
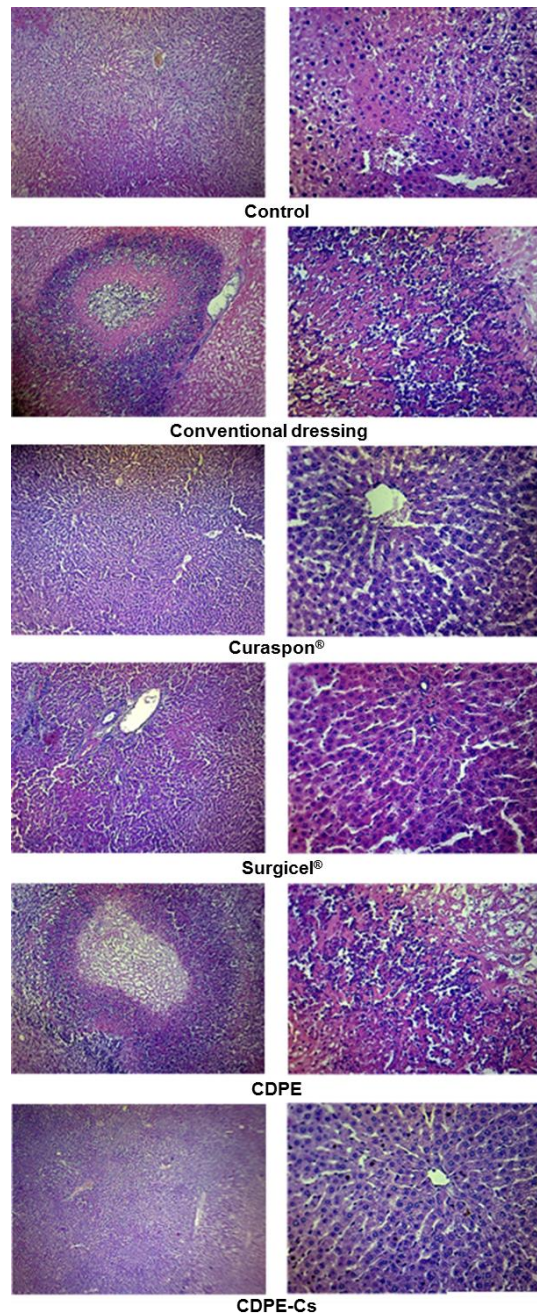
Figure III.9. Photomicrographs of the histological structures of the livers from rats after treatment with selected hemostatic dressings (H & E stain, × 10, left; × 40, right). Conventional dressing, Curaspon®, Surgicel®, CDPE, and CDPE-Cs were applied immediately after the gauze-based absorption of the initial bleeding from the injury sites. One week after the implantation of the various hemostatic agents, the tissues surrounding the livers were examined.
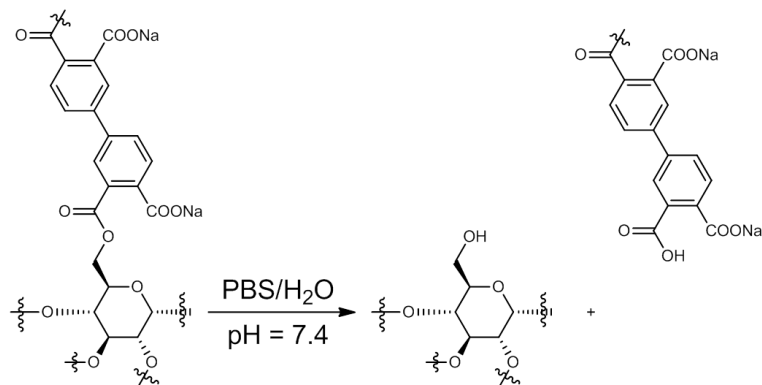
Figure III.10. Scheme detailing a potential ester hydrolysis reaction, shown for a single CD repeat unit, yielding the ring-opened byproduct of the aromatic linker and regenerating the hydroxylic cyclodextrin moiety.
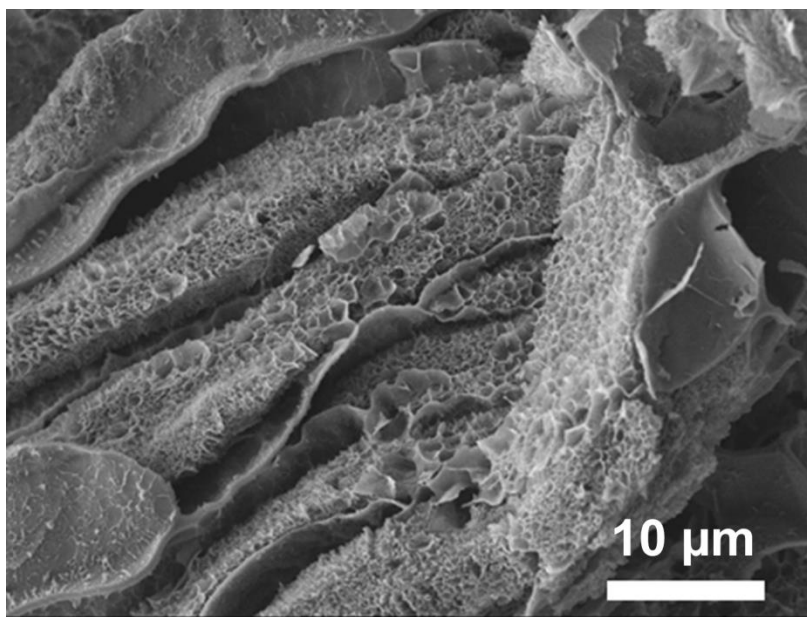
Figure III.11. Additional SEM image of lyophilized CDPE template.

3.3 Experimental

3.3.1 Materials

Acetic acid (glacial), anhydrous dimethyl sulfoxide (DMSO), benzene, phosphate-buffered saline tablets, 3,3',4,4'-biphenyltetracarboxylic dianhydride (BPDA), ethanol, methyl benzoate, heparin sodium, formalin solution (neutral buffered, 10%), triethylamine (Et$_3$N), urethane, sodium chloride (NaCl), paraffin, deuterium oxide (D$_2$O), acetic acid-d$_4$, sodium hydroxide (NaOH), and chitosan (molar mass 310–375 kDa) were purchased from Sigma-Aldrich and used as received. β-Cyclodextrin was obtained from TCI America and dried *in vacuo* at 70 °C for 12 h prior to use. Nanopure water (18.2 MΩ•cm) was acquired from an EMD Millipore Milli-Q water filtration system.

3.3.2 Characterization

Solution-state ^{1}H and ^{13}C NMR spectra were collected on a Varian Inova 500 spectrometer at room temperature. Solid-state cross-polarization magic angle spinning (CP-MAS) ^{13}C NMR spectra were obtained on a Bruker Avance 400 spectrometer with a 4 mm rotor at a spin rate of 10.0 kHz. The instruments were interfaced to a LINUX computer using VNMR-J software, and spectra were processed with MestReNova version 9.0.1-13254 by Mestrelab Research S.L. Attenuated total reflection Fourier-

transform infrared (ATR-FTIR) spectroscopy was performed on a Shimadzu IR-Prestige-21 spectrometer at a 1.0 cm^{-1} resolution. Thermogravimetric analysis (TGA) was performed on a Mettler-Toledo TGA 2 with a heating rate of 10 °C min^{-1} under argon atmosphere. Scanning electron microscopy (SEM) images were collected on a JEOL JSM-7500F FE-SEM equipped with a high brightness conical FE gun and a low aberration conical objective lens after platinum/palladium sputtering of the sample. Powder X-ray diffraction (PXRD) spectra were obtained on a Bruker D8 ADVANCE instrument with a Bruker LYNXEYE detector, with a 1 kW Cu X-ray tube, maintained at an operating current of 40 kV and 25 mA, operated in Bragg-Brentano para-focusing mode. Turbidity measurements were performed on a Shimadzu UV-2550 spectrophotometer at 450 nm with polystyrene cuvettes. Dynamic light scattering (DLS) measurements were performed on a Malvern Zetasizer Nano ZS with polystyrene cuvettes. Elemental analysis was performed at Midwest Microlab, LLC in Indianapolis, IN.

3.3.3 Synthesis and Degradation Studies

CDPE hydrogel template synthesis: To a flame-dried round-bottom flask equipped with a stir bar was added β-cyclodextrin (1.750 g, 1.542 mmol), triethylamine (0.468 g, 4.62 mmol), and anhydrous dimethyl sulfoxide (14.42 mL). After dissolution, BPDA (1.361 g, 4.626 mmol) was added in one portion. The mixture was stirred for 5 min until the solids were evenly distributed throughout the mixture. The suspension was

then poured into a shallow glass dish and heated to 70 °C on a hot plate for 2.5 h. After complete gelation, the system was allowed to return to room temperature. The gel was removed and cut to the desired shape with a razor blade and soaked in an excess of dimethyl sulfoxide for 1 h. The solvent was removed and exchanged with fresh dimethyl sulfoxide three additional times for 1 h each before placing the gel in an excess of water. The gel was then soaked in a saturated aqueous sodium chloride solution three times for 1 h each, before soaking three additional times in water for 1 h each. Samples were stored in water, or dried by lyophilization for characterization. ^{13}C CP-MAS NMR (101 MHz, spin rate 10.0 kHz, ppm) δ 237.65–225.48, 179.16–160.74, 145.71–120.24, 105.51–92.82, 87.50–52.05. FTIR (cm^{-1}): 3678–3015, 2927, 1776, 1710, 1603, 1576, 1363, 1289, 1245, 1145, 1077, 1032, 1002, 944, 845, 792, 769, 705. TGA: 25–90 ºC, 6% mass loss; 90–235 ºC, 4% mass loss; 235–280 ºC, 29% mass loss; 280–330 ºC, 11% mass loss; 330–390 ºC, 14% mass loss; 390–465 ºC, 8% mass loss; 465–500 ºC, 10% mass loss; 18% mass remaining above 500 ºC. Anal. calcd. for $(C_6H_{10}O_5)_1 \cdot (C_{14}H_{12}O_8Na)_6 \cdot (H_2O)_6 \cdot (NaCl)_{0.5}$: C, 47.27; H, 4.14; N, 0.00; Na, 6.53. Found: C, 47.64; H, 4.23; N, 0.00; Na, 6.80.

CDPE stability and degradation study: A phosphate-buffered saline tablet was dissolved in the corresponding amount of deuterated water to obtain a solution of 0.01 M phosphate buffer, 0.0027 M potassium chloride, and 0.137 M sodium chloride. A small, intact portion of lyophilized CDPE was cut to size by razor blade and placed in an NMR tube with the PBS D$_2$O solution to obtain a concentration of 15.0 mg mL^{-1}. The sample was then gently agitated at 37 °C (60 rpm), and analyzed by 1H NMR spectroscopy at 24

h intervals. After 7 d, the solution was transferred to a cuvette, and transmittance at 450 nm was measured to quantify turbidity, followed by dynamic light scattering measurements. A second sample was analogously prepared from lyophilized CDPE and 1 % acetic acid in D_2O, at a 15.0 mg mL^{-1} concentration, and analyzed by ^1H NMR spectroscopy at 24 h intervals, with storage at room temperature without agitation.

Chitosan loading to afford composite CDPE-Cs hydrogels: A chitosan solution was prepared by the dissolution of 5.000 g chitosan in 500.0 g acetic acid solution (1 *wt.*% in nanopure water) to obtain a 1 *wt.*% solution. After stirring for 24 h at room temperature, aqueous sodium hydroxide (5 M) solution was added dropwise, with vigorous stirring, until a pH of 5.5 was obtained. Pre-cut CDPE gels were submerged in the chitosan solution in a glass dish, and allowed to stand at room temperature for 7 d. Loaded gels were rinsed with water and lyophilized for characterization by IR spectroscopy and TGA. FTIR (cm^{-1}): 3678–3015, 2927, 2853, 1710, 1653, 1576, 1363, 1295, 1245, 1154, 1077, 1032, 944, 894, 845, 769, 705. TGA: 25–135 ºC, 12% mass loss; 205–360 ºC, 43% mass loss; 360–500 ºC, 12% mass loss; 33% mass remaining above 500 ºC.

CDPE template removal for characterization of the templated chitosan mats: Template removal was achieved by soaking lyophilized loaded gels in 100 mL aqueous NaOH solution (5 M) for 15 min, followed by rinsing with an excess of water. The resulting chitosan monolith was then dried *in vacuo* before characterization. The masses of the lyophilized CDPE-Cs composite gel and resulting dried templated chitosan mat

were both measured to determine the mass loss during template removal, and to estimate the chitosan concentration in the composite material. For solution-state NMR spectroscopy of the templated chitosan, *ca*. 15 mg of the material was sonicated in deuterated trifluoroacetic acid until dissolved. ^{1}H NMR (500 MHz, CF_3COOD, ppm) δ 5.56-8.85 (m, 2H), 4.74–3.13 (m, 12H), 2.26–2.12 (m, 3H). ^{13}C CP-MAS NMR (101 MHz, spin rate 10.0 kHz, ppm) δ 172.82, 110.78–95.86, 87.86–69.17, 66.02–55.74, 25.49–18.06. FTIR (cm^{-1}): 3647–2997, 2920, 2853, 1647, 1571, 1471, 1417, 1378, 1319, 1153, 1065, 1030, 992, 947, 895, 805. TGA: 25–90 ℃, 9% mass loss; 90–200 ℃, 3% mass loss; 200–325 ℃, 43% mass loss; 325–500 ℃, 16% mass loss; 29% mass remaining above 500 ℃.

3.3.4 In Vivo Evaluation of Hemostatic Efficiency

Animals were purchased and kept at room temperature, and allowed food and water ad libitum. The protocol was approved by the Assiut University Animal Ethical Committee (Ethical approval number 1730030). Animals were maintained under general anesthesia during the duration of experiments and euthanatized while under anesthesia at the end of the experiments.

Rats: The acute liver punch biopsy model was developed as described previously[132-133] (with slight modifications, to evaluate the biocompatibility/biodegradation of the developed hemostatic hydrogel and to examine the hemostatic efficiency *via* measurements of the time to hemostasis

and blood loss). Adult Sprague-Dawley rats (*ca.* 300 g) were anaesthetized with an intraperitoneal injection of sodium thiopental (50 mg kg-1) and their abdominal hair was shaved. The rats were divided into five groups (n = 6 per group). After opening the abdomen, the liver was exposed and an incision of *ca.* 1 cm in diameter, at an angle perpendicular to the tissue to a depth stop of *ca.* 0.3 cm, was produced on the liver. The tissue in the center of the injury site was removed using forceps and surgical scissors. Sterile gauze was used to absorb initial bleeding, and then, conventional gauze, Curaspon®, Surgicel®, CDPE and CDPE-Cs hydrogels were implanted into the injury site. A blade inserted onto a syringe was utilized to induce the injury, and to cut the gauze, sponge, and hemostatic hydrogels to match the dimensions of the wound (*i.e. ca.* 1 cm in diameter × 0.3 cm in depth). Several pieces were applied from the conventional gauze, Curaspon®, and Surgicel®, and bleeding was evaluated every 30 s for 10 min. CDPE and CDPE-Cs hydrogels were applied only once. The time to hemostasis and blood loss were measured. The hemostatic time was recorded as the last time of application where bleeding was not observed from the injury site. Weights of the dressings before and after applications were recorded to calculate the amount of blood loss. For hydrogels, blood loss was calculated based on the bleeding from the injury that was absorbed into the surrounding gauze. For biocompatibility/biodegradation studies, the conventional gauze dressings, Curaspon®, Surgicel®, and CDPE and CDPE-Cs hydrogels were implanted and left inside the liver after the first application. The initial bleeding was absorbed with gauze. The abdomen was then closed with sutures, and the area was sterilized with povidone iodine. After one week, the sutures were removed and

63

the liver was visually examined for wound healing. The animals were euthanized at the end of the experiments, and specimens from the liver tissues surrounding the injury sites were harvested for histological examination. Tissues were fixed immediately in 10% neutral formalin for 24 h, washed in running tap water for at least 2 h, and then immersed in 70% ethanol. Dehydration in ascending concentrations of ethanol (*i.e.* 70, 90, 95 and 100%) was carried out, followed by clearing the specimens in double embedding (1 g celloidin dissolved in 100 mL methyl benzoate, three changes for 3 d). The specimens were then washed in benzene (two changes, each for 15 min). Impregnation in paraffin was performed, followed by embedding the specimens in hard paraffin. Sections of 5 μm thickness were prepared using a rotary microtome (CUT 4050, microTec Laborgeräte GmbH, Walldorf, Germany). Specimens were stained with Hematoxylin and Eosin (H & E) stain for histological examination and imaged by Olympus BX53 light microscope (Olympus Co., Tokyo, Japan).

Rabbit studies: Adult rabbits (*ca.* 2 kg) were kept in large cages and were anesthetized with intraperitoneal injection of urethane (1 g kg^{-1}) prior to the surgical procedures. Rabbits were divided randomly into five groups (n = 6 per group) and treated exactly as mentioned in the *in vivo* rat section (*vide supra*). In addition to measuring the time to hemostasis and blood loss, the mean arterial blood pressure was monitored during the surgical procedures. A 20-gauge catheter was surgically cannulated into the right carotid artery and the mean arterial pressure (MAP) was recorded continuously under general anesthesia before the liver injury and for 1 h after the injury. Blood pressure was monitored on a polygraph using the Universal

Oscillograph (Harvard Apparatus, South Natick, MA). A heparinized rabbit model was utilized at a certain dose of heparin (*i.e.* 250 IU kg^{-1}) to achieve bleeding that would not stop spontaneously after the liver injury.

Pig studies: Pigs (*ca.* 50 kg) were anesthetized with intraperitoneal injection of sodium thiopental (50 mg kg^{-1}). Identical procedures were performed to evaluate the time to hemostasis and blood loss, as mentioned previously. Six pigs were utilized, and five incisions were performed in each one, as previously described, and conventional gauze, Curaspon®, Surgicel®, and CDPE and CDPE-Cs hydrogels were applied.

Values are presented as the mean ± standard deviation (SD) of at least six independent experiments. Significant differences between groups were evaluated by one-way ANOVA followed by Tukey's multiple comparison tests. Differences between different groups were considered significant for *p* values less than 0.05.

CHAPTER IV

DETERMINISTIC FILM TOPGRAPHIES AND POROSITIES BY THE

EXTRACTION OF MOLECULAR BRUSH POLYMERS

4.1 Introduction

Thin films with tailor-made porosities, surface topographies, and roughness are critical to a number of application areas including antireflective coatings,[43] nanopatterning,[134-135] and separation membranes.[136] Of particular interest *en route* to obtaining nanostructured polymer thin films are "top-down" techniques that are high throughput and compatible with current industry processes. "Top down" production methods of nanoporous polymer thin films generally involve the exploitation of some phase incompatibility, in which block copolymers are driven to self-assemble into microphase-separated structures to relieve unfavorable free energy of mixing.[137-138] The subsequent selective removal of one of the domains yields void spaces, which can often be achieved with orientation-specific control and long-range ordering.[139] However, this approach is limited by the discrete topologies determined by thermodynamic equilibrium for each system, which yield limited control over the pore structure by manipulation of the volume fraction for each domain. Furthermore, these types of phase-separated structures have relatively low surface areas, where void spaces are confined in isolated pores due to the nature of the microphase-separated structures.

The use of miscible precursors in the preparation of nano-corrugated thin films was reported as early as 2001.[54] Interestingly, such an approach for inducing porosity and surface roughness in films has seemingly remained unexplored. The selective removal of a domain distributed homogeneously throughout a matrix is expected to allow the formation of thin films with void spaces determined by precise control over the volume fraction of the extracted domain. A favorable interaction of the extractable domain with the matrix polymer is anticipated to enable the formation of pores whose interconnectivity increases with volume fraction, enabling access to films with large surface areas and high permeabilities. Molecular bottlebrush polymers were identified as a promising candidate for these extractable porogenic domains, as they provide a versatile platform for tailoring the molecular topology, dimensions, and chemical properties of these components—in turn yielding great control over the surface topography and porosities of the resulting films.[140-141]

It was hypothesized that the selective extraction of these bottlebrush polymers from an inert, chemically compatible matrix polymer could be achieved by the utilization of acid-labile hydrophobic protecting groups, enabling a solubility modulation of the brushes when exposed to acid. Protected brushes could, then, be cast with a compatible, hydrophobic matrix polymer to form homogeneous films in which the resulting morphology is kinetically trapped. Upon acid exposure, triggering the removal of the hydrophobic protecting groups to expose hydrophilic groups, brushes could then be selectively extracted by rinsing with an aqueous base solution (Figure IV.1). This system was envisioned in pursuit of films with porosities and surface architectures

predetermined by the volume fraction, molecular topology, and chemical properties of the removable component. This system may also enable further control over the film topography, *e.g.* the controlled alignment of features by the spatial-specific inclusion of surface-directing groups to the sacrificial brush polymer, as has been previously demonstrated.[140-141]
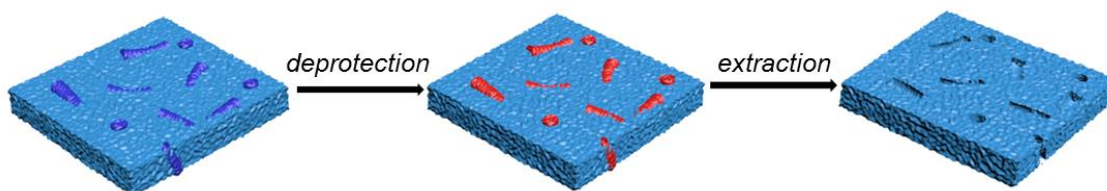
Figure IV.1. Illustration of the selective extraction of bottlebrush polymers to produced tailored film topographies.

4.2   Results and Discussion

Bottlebrush polymers were synthesized by a "grafting-through" approach *via* orthogonal reversible addition-fragmentation chain transfer (RAFT) and ring-opening metathesis polymerization (ROMP) steps (Figure IV.2). 1-Ethylcyclopentyl methacrylate (ECPMA) was chosen as the acid-sensitive moiety, as it has been established to undergo deblocking under acidic conditions to reveal the hydrophilic acrylic acid group.[141] A norbornenyl-functionalized chain transfer agent (CTA) was synthesized according to literature methods,[142] and RAFT polymerization of ECPMA, with azobisisobutyronitrile (AIBN) as a radical source, yielded norbornenyl-

functionalized macromonomers (Nb-PECPMA) with excellent control. ROMP of Nb-PECPMA could then be readily achieved with Grubbs 3rd generation catalyst, affording bottlebrushes polymers with narrow dispersities.
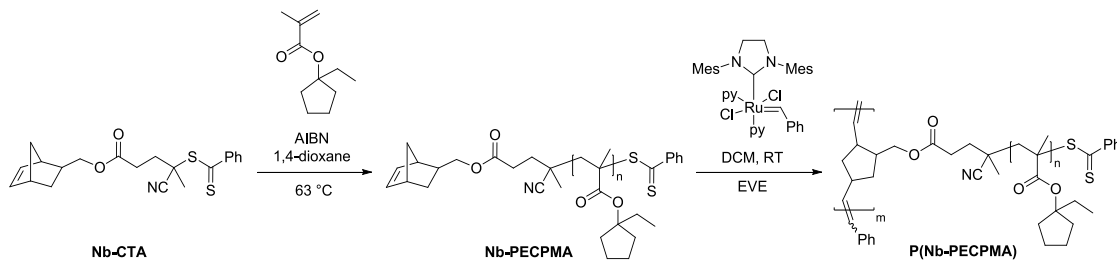
Figure IV.2. Synthetic overview of molecular bottlebrushes with hydrophobic, acid-labile protecting groups.

Of the brushes synthesized, P(Nb-PECPMA$_{35}$)$_{25}$ was selected for further studies. The number average molar mass determined by size exclusion chromatography (SEC) was in close agreement with the theoretical value according to the reaction stoichiometry. A trace amount of macromonomer was observed by SEC (Figure IV.3c), however NMR spectroscopic analysis indicated the complete consumption of the norbornenyl groups, as evidenced by the disappearance of the peak at 6.20 ppm (Figure IV.3a, b). This likely indicated the presence of a small amount of PECPMA chains without norbornenyl chain-ends, prohibiting their inclusion in the brush polymer product. FTIR spectroscopy revealed nearly identical spectra for the macromonomer and brush polymers, save for the disappearance of the alkenyl C–H stretch at 707 cm^{-1} for the brush polymer, further confirming the complete consumption of the norbornenyl groups during ROMP (Figure IV.3d).

69
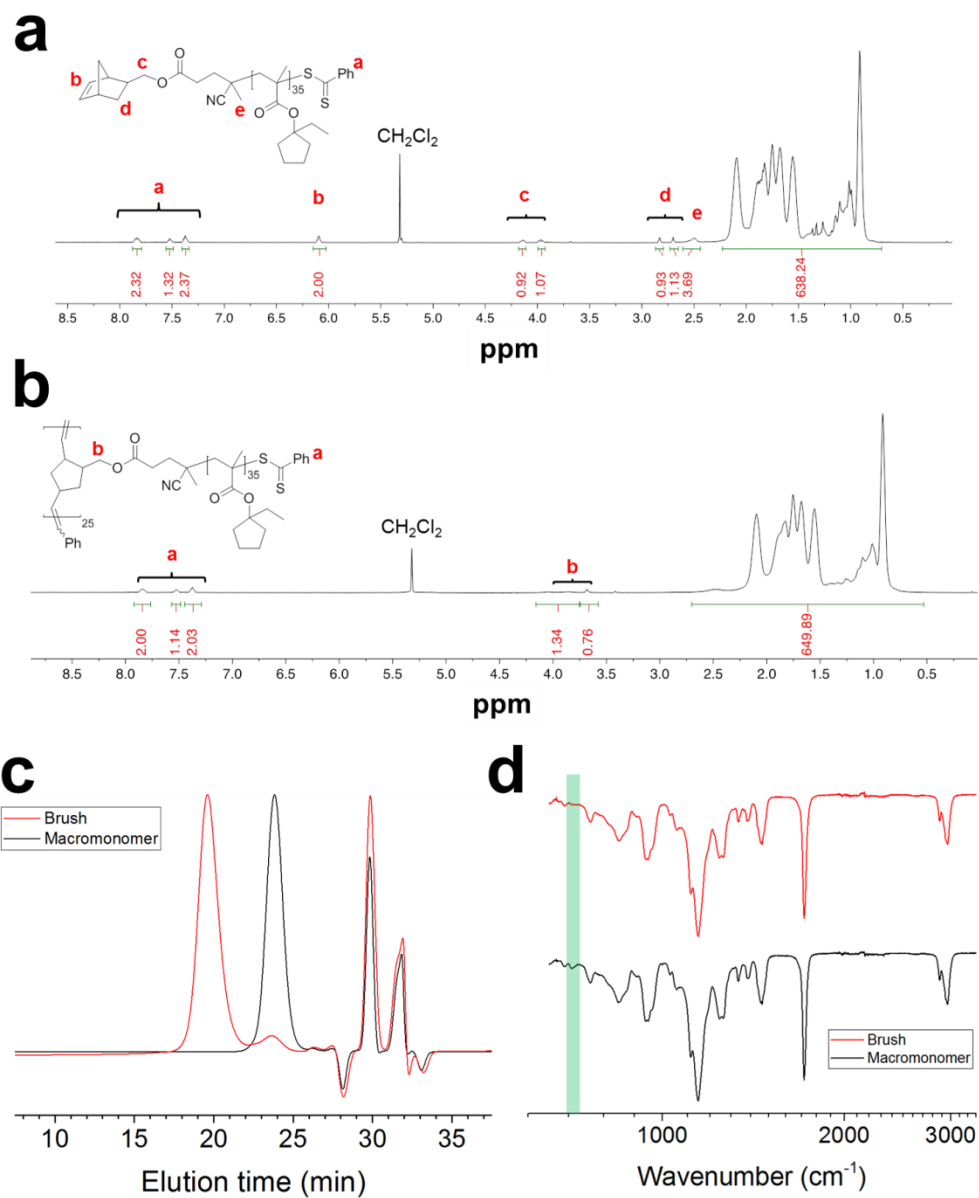
Figure IV.3. Overview of polymer characterization. (a) ^{1}H NMR (500 MHz, in CD$_2$Cl$_2$) spectra of macromonomer Nb-PECPMA$_{35}$. (b) ^{1}H NMR (500 MHz, in CD$_2$Cl$_2$) spectra of brush P(Nb-PECPMA$_{35}$)$_{25}$. (c) SEC traces for brush and macromonomer. (d) FTIR spectra of brush and macromonomer, with the alkenyl C–H stretch at 707 cm^{-1} highlighted.

P(Nb-PECPMA$_{35}$)$_{25}$ brushes were imaged by AFM, after deposition on highly oriented pyrolytic graphite (HOPG) (Figure IV.4), to provide a reference during further film studies. It was expected that developed films exhibit holes that reflect the dimensions observed during imaging of the individual brushes. The feature sizes observed by AFM were consistent with the theoretical contour lengths of *ca.* 20 nm, for brush diameter corresponding to the PECPMA sidechains, and *ca.* 12 nm, for length of the polynorbornene backbone, calculated from the theoretical degree of polymerization (DP) for each unit, respectively. Smaller features, from *ca.* 20 to 30 nm widths and *ca.* 10 to 20 nm lengths, corresponded to individual brushes, while the larger features observed likely corresponded to the aggregation of several brush polymers together.
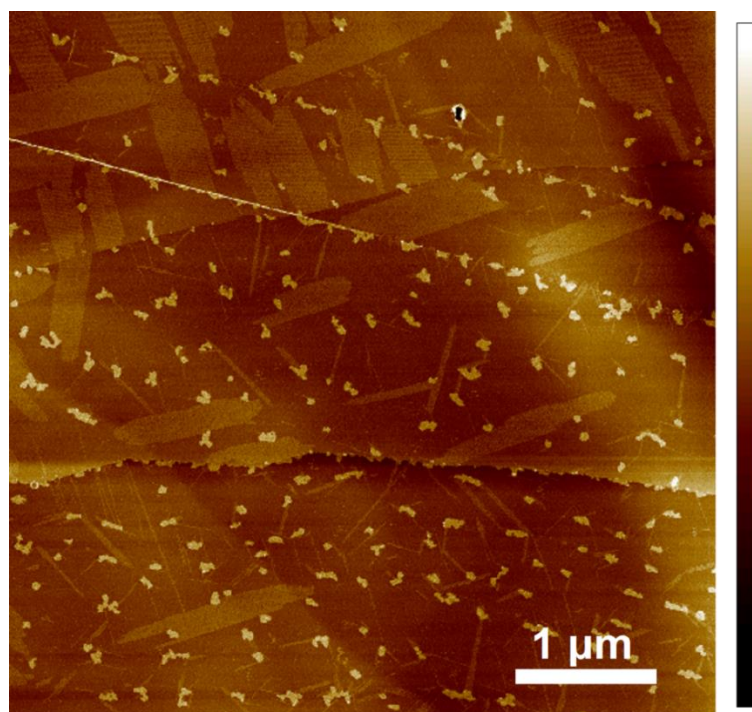
Figure IV.4. AFM height image of brushes, cast on HOPG (height scale bar ±2.5 nm)

Solution-state control studies were performed to verify the efficacy of acid-catalyzed deblocking of ECPMA and to confirm solubility of the methacrylic acid (MAA) product (Figure IV.5) in the aqueous developer. A small amount of the protected brush was dissolved in chloroform with *p*-toluenesulfonic acid monohydrate, 1:1 by mass, and the solution was stirred for 2 h at 40 °C. A pink precipitate slowly formed, and was collected by addition to diethyl ether. The product was freed of solvent *in vacuo* and analyzed by ^{1}H NMR, confirming the appearance of the acidic MAA proton and disappearance of the ethyl cyclopentyl protons. The product was readily dissolved in 0.2 M aqueous tetramethylammonium hydroxide (TMAH), chosen as the developer solution, forming a clear solution. These studies confirmed the ability of the brush polymer to undergo acid-catalyzed deblocking and validated the possibility of extraction by the aqueous developer.
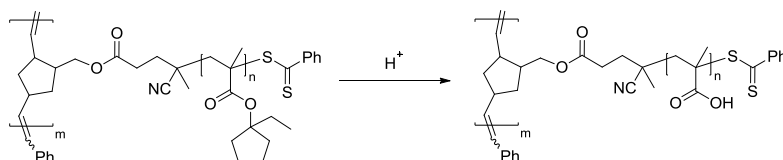
Figure IV.5. Overview of acid-catalyzed deprotection of P(Nb-PECPMA$_{35}$)$_{25}$ to afford P(Nb-PMAA$_{35}$)$_{25}$.

Several matrix polymers were explored in film studies, and poly(cyclohexyl methacrylate) (PCHMA) was ultimately selected for its compatibility with the brush polymer. PCHMA offered miscibility with the ECPMA brushes, owing to their chemical similarity, while maintaining stability to acid. Films were cast from 2 *wt.* % solutions in 2-heptanone, 3:1 matrix:brush by mass, on polystyrene-primed silicon (Si)

wafers. The films were briefly heated to 90 °C for 5 s to remove residual solvent and imaged by AFM (Figure IV.6). The resulting films were relatively smooth and featureless, confirming the phase compatibility of the two polymers. Cluster secondary ion mass spectrometry (SIMS) spatial correlation analysis was used to corroborate the miscibility of the two domains. Analyzed films exhibited colocalized signals for the brush and matrix species, indicating homogeneous distribution of the two domains at the film surface.
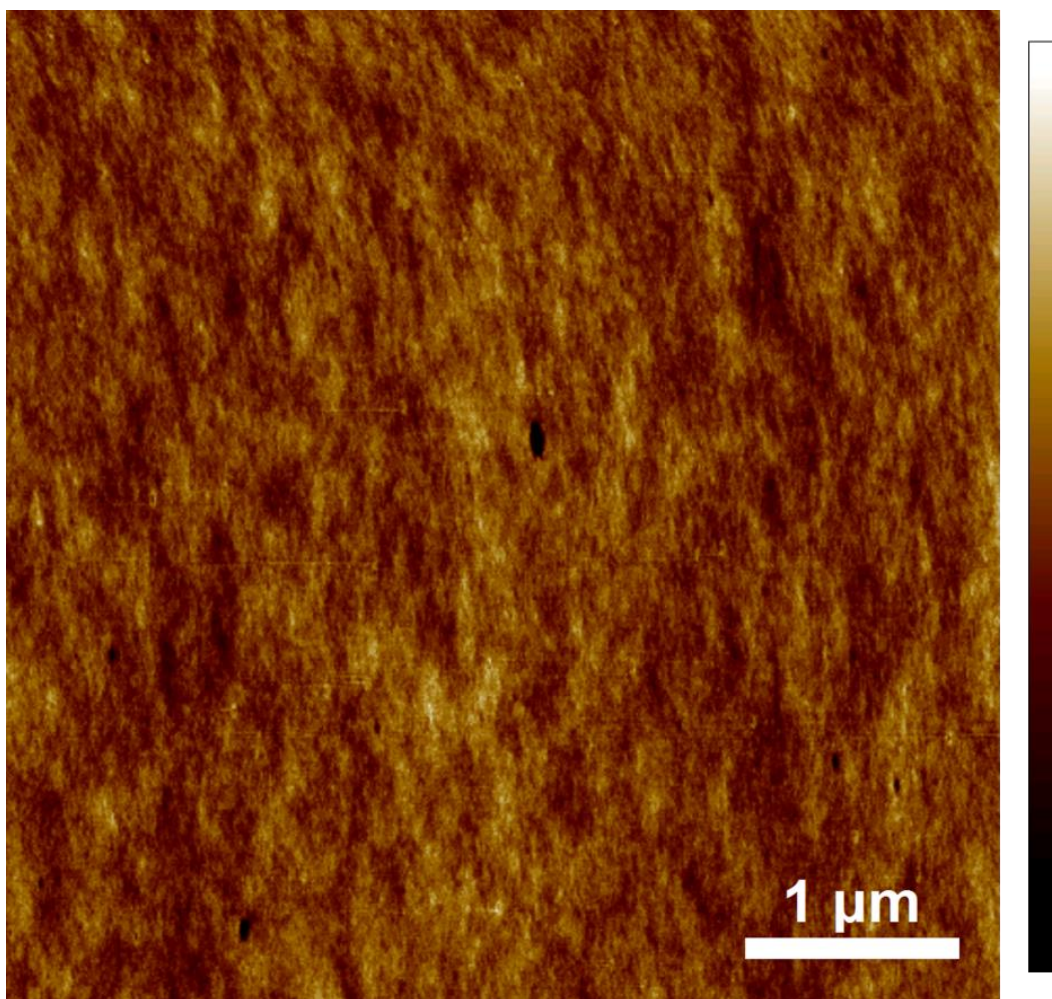
Figure IV.6. Height image of film comprising brush and matrix polymer, cast on PS-primed wafer, by AFM (height scale bar ±5.0 nm).

Film-state brush removal studies were then designed such that films of a known concentration of brush were prepared and imaged as-cast and after subsequent deblocking and development. The deblocking reaction was triggered by heating films, at 90 °C, for a predetermined amount of time, before development by rinsing in 0.2 M aqueous TMAH solution and water. Polystyrene-primed wafers were employed to increase the adhesion of the hydrophobic films to the substrate, preventing delamination of films during development. Many acid sources were evaluated, including photoacid generators, but ultimately *p*-toluenesulfonic acid (PTSA) was chosen for its increased miscibility with the brush and matrix polymers relative to other acids screened.

Matrix/acid only films were first prepared to confirm the resistance of the matrix film to the development conditions, and as a negative control study. Films were cast from a 4:1 matrix:acid solution (2 *wt.* % in 2-heptanone) and imaged before and after the chosen baking and development conditions (Figure IV.7). An increase in initial surface roughness, relative to the matrix/brush only films, was observed, and attributed to the increase in phase contrast between the hydrophobic matrix polymer and polar organic acid. Some minor features were observed throughout the study, and were ascribed to aggregation of the acid molecules at the surface of films. Films appeared slightly smoother after development, which was likely due to thermal annealing during the 90 °C bake.

74
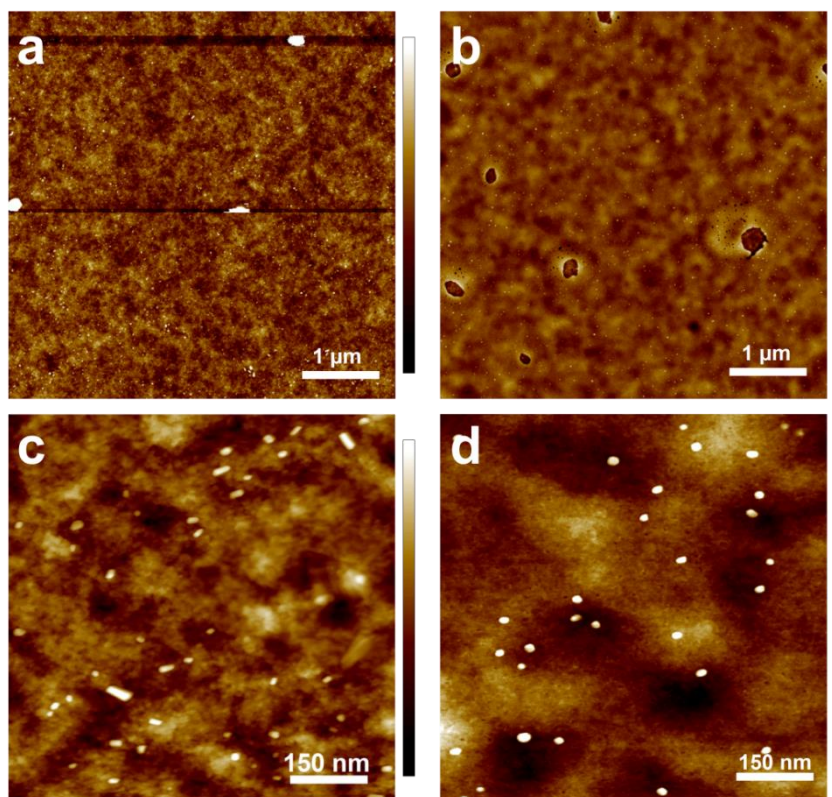
Figure IV.7. AFM height images of matrix/acid only films, 4:1 matrix:acid by mass (height scale bars ±10.0 nm). (a) Film as-cast, with 10 s post-application bake at 90 °C. (b) Film after development, with 5 min 90 °C bake followed by 0.2 M aqueous TMAH and water rinsing for 30 s each. (c) As-cast film, larger magnification. (d) Developed film, larger magnification.

Films containing brush were then studied, with an analogous polymer:acid mass ratio to the matrix/acid only films. A 3:1:1 by mass matrix:brush:acid solution was prepared at 2 *wt.* % in 2-heptanone and cast into films. The films were imaged as-cast and after development, as described previously (Figure IV.8). As-cast films exhibited similar surface morphologies to the matrix/acid only films, with the features attributed to minor surface aggregation of acid present as well. However, after development, a significant change in the film morphology was observed. The surface roughness

increased, contrasting what was observed in matrix/acid only films, and the appearance of holes, corresponding well with the size and shape of brushes, was noted. A change film thickness was also observed, from *ca*. 40 nm as-cast to *ca*. 31 nm after development.
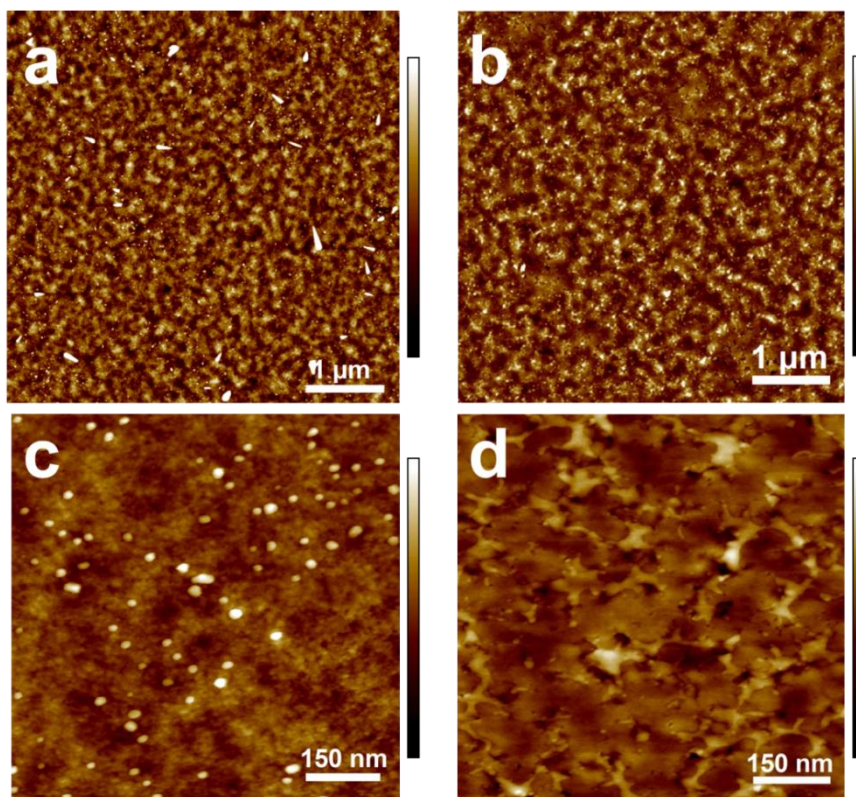
Figure IV.8. AFM height images of films comprising 3:1:1 matrix:brush:acid by mass (height scale bars ±10.0 nm). (a) Film as-cast. (b) Film after development, with 5 min 90 °C bake followed by 0.2 M aqueous TMAH and water rinsing for 30 s each. (c) As-cast film, larger magnification. (d) Developed film, larger magnification.

Cluster SIMS was used to track the presence of each chemical component of the film during development. A mass signal at *ca*. 113 amu, assigned to the anionic ECPMA fragment $C_7H_{13}O^-$, was found in the film as-cast, with its near-total disappearance observed after development (Figure IV.9a). A mass signal at *ca.* 99 amu,

assigned to the $C_6H_{11}O^-$ fragment of PCHMA, was used to track the presence of the matrix and was slightly increased after development, which may be due to the increased potential for ionization after development. Interestingly, the sulfite anion (*ca.* 80 amu) was also observed in comparable amounts in both as-cast and developed films, indicating its persistence even after the aqueous rinse.
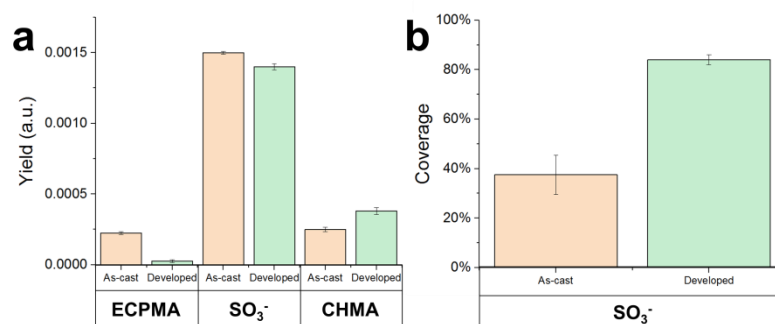
Figure IV.9. Cluster SIMS data for 3:1:1 (matrix:brush:acid by mass) film as-cast and after development. (a) Signal intensity for each species before and after development. (b) Degree of acid coverage before and after development.

Further studies were performed at varying concentrations of brush to determine if the resulting porosity of films could be controlled by regulation of the film composition. The addition of acid to the film, instead of later film exposure to acid after casting, hindered the formation of smooth films as the brush concentration was increased. Larger amounts of brush necessitated the addition of larger amounts of acid, and at relatively high concentrations of acid, *i.e.* 1:1:1 and 2:1:1 matrix:brush:acid by mass, significant phase separation was observed (Figure IV.10a–d). However, effective brush removal was observed, and a significant topography change was noted in these films after development, with the appearance of holes, again corresponding well with the

shape and size of brushes (Figure IV.10b, d). At lower brush/acid concentrations, *i.e.*

5:1:1 matrix:brush:acid by mass, phase separation was not observed, and similar features

were observed to the 3:1:1 composition, in as-cast and developed films.
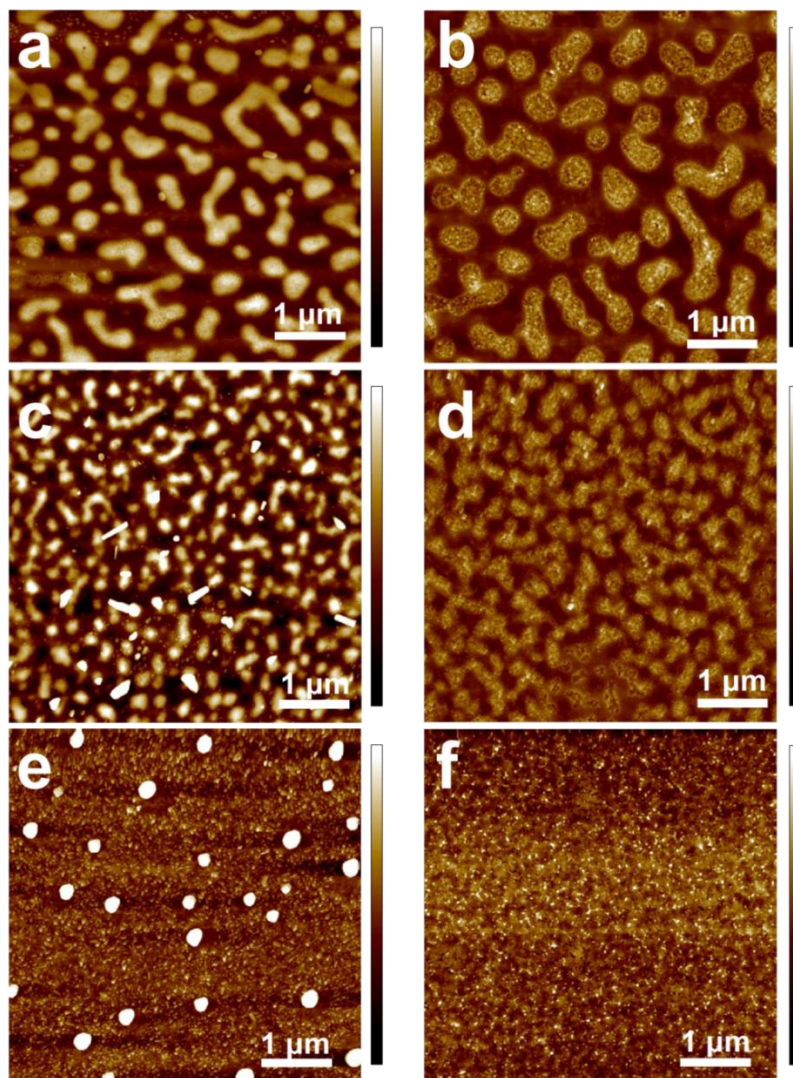
Figure IV.10. AFM height images of films. (a) 1:1:1 matrix:brush:acid by mass, as-cast (height scale bar ±40.0 nm). (b) 1:1:1 film after development (height scale bar ±20.0 nm). (c) 2:1:1 matrix:brush:acid by mass, as-cast (height scale bar ±20.0 nm). (d) 2:1:1 film after development (height scale bar ±20.0 nm). (e) 5:1:1 matrix:brush:acid by mass, as-cast (height scale bar ±10.0 nm). (f) 5:1:1 film after development (height scale bar ±10.0 nm).

Island formation in films with larger concentrations of acid was hypothesized to correspond to phase segregation between the polymer and acid domains. SIMS data supported this notion, as it was found that signals corresponding to the matrix and brush domains were colocalized, while signals corresponding to PTSA were negatively correlated. Despite the spatial separation of acid from brush, deprotection was still successful—likely indicating sufficient acid mobility throughout the film during the heating step that enabled interaction with the ECPMA moieties. The diffusion of acid throughout the film was confirmed in a SIMS experiment, and acid coverage was determined to be *ca*. 40% for as-cast films and *ca*. 85% after development (Figure IV.9b).

The observed island features provided a valuable basis of measurement. Feature heights in the 1:1:1 films, as-cast, were 37.9 ± 5.5 nm, and these islands comprised 40.4% of the film. After development, the heights were reduced to 14.9 ± 3.4 nm, with holes measuring 5.0 ± 1.8 nm in depth, with the islands corresponding to 43.9% of the film area. In 2:1:1 films, these features measured 26.8 ± 3.6 nm in height, with 31.8% coverage. After development the heights were again reduced to 14.2 ± 3.4 nm, with holes 4.6 ± 1.7 nm in depth, and the features covered 27.4% of the film surface. These dramatic changes in feature heights, with the retention of surface coverage, is consistent with the hypothesis that brushes are selectively removed, leaving behind the inert PCHMA matrix. SIMS data further corroborated selective brush removal, as the signal corresponding to the ECPMA fragment was significantly reduced after development, while the matrix signal again slightly increased (Figure IV.11). For the two films that

exhibited phase separated structures (1:1:1 and 2:1:1 matrix:brush:acid by mass), SIMS data indicated significantly increased acid removal during development, compared with the films that did not contain these features (Figure IV.11). This likely indicates difficultly in removing the acid from the hydrophobic matrix, whereas acid is effectively removed when isolated from the polymeric domains.
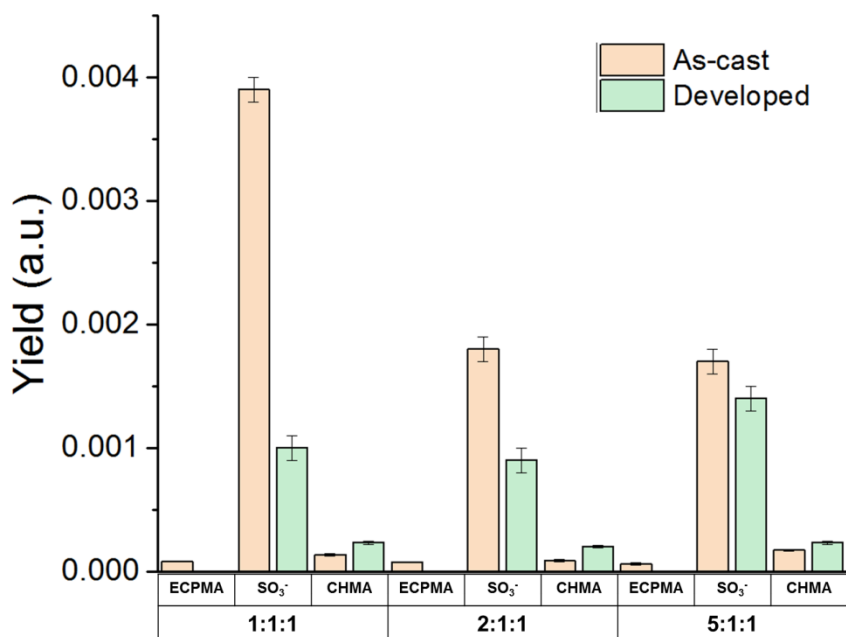
Figure IV.11. Cluster SIMS data for 1:1:1, 2:1:1, and 5:1:1 (matrix:brush:acid by mass) films, showing the signal intensity for each species before and after development.

In summary, the sacrificial polymeric porogens were successfully employed to control the surface topography of polymer thin films. Acid-sensitive ECPMA bottlebrush polymers were blended with an inert, chemically compatible PCHMA matrix and acid, before casting into films. At lower brush/acid concentrations, as-cast films were smooth, however, larger concentrations resulted in significant phase segregation between the acid and polymer domains. Despite this phase separation at larger

brush/acid concentrations, selective removal of the brush, resulting in brush-sized and shaped holes in the films, was successful at all compositions studied—demonstrated by AFM and SIMS studies. Conditions that diminish the effect of acid-induced phase segregation, such as downstream film exposure to acid as opposed to inclusion in the initial film composition, will be explored to enable access to systems with larger brush concentrations and improve the residual acid content in films after development. Though this imprinting strategy was demonstrated in thin films, it can conceivably be applied analogously in bulk materials. Furthermore, through the controlled installation of surface- and substrate-directing groups to the brush templates, this system is expected to provide a powerful synthetic platform *en route* to the introduction of highly tailored porosities and topographies to host materials.

4.3   Experimental

4.3.1 Materials

Grubbs second generation catalyst (G2), pyridine, azobisisobutyronitrile (AIBN), 4-dimethylaminopyridine, 4-cyano-4-(phenylcarbonothioylthio)-pentanoic acid, *exo*-5-norbornene-2-carboxylic acid, anhydrous 1,4-dioxane, PTSA monohydrate, TMAH, ethyl vinyl ether, lithium aluminum hydride, *N,N'*-dicyclohexylcarbodiimide, poly(cyclohexyl methacrylate) ($\bar{M}_w$ 65 kDa) were purchased from Sigma-Aldrich. Ethyl cyclopentyl methacrylate (ECPMA) and hydroxy terminated polystyrene ($\bar{M}_w$ 27 kDa)

were provided by DowDuPont. AIBN was recrystallized from methanol before use. ECPMA was passed through a basic alumina column before use. All other reagents were used as received. Si wafers were obtained from Addison Engineering, Inc.

4.3.2 Characterization

^{1}H and ^{13}C NMR spectra were collected in the solution state on a Varian Inova 500 spectrometer at room temperature. Spectra were processed with MestReNova version 9.0.1-13254 by Mestrelab Research S.L. ATR-FTIR was performed on a Shimadzu IR-Prestige-21 spectrometer at a 1.0 cm^{-1} resolution. Atomic force microscopy (AFM) was performed on an Asylum MFP-2D system (Oxford Instruments, Plc.) in tapping mode, with silicon tips (T190-25, VISTA probes; spring constant: 48 N m^{-1}, tip radium: 10 nm, resonance constant: 190 kHz).

SEC was performed on a Waters 1515HPLC equipped with a differential refractive index detector (Wyatt Technology, Optilab T-rEX) and a multi-angle laser light scattering (MALLS) detector (Wyatt Technology, DAWN HELEOS II, 658 nm), using ASTRA software (Wyatt Technology) and three-column series (Phenogel 5 µm; 100 Å, 104 Å, and Linear (2); 300×4.6 mm columns; Phenomenex, Inc.). Polymer solutions were prepared at a known concentration (*ca.* 5 mg mL^{-1}), and a 200 µL injection volume was used. After filtration through a 200 nm PTFE filter, samples were passed through the SEC system, equilibrated at 40°C in tetrahydrofuran, with a flow rate

of 0.35 mL min-1.   The dn/dc values of the analyzed polymers were determined from the differential refractometer response based on sample concentration.

Cluster SIMS data was collected on a custom-built massive cluster secondary ion mass spectrometer.[143] A gold liquid metal ion source and a Wien filter, installed on a 100 kV platform to increase the kinetic energy of the projectile, were used to generate a beam of mass selected Au_{400}^{4+} projectiles.[144] The projectiles were pulsed to a rate of *ca*. 1000 projectiles per second, and biased to -10 kV. The electrons generated during collision of the projectiles with the substrate were deviated by a weak magnetic field and collected on a microchannel plate-based detector, and were used to indicate the start of the time-of-flight mass spectrometry (TOF-MS) measurement. The negative secondary ions were accelerated toward a reflectron TOF-MS and collected by an eight-anode microchannel plate-based detector. The suite of start and stop signals were collected by a time-to-digital converter (TDCV4 Institute of Nuclear Physics, Orsay, France) operating in event-by-event mode. Mass spectra were collected before the subsequent projectile impact, termed the event-by-event bombardment/detection mode. Each film sample was analyzed in three discrete locations (125 μm radius) with 2×10^6 to 4×10^6 projectiles.

4.3.3 Synthesis and Film Studies

Preparation of *exo*-5-norbornene-2-methanol (Nb-OH): Synthesis of Nb-OH was performed according to a modified literature procedure.[145] To a flame dried round-

bottom flask was added *exo*-5-norbornene-2-carboxylic acid (5.053 g, 36.57 mmol) with 100 mL anhydrous tetrahydrofuran. The solution was cooled on an ice bath to 0 °C, followed by the slow addition of lithium aluminum hydride (2.104 g, 55.44 mmol). The solution was then removed from the ice bath and stirred at room temperature. After 12 h, 2 mL water was added dropwise, followed by 3 mL 10% aqueous sodium hydroxide. After a final addition of 6 mL of water to the solution, the mixture was filtered through a thin layer of celite to remove the solids. The filtrate was dried over sodium sulfate and freed of solvent under reduced pressure. The product was isolated by column chromatography (2:1 *v/v* pentane/diethyl ether), and obtained as a colorless oil (3.095 g, 68.14% yield). Characterization data was consistent with published data.[145]

Preparation of exo-5-norbornenylmethyl 4-cyano-4-(phenylcarbonothioylthio)-pentanoate (Nb-CTA): Synthesis of Nb-CTA was performed according to a modified literature procedure.[142] To a flame dried round-bottom flask was added 4-cyano-4-(phenylcarbonothioylthio)pentanoic acid (2.011 g, 7.198 mmol), 4-dimethylaminopyridine (0.118 g, 0.966 mmol),Nb-OH (1.093 g, 8.802 mmol) , and 40 mL anhydrous dichloromethane. The solution was cooled on an ice bath to 0 °C before the slow addition of *N,N'*-dicyclohexylcarbodiimide (1.873 g, 9.078 mmol). The solution was stirred for 1 h at 0 °C before allowing the vessel to warm to room temperature. After a further 48 h stirring at room temperature, the solids were removed over a thin layer of celite. The filtrate was washed with 100 mL saturated aqueous sodium bicarbonate solution followed by water. The organics were collected and dried over sodium sulfate before concentrating under reduced pressure. The product was

isolated by column chromatography (10% ethyl acetate in hexane), yielding a viscous red oil (2.119 g, 76.36% yield). Characterization data was consistent with published data.

Preparation of poly(ethylcyclopentyl methacrylate) macromonomer (Nb-PECPMA$_{35}$): To a flame-dried Schlenk flask was added ECPMA (702 mg, 3.85 mmol), Nb-CTA (51 mg, 0.13 mmol), AIBN (3.2 mg, 0.020 mmol), and 0.95 mL anhydrous 1,4-dioxane. The solution was deoxygenated by four cycles of freeze-pump-thaw before addition to a preheated oil bath at 63 °C. After 16.75 h, the reaction was quenched by submersion of the flask into liquid nitrogen. The solution was allowed to thaw and the product was collected by precipitation into MeOH at 0 °C. The product was further washed with MeOH and dried under reduced pressure, yielding a pink solid (244 mg). ^{1}H NMR (500 MHz, CD$_2$Cl$_2$ ppm) δ 7.83 (m, 2H), 7.55 (m, 1H), 7.42 (m, 2H), 6.20 (m, 2H), 4.33 (m, 1H), 3.98 (m, 1H), 2.80 (m, 1H), 2.68 (m, 1H), 2.50 (m, 3H), 2.22–0.85 (br, 639H). ^{13}C NMR (126 MHz, CD$_2$Cl$_2$ ppm) δ 172.32, 89.15, 42.86–41.20, 31.96–29.60, 20.97–18.27, 15.03–12.13, 4.29. FTIR (cm^{-1}): 3045–2829, 1716, 1458, 1386, 1336, 1264, 1243, 1145, 1113, 1053, 1031, 991–908, 887–785, 760, 707, 689. $M_{n\ SEC}$ 8.3 kDa, $Đ$ = 1.1.

Preparation of Grubbs third generation catalyst (G3): Synthesis of G3 was performed according to a modified literature procedure.[146] To a flame-dried round bottom flask was added anhydrous pentane. The solvent was bubbled with nitrogen for 30 min, followed by cooling on an ice bath at 0 °C. To a separate flame-dried vial was added G2 (248 mg, 0.301 mmol). The solids were degassed under reduced pressure and

backfilled with nitrogen before the addition of 1 mL pyridine by degassed syringe. The solution was allowed to stir at room temperature for 5 min before addition to 90 mL of the cold, degassed pentane by pipette. The solids were collected by centrifugation, and washed several times with cold pentane. The product was collected as a green solid, and dried and stored under reduced pressure (196 mg, 89.4% yield). Characterization data was consistent with published data.[146]

Preparation of ECPMA brush polymer (P(Nb-PECPMA$_{35}$)$_{25}$): To a flame-dried Schlenk flask was added G3 (0.77 mg, 0.0011 mmol) and 0.5 mL anhydrous DCM. The solution was deoxygenated by four cycles of freeze-pump-thaw. To a flame-dried vial was added Nb-PCEPMA (180 mg, 0.0266 mmol) and 1.7 mL anhydrous DCM. The solution was deoxygenated by four cycles of freeze-pump-thaw, before addition to the Schlenk flask by degassed syringe. The solution was allowed to stir at room temperature for 1.5 h before the addition of 0.15 mL ethyl vinyl ether by syringe. The solution was further stirred at room temperature for 1 h before collection of the product by precipitation into MeOH at 0 °C. The product was further rinsed with MeOH and dried under reduced pressure, yielding a pink solid (154 mg, 85.6% yield). ^{1}H NMR (500 MHz, CD$_2$Cl$_2$, ppm) δ 7.83 (m, 2H), 7.61 (m, 1H), 7.38 (m, 2H), 2.70–0.83 (br, 644H). FTIR (cm^{-1}): 3045–2829, 1716, 1458, 1386, 1336, 1264, 1243, 1145, 1113, 1053, 1031, 991–908, 887–785, 760, 689. ^{13}C NMR (126 MHz, CD$_2$Cl$_2$ ppm) δ 171.85, 89.15, 41.99, 32.20–29.98, 27.28–25.28, 20.71–18.67, 14.63–17.78, 4.31. $M_{n\ SEC}$ 170 kDa, $Đ$ = 1.2.

Solution-state acid deblocking control study: To a 10 mL shell vial was added P(Nb-PECPMA) (60.0 mg) and 2 mL chloroform. After dissolution of the polymer, PTSA monohydrate (60.2 mg, 0.316 mmol) was added in one portion. The solution was stirred at 40 °C for 1 h, before collection of the product by precipitation into cold diethyl ether. The product was rinsed with diethyl ether and freed of solvent *in vacuo*. The solid product was then dissolved in 0.2 M aqueous TMAH solution to confirm its solubility in the developer. ^{1}H NMR (500 MHz, DMSO-d_6, ppm) δ 7.82 (m, 2H), 7.65 (m, 1H), 7.50 (m, 2H), 4.09 (m, 1H), 3.94 (m, 1H), 3.72–3.23 (br, 38H), 2.82 (m, 1H), 2.68(m, 1H), 1.76–0.61 (br, 182H).

Imaging of brushes: A solution of P(Nb-PECPMA$_{35}$)$_{25}$ was prepared in a small vial at a concentration of 4 µmol L^{-1} in 2-heptanone. The solution was filtered through a 200 nm polytetrafluoroethylene (PTFE) syringe filter and cast on freshly cleaved HOPG at 1500 rpm for 15 s (2000 rpm s^{-1}), before imaging by AFM.

Preparation of PS-primed Si wafers: A native Si wafer was subjected to UV–O$_3$ surface treatment for 5 min. A 2 *wt.* % solution of hydroxy terminated polystyrene ($\overline{M}_w$ 27 kDa) in 2-heptanone was prepared and filtered through a 200 nm PTFE syringe filter. A film was cast on the oxidized wafer from the solution at (i) 500 rpm for 5 s and (ii) 3000 rpm for 30 s (2000 rpm s^{-1}). The wafer was then heated on a hot plate to 200 °C for 30 min, followed by sonication in toluene at room temperature for 10 min. The wafer was further rinsed with toluene before heating to 135 °C for 1 min. Primed wafers were then cut to 1 cm $\times$ cm pieces and stored in a plastic Petri dish.

Preparation of films: Films were cast from the corresponding 2 *wt.* % solutions in 2-heptanone on pre-cut primed wafer pieces at (i) 500 rpm for 5 s and (ii) 3000 rpm for 30 s (2000 rpm s^{-1}). Developed films were heated on a hot plate at 90 °C for 5 min and rinsed in 0.2 M aqueous TMAH solution for 30 s, followed by rinsing in water for 30 s. Films were scratched with a diamond scribe for film thickness measurements by AFM.

CHAPTER V

CONCLUSIONS

5.1   Research Summary

This work detailed the development of systematic methodologies for the preparation of customized porous materials. A synthetic platform for the functionalization of cyclodextrin and its subsequent inclusion into porous frameworks for advanced applications was outlined, and the synthesis of sacrificial porogenic agents for templating highly tailored pore topographies was established. These groups of techniques encompass a sustainable, scalable, and cost-effective strategy for producing a diverse range of materials with elegant control over their pore geometries, chemical properties, and activities.

Through selective functionalization of naturally derived cyclodextrin-based precursors and judicious choice in small molecule linkers, we were able to design polymeric materials for unique, targeted applications with large concentrations of the active cyclodextrin groups. Cyclodextrin polyimides, derived from aminated cyclodextrin monomers, were developed for molecular separations, and their facile preparation as bulk materials and as thin films were outlined. The robust imide linkages provided a key advantage in the thermal stability of the material, as well as its durability across multiple regeneration cycles. Furthermore, the impressive chemical stability of the material enabled its use in a broad variety of solvents. To date, very few porous

cyclodextrin-based materials, in which the cyclodextrins, themselves, form the scaffold of the material have been reported.[25, 77-78, 93] Moreover, in each reported example, the utilization of the material is severely limited by the lack of any hierarchical structure. The significance of our work is in the demonstration that hierarchically porous materials, of crucial importance to use for separation in flow, could be readily produced from cyclodextrin/linker-only frameworks. We further demonstrated that this hierarchical structure endowed the materials with the ability to simultaneously allow mobility of the eluent and target compound immobilization. This development marks a substantial improvement in the practicability of cyclodextrin-derived materials for commercial-scale separations, both in their cost-effective preparation and operation under continuous flow conditions.

Cyclodextrin polyesters, synthesized from native hydroxylic cyclodextrins, were designed to degrade under physiological conditions, and displayed impressive performance as bioabsorbable, sacrificial carriers for chitosan, a polymeric hemostatic agent. The linkage chemistry of the material, in addition to providing the desired degradation properties, provided carboxylate sites in the material capable of interaction with the ammonium groups of chitosan, and facilitated the assembly of chitosan into nanofibrous mats with high surface areas, therefore increasing their hemostatic efficiency. These examples not only established the efficacy of this synthetic strategy to afford porous scaffolds, but also demonstrated that diverse, advanced functionalities could be targeted through synthetic control of the precursors and resulting linkage chemistry.

Acid-deprotectable, cylindrical bottlebrushes were used as sacrificial porogens to imprint predetermined topographies in thin films. It was demonstrated that these brushes could be cast with a compatible linear matrix polymer into films, followed by acid-deprotection of the brushes and subsequent removal by an aqueous developer. The resulting films exhibited topographies consistent with the selective removal of the brush component when viewed by AFM, indicating that this system may present a method for the tailoring of pore and surface topographies in a chosen host material. The key advantage in this approach, compared with traditional imprinting strategies, is the miscibility of the matrix and porogen. Upon casting, the film morphology is kinetically trapped in its homogeneous state, before chemical modification of the porogens to facilitate their selective removal, yielding access to morphologies not obtainable by immiscible components.

5.2   Scope and Future Directions

These synthetic platforms, individually and collectively, provide a seemingly limitless array of obtainable materials, in both structure and activity. In an advanced implementation, the combination of the two synthetic strategies could allow the construction of cyclodextrin-rich frameworks with intricately tuned hierarchical functionalities. At the molecular level, functionalization of the cyclodextrins and their linkages would provide finely tuned chemical-selective activities, while macromolecularly imprinted pores would provide shape-selective peremeabilities. The

sacrificial nature of the porogens would render the cyclodextrin-concentration in the resulting material unaffected, maintaining the maximized effect of the cyclodextrins while offering the ability to provide additional mechanisms of activity within the material.

CDPI is an excellent case study for how this synthetic platform could be applied to produce porous, cyclodextrin-based materials with finely tuned activities on the molecular level. In the synthesis of the aminated cyclodextrin precursor, two intermediate products are first prepared: a halogenated derivative and the azide-functionalized derivative. The halogenated cyclodextrin allows for the installation of a wide-range of functional groups through nucleophilic attack. Their facile conversion to azide groups further allows functionalization through the Huisgen 1,3-dipolar cycloaddition, termed a "click" reaction for its simplicity of preparation and large thermodynamic driving force.[147] Alternatively, the aminated derivative, itself, provides the cyclodextrin with strong nucleophilic groups, allowing the installation of functionalities with electrophilic moieties. By these means, a wide breadth of functional cyclodextrin polymer precursors can be designed and prepared. As it was demonstrated that only *ca*. 5.5 amine groups per cyclodextrin were required to form CDPI, *ca*. 1.5 functional groups per cyclodextrin are left available for further functionalization, either through modification to the cyclodextrin precursors, as previously mentioned, or postmodification of the polymer network. In a practical example, stoichiometric control during the reduction of the azide to the amine allows the formation of cyclodextrin derivatives with sufficient amine groups for polymerization, with remaining unreacted

azide groups for postmodification through a heterogeneous azide-alkyne "click" reaction (Figure V.1). To this end, a customizable, porous cyclodextrin framework is produced without the need for any additional synthetic steps during preparation of the precursor.
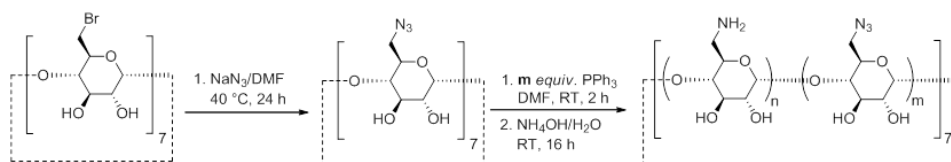
Figure V.1. Synthetic overview of an azide-amine-functionalized cyclodextrin derivative with stoichiometric control.

Subsequent polymerization of the azide-amine-functionalized cyclodextrin yields a porous material analogous to CDPI with free azide groups distributed throughout the network. Functional groups can then be installed (Figure V.2) to either precisely tune the selectivity of the cyclodextrins,[38] or to install additional modes of action, *e.g.* targeting ligands for metals.[148]
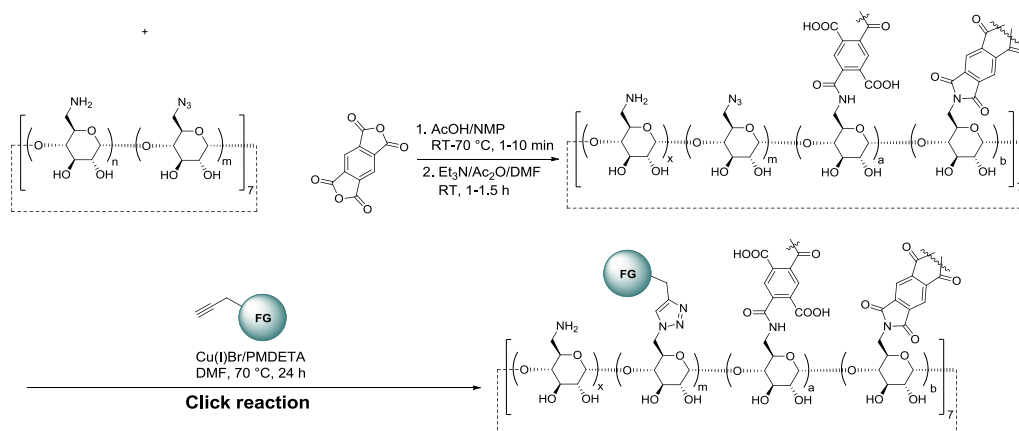
Figure V.2. Preparation of CDPI-N_3 and subsequent installation of functional groups (FG) through "click" chemistry.

In addition to accessorizing these materials with individual functional groups, this approach could also enable the formation of "smart" materials, *e.g.* slide-ring gels,[149-152] by the threading of a compatible, alkyne-functionalized linear polymer, followed by cross-linking through the azide-alkyne "click" reaction (Figure V.3). In addition to the interesting dynamic and robust mechanical properties, this approach may offer a method to process CDPI into higher density materials with reduced macroporosity. Though the macroporosity of CDPI for separation-based applications was desired to provide mobility of the mobile phase through the material, it may be unnecessary and volume-inefficient in other applications. In insulation-based applications, for example, porous gels can be milled into small particles and compressed to improve their performance.[153] This insulation enhancement is achieved by reducing the relative amount of macroporosity in the material, which allows heat flow by convection, while leaving the mesoporosity, which provides the primary insulating activity. The threading and cross-linking of milled CDPI may provide a way to reform the insoluble particles to enable processing by mold and film casting for insulating films, coatings, and specialty packaging.

Figure V.3. Synthesis of slide-ring CDPI gels, in which linear poly(ethylene oxide) (red) is threaded through the cavity of the cyclodextrin before immobilization by cross-linking.

Control of the linkage chemistry in these cyclodextrin-based frameworks is yet another exciting way to introduce new capabilities to these materials and augment the scope of their use. It was demonstrated, in this work, that base-labile linkages were efficacious for biocompatible wound dressings, but there are endless additional possibilities available. Acid-labile linkages could impart these materials with the ability to act as positive tone photopatternable materials for nanodielectric applications. Linkages that degrade under light could be employed for photodegradable materials, or linkages that cross-link under light for photocurable materials. Dynamic linkages, *e.g.* β-hydroxy esters,[154] may introduce the possibility for self-healing properties. Furthermore, as we demonstrated that the geometry of the cross-linker and resulting flexibility of the linkages played a central role in the resulting morphology, diverse pore structures may be accessible merely by the choice in cross-linker. Hence, this synthetic platform provides a powerful, dynamic method for the design and preparation of cyclodextrin-based porous materials with predetermined chemical properties and activities.

The use of tailored polymeric porogens provides another systematic synthetic approach to the realization of materials with predetermined pore topographies and permeabilities. The templating of an inert matrix polymer with sacrificial cylindrical bottlebrush polymers was investigated as a straightforward proof-of-concept, however, as with the cyclodextrin-based materials, this synthetic platform offers immense potential in accessing materials with unique, tailored topography and function beyond what was explicitly demonstrated. A wealth of polymeric architectures, and therefore

corresponding pore geometries, are available through controlled polymerization techniques—from dumbbell-shaped[155] and cyclic brushes,[156] to complex nanostructures with three-dimensional, light-mediated control.[157] Furthermore, the spatial-specific inclusion of surface directing groups, as demonstrated previously in our group,[140-141] can be applied to enable the confinement of features to the surface of films for nanocorrugated materials, or to induce vertical alignment of domains for permeable films with nanoporous channels.

In conclusion, the developed synthetic methodologies described herein present an expansive approach to the preparation of materials with intricately designed pore topographies and functionalities. This all-encompassing set of techniques offer a strategy to achieve desired chemical properties and activities on a molecular level, while enabling control over the network architecture and topography—yielding advanced materials that are deterministically hierarchical in both form and function.

REFERENCES

1.   Zeldovich, Y. B.; Einasto, J.; Shandarin, S. F., Giant voids in the Universe. *Nature* **1982,** *300* (5891), 407-413.

2.   Mann, R. B.; Morris, M. S., Classical models of subatomic particles. *Phys. Lett. A* **1993,** *181* (6), 443-445.

3.   Cadman, J.; Zhou, S.; Chen, Y.; Li, Q., Cuttlebone: Characterisation, application and development of biomimetic materials. *J. Bionic Eng.* **2012,** *9* (3), 367-376.

4.   Ma, Y.; Tong, W.; Zhou, H.; Suib, S. L., A review of zeolite-like porous materials. *Micropor. Mesorpor. Mat.* **2000,** *37* (1), 243-252.

5.   Collins, R. T.; Fauchet, P. M.; Tischler, M. A., Porous Silicon: From Luminescence to LEDs. *Phys. Today* **1997,** *50* (1), 24-31.

6.   Yang, H.; Xu, Z.; Fan, M.; Gupta, R.; Slimane, R. B.; Bland, A. E.; Wright, I., Progress in carbon dioxide separation and capture: A review. *J. Environ. Sci. (China)* **2008,** *20* (1), 14-27.

7.   Nakanishi, K.; Tanaka, N., Sol–Gel with Phase Separation. Hierarchically Porous Materials Optimized for High-Performance Liquid Chromatography Separations. *Acc. Chem. Res.* **2007,** *40* (9), 863-873.

8.   Morris, R. E.; Wheatley, P. S., Gas Storage in Nanoporous Materials. *Angew. Chem. Int. Ed.* **2008,** *47* (27), 4966-4981.

9.   Makal, T. A.; Li, J.-R.; Lu, W.; Zhou, H.-C., Methane storage in advanced porous materials. *Chem. Soc. Rev.* **2012,** *41* (23), 7761-7779.

10.   Thomas, K. M., Hydrogen adsorption and storage on porous materials. *Catal. Today* **2007,** *120* (3), 389-398.

11.   Li, Y.; Fu, Z.-Y.; Su, B.-L., Hierarchically Structured Porous Materials for Energy Conversion and Storage. *Adv. Funct. Mater.* **2012,** *22* (22), 4634-4667.

12.   Anglin, E. J.; Cheng, L.; Freeman, W. R.; Sailor, M. J., Porous silicon in drug delivery devices and materials. *Adv. Drug Deliv. Rev.* **2008,** *60* (11), 1266-1277.

13.   Adebajo, M. O.; Frost, R. L.; Kloprogge, J. T.; Carmody, O.; Kokot, S., Porous Materials for Oil Spill Cleanup: A Review of Synthesis and Absorbing Properties. *J. Porous Mat.* **2003,** *10* (3), 159-170.

14.   Brody, A. L.; Bugusu, B.; Han, J. H.; Sand, C. K.; McHugh, T. H., Scientific Status Summary. *J. Food Sci.* **2008,** *73* (8), R107-R116.

15.   Yurkov, A. L.; Aksel'rod, L. M., Properties of Heat-Insulating Materials (A Review). *Refract. Ind. Ceram.* **2005,** *46* (3), 170-174.

16.   Maex, K.; Baklanov, M. R.; Shamiryan, D.; lacopi, F.; Brongersma, S. H.; Yanovitskaya, Z. S., Low dielectric constant materials for microelectronics. *J. Appl. Phys.* **2003,** *93* (11), 8793-8841.

17.   Zhou, H.-C.; Long, J. R.; Yaghi, O. M., Introduction to Metal–Organic Frameworks. *Chem. Rev.* **2012,** *112* (2), 673-674.

18.   Côté, A. P.; Benin, A. I.; Ockwig, N. W.; Keeffe, M.; Matzger, A. J.; Yaghi, O. M., Porous, Crystalline, Covalent Organic Frameworks. *Science* **2005,** *310* (5751), 1166.

19.   Mastalerz, M., The Next Generation of Shape-Persistant Zeolite Analogues: Covalent Organic Frameworks. *Angew. Chem. Int. Ed.* **2008,** *47* (3), 445-447.

20.   McKeown, N. B.; Budd, P. M., Polymers of intrinsic microporosity (PIMs): organic materials for membrane separations, heterogeneous catalysis and hydrogen storage. *Chem. Soc. Rev.* **2006,** *35* (8), 675-683.

21.   Schmidt, R. H.; Haupt, K., Molecularly Imprinted Polymer Films with Binding Properties Enhanced by the Reaction-Induced Phase Separation of a Sacrificial Polymeric Porogen. *Chem. Mater.* **2005,** *17* (5), 1007-1016.

22.   Kowalewski, T.; Tsarevsky, N. V.; Matyjaszewski, K., Nanostructured Carbon Arrays from Block Copolymers of Polyacrylonitrile. *J. Am. Chem. Soc.* **2002,** *124* (36), 10632-10633.

23.   Sauceau, M.; Fages, J.; Common, A.; Nikitine, C.; Rodier, E., New challenges in polymer foaming: A review of extrusion processes assisted by supercritical carbon dioxide. *Prog. Polym. Sci.* **2011,** *36* (6), 749-766.

24.   Vasilev, K.; Britcher, L.; Casanal, A.; Griesser, H. J., Solvent-Induced Porosity in Ultrathin Amine Plasma Polymer Coatings. *J. Phys. Chem. B* **2008,** *112* (35), 10915-10921.

25.   Alsbaiee, A.; Smith, B. J.; Xiao, L.; Ling, Y.; Helbling, D. E.; Dichtel, W. R., Rapid removal of organic micropollutants from water by a porous β-cyclodextrin polymer. *Nature* **2016,** *529* (7585), 190-194.

26.   Alzate-Sánchez, D. M.; Smith, B. J.; Alsbaiee, A.; Hinestroza, J. P.; Dichtel, W. R., Cotton Fabric Functionalized with a β-Cyclodextrin Polymer Captures Organic Pollutants from Contaminated Air and Water. *Chem. Mater.* **2016,** *28* (22), 8340-8346.

27.   Marques, H. M. C., A review on cyclodextrin encapsulation of essential oils and volatiles. *Flavour Fragr. J.* **2010,** *25* (5), 313-326.

28.   Schneiderman, E.; Stalcup, A. M., Cyclodextrins: a versatile tool in separation science. *J. Chromatogr. B* **2000,** *745* (1), 83-102.

29.   Rosa dos Santos, J.-F.; Alvarez-Lorenzo, C.; Silva, M.; Balsa, L.; Couceiro, J.; Torres-Labandeira, J.-J.; Concheiro, A., Soft contact lenses functionalized with pendant cyclodextrins for controlled drug delivery. *Biomaterials* **2009,** *30* (7), 1348-1355.

30.   Ohno, K.; Wong, B.; Haddleton, D. M., Synthesis of well-defined cyclodextrin-core star polymers. *J. Polym. Sci. A* **2001,** *39* (13), 2206-2214.

31.   Stenzel, M. H.; Davis, T. P., Star polymer synthesis using trithiocarbonate functional β-cyclodextrin cores (reversible addition–fragmentation chain-transfer polymerization). *J. Polym. Sci. A* **2002,** *40* (24), 4498-4512.

32.   Renard, E.; Deratani, A.; Volet, G.; Sebille, B., Preparation and characterization of water soluble high molecular weight β-cyclodextrin-epichlorohydrin polymers. *Eur. Polym. J.* **1997,** *33* (1), 49-57.

33.   Kakuta, T.; Takashima, Y.; Nakahata, M.; Otsubo, M.; Yamaguchi, H.; Harada, A., Preorganized Hydrogel: Self-Healing Properties of Supramolecular Hydrogels Formed by Polymerization of Host–Guest-Monomers that Contain Cyclodextrins and Hydrophobic Guest Groups. *Adv. Mater.* **2013,** *25* (20), 2849-2853.

34.   Zhang, J.; Ma, P. X., Cyclodextrin-based supramolecular systems for drug delivery: Recent progress and future perspective. *Adv. Drug Deliv. Rev.* **2013,** *65* (9), 1215-1233.

35.   van de Manakker, F.; Vermonden, T.; van Nostrum, C. F.; Hennink, W. E., Cyclodextrin-Based Polymeric Materials: Synthesis, Properties, and Pharmaceutical/Biomedical Applications. *Biomacromolecules* **2009,** *10* (12), 3157-3175.

36.   Nepogodiev, S. A.; Stoddart, J. F., Cyclodextrin-Based Catenanes and Rotaxanes. *Chem. Rev.* **1998,** *98* (5), 1959-1976.

37.   Murakami, T.; Schmidt, B. V. K. J.; Brown, H. R.; Hawker, C. J., One-Pot "Click" Fabrication of Slide-Ring Gels. *Macromolecules* **2015,** *48* (21), 7774-7781.

38.   Wenz, G.; Strassnig, C.; Thiele, C.; Engelke, A.; Morgenstern, B.; Hegetschweiler, K., Recognition of Ionic Guests by Ionic β-Cyclodextrin Derivatives. *Chem. Eur. J.* **2008,** *14* (24), 7202-7211.

39.   Ree, M.; Yoon, J.; Heo, K., Imprinting well-controlled closed-nanopores in spin-on polymeric dielectric thin films. *J. Mater. Chem.* **2006,** *16* (7), 685-697.

40.   Maidenberg, D. A.; Volksen, W.; Miller, R. D.; Dauskardt, R. H., Toughening of nanoporous glasses using porogen residuals. *Nat. Mater.* **2004,** *3*, 464.

41.   Dubois, G.; Volksen, W.; Magbitang, T.; Sherwood, M. H.; Miller, R. D.; Gage, D. M.; Dauskardt, R. H., Superior mechanical properties of dense and porous organic/inorganic hybrid thin films. *J. Sol-Gel Sci. Technol.* **2008,** *48* (1-2), 187-193.

42.   Kim, S.; Cho, J.; Char, K., Thermally Stable Antireflective Coatings Based on Nanoporous Organosilicate Thin Films. *Langmuir* **2007,** *23* (12), 6737-6743.

43.   Raut, H. K.; Ganesh, V. A.; Nair, A. S.; Ramakrishna, S., Anti-reflective coatings: A critical, in-depth review. *Energy Environ. Sci.* **2011,** *4* (10), 3779-3804.

44.   Azzaroni, O.; Lau, K. H. A., Layer-by-layer assemblies in nanoporous templates: nano-organized design and applications of soft nanotechnology. *Soft Matter* **2011,** *7* (19), 8709-8724.

45.   Bang, J.; Kim, S. H.; Drockenmuller, E.; Misner, M. J.; Russell, T. P.; Hawker, C. J., Defect-Free Nanoporous Thin Films from ABC Triblock Copolymers. *J. Am. Chem. Soc.* **2006,** *128* (23), 7622-7629.

46.   Park, S.; Kim, B.; Wang, J. Y.; Russell, T. P., Fabrication of Highly Ordered Silicon Oxide Dots and Stripes from Block Copolymer Thin Films. *Adv. Mater.* **2008,** *20* (4), 681-685.

47.   Jung, Y. S.; Ross, C. A., Well-Ordered Thin-Film Nanopore Arrays Formed Using a Block-Copolymer Template. *Small* **2009,** *5* (14), 1654-1659.

48.   Hedrick, J. L.; Miller, R. D.; Hawker, C. J.; Carter, K. R.; Volksen, W.; Yoon, D. Y.; Trollsås, M., Templating Nanoporosity in Thin-Film Dielectric Insulators. *Adv. Mater.* **1998,** *10* (13), 1049-1053.

49.   Li, S.; Li, Z.; Yan, Y., Ultra-Low-k Pure-Silica Zeolite MFI Films Using Cyclodextrin as Porogen. *Adv. Mater.* **2003,** *15* (18), 1528-1531.

50.   Yim, J. H.; Seon, J. B.; Jeong, H. D.; Pu, L. S.; Baklanov, M. R.; Gidley, D. W., Morphological Control of Nanoporous Films by the Use of Functionalized Cyclodextrins as Porogens. *Adv. Funct. Mater.* **2004,** *14* (3), 277-282.

51.	Yim, J.-H.; Baklanov, M. R.; Gidley, D. W.; Peng, H.; Jeong, H.-D.; Sun Pu, L., Pore Structure of Modified Cyclic Silsesquioxane Thin Films Made Porous Using a Cyclodextrins-Based Porogen. *J. Phys. Chem. B* **2004,** *108* (26), 8953-8959.

52.	Heise, A.; Nguyen, C.; Malek, R.; Hedrick, J. L.; Frank, C. W.; Miller, R. D., Starlike Polymeric Architectures by Atom Transfer Radical Polymerization: Templates for the Production of Low Dielectric Constant Thin Films. *Macromolecules* **2000,** *33* (7), 2346-2354.

53.	Hedstrom, J. A.; Toney, M. F.; Huang, E.; Kim, H.-C.; Volksen, W.; Magbitang, T.; Miller, R. D., Pore Morphologies in Disordered Nanoporous Thin Films. *Langmuir* **2004,** *20* (5), 1535-1538.

54.	Ibn-Elhaj, M.; Schadt, M., Optical polymer thin films with isotropic and anisotropic nano-corrugated surface topologies. *Nature* **2001,** *410*, 796.

55.	Lin, Q.; Steinhäusler, T.; Simpson, L.; Wilder, M.; Medeiros, D. R.; Willson, C. G.; Havard, J.; Fréchet, J. M. J., A Water-Castable, Water-Developable Chemically Amplified Negative-Tone Resist. *Chem. Mater.* **1997,** *9* (8), 1725-1730.

56.	Del Valle, E. M. M., Cyclodextrins and their uses: a review. *Process Biochem.* **2004,** *39* (9), 1033-1046.

57.	Crini, G., Non-conventional low-cost adsorbents for dye removal: A review. *Bioresour. Technol.* **2006,** *97* (9), 1061-1085.

58.	Crini, G., Recent developments in polysaccharide-based materials used as adsorbents in wastewater treatment. *Prog. Polym. Sci.* **2005,** *30* (1), 38-70.

59.	Crini, G.; Bertini, S.; Torri, G.; Naggi, A.; Sforzini, D.; Vecchi, C.; Janus, L.; Lekchiri, Y.; Morcellet, M., Sorption of aromatic compounds in water using insoluble cyclodextrin polymers. *J. Appl. Polym. Sci.* **1998,** *68* (12), 1973-1978.

60.	Crini, G., Studies on adsorption of dyes on beta-cyclodextrin polymer. *Bioresour. Technol.* **2003,** *90* (2), 193-198.

61.	Crini, G.; Morcellet, M., Synthesis and applications of adsorbents containing cyclodextrins. *J. Sep. Sci.* **2002,** *25* (13), 789-813.

62.	Morin-Crini, N.; Crini, G., Environmental applications of water-insoluble β-cyclodextrin–epichlorohydrin polymers. *Prog. Polym. Sci.* **2013,** *38* (2), 344-368.

63.	Sharma, N.; Baldi, A., Exploring versatile applications of cyclodextrins: an overview. *Drug Deliv.* **2016,** *23* (3), 729-747.

64.	Yuen, F. K.; Hameed, B. H., Recent developments in the preparation and regeneration of activated carbons by microwaves. *Adv. Colloid Interface Sci.* **2009,** *149* (1), 19-27.

65.	Foo, K. Y.; Hameed, B. H., Insights into the modeling of adsorption isotherm systems. *Chem. Eng. J.* **2010,** *156* (1), 2-10.

66.	Li, Y.; Lu, P.; Cheng, J.; Zhu, X.; Guo, W.; Liu, L.; Wang, Q.; He, C.; Liu, S., Novel microporous β-cyclodextrin polymer as sorbent for solid-phase extraction of bisphenols in water samples and orange juice. *Talanta* **2018,** *187*, 207-215.

67.	Yamasaki, A.; Iwatsubo, T.; Masuoka, T.; Mizoguchi, K., Pervaporation of ethanol/water through a poly(vinyl alcohol)/cyclodextrin (PVA/CD) membrane. *J. Membr. Sci.* **1994,** *89* (1), 111-117.

68.	Kusumocahyo, S. P.; Kanamori, T.; Sumaru, K.; Iwatsubo, T.; Shinbo, T., Pervaporation of xylene isomer mixture through cyclodextrins containing polyacrylic acid membranes. *J. Membr. Sci.* **2004,** *231* (1), 127-132.

69.	Jiang, L. Y.; Chung, T. S., β-Cyclodextrin containing Matrimid® sub-nanocomposite membranes for pervaporation application. *J. Membr. Sci.* **2009,** *327* (1), 216-225.

70.	Jiang, L. Y.; Chung, T. S., Homogeneous polyimide/cyclodextrin composite membranes for pervaporation dehydration of isopropanol. *J. Membr. Sci.* **2010,** *346* (1), 45-58.

71.	Adams, F. V.; Nxumalo, E. N.; Krause, R. W. M.; Hoek, E. M. V.; Mamba, B. B., Preparation and characterization of polysulfone/β-cyclodextrin polyurethane composite nanofiltration membranes. *J. Membr. Sci.* **2012,** *405-406*, 291-299.

72.	Mbuli, B. S.; Dlamini, D. S.; Nxumalo, E. N.; Krause, R. W.; Pillay, V. L.; Oren, Y.; Linder, C.; Mamba, B. B., Preparation and characterization of thin film composite membranes modified with amine-functionalized β-cyclodextrins. *J. Appl. Polym. Sci.* **2013,** *129* (2), 549-558.

73.	Mbuli, B. S.; Nxumalo, E. N.; Mhlanga, S. D.; Krause, R. W.; Pillay, V. L.; Oren, Y.; Linder, C.; Mamba, B. B., Development of antifouling polyamide thin-film composite membranes modified with amino-cyclodextrins and diethylamino-cyclodextrins for water treatment. *J. Appl. Polym. Sci.* **2014,** *131* (8), 40109.

74.	Yu, Z.; Pan, Y.; He, Y.; Zeng, G.; Shi, H.; Di, H., Preparation of a novel anti-fouling [small beta]-cyclodextrin-PVDF membrane. *RSC Adv.* **2015,** *5* (63), 51364-51370.

75.   Rölling, P.; Lamers, M.; Staudt, C., Cross-linked membranes based on acrylated cyclodextrins and polyethylene glycol dimethacrylates for aromatic/aliphatic separation. *J. Membr. Sci.* **2010,** *362* (1), 154-163.

76.   Adams, F. V.; Nxumalo, E. N.; Krause, R. W. M.; Hoek, E. M. V.; Mamba, B. B., Application of polysulfone/cyclodextrin mixed-matrix membranes in the removal of natural organic matter from water. *Phys. Chem. Earth* **2014,** *67*, 71-78.

77.   Villalobos, L. F.; Huang, T.; Peinemann, K.-V., Cyclodextrin Films with Fast Solvent Transport and Shape-Selective Permeability. *Adv. Mater.* **2017,** *29* (26), 1606641.

78.   Jiangtao, L.; Dan, H.; Yu, Z.; Susilo, J.; Tai-Shung, C., Precise Molecular Sieving Architectures with Janus Pathways for Both Polar and Nonpolar Molecules. *Adv. Mater.* **2018,** *30* (11), 1705933.

79.   Leventis, N.; Sotiriou-Leventis, C.; Mohite, D. P.; Larimore, Z. J.; Mang, J. T.; Churu, G.; Lu, H., Polyimide Aerogels by Ring-Opening Metathesis Polymerization (ROMP). *Chem. Mater.* **2011,** *23* (8), 2250-2261.

80.   Guo, H.; Meador, M. A. B.; McCorkle, L.; Quade, D. J.; Guo, J.; Hamilton, B.; Cakmak, M.; Sprowl, G., Polyimide Aerogels Cross-Linked through Amine Functionalized Polyoligomeric Silsesquioxane. *ACS Appl. Mater. Interfaces* **2011,** *3* (2), 546-552.

81.   Meador, M. A. B.; Malow, E. J.; Silva, R.; Wright, S.; Quade, D.; Vivod, S. L.; Guo, H.; Guo, J.; Cakmak, M., Mechanically Strong, Flexible Polyimide Aerogels Cross-Linked with Aromatic Triamine. *ACS Appl. Mater. Interfaces* **2012,** *4* (2), 536-544.

82.   Meador, M. A. B.; Wright, S.; Sandberg, A.; Nguyen, B. N.; Van Keuls, F. W.; Mueller, C. H.; Rodríguez-Solís, R.; Miranda, F. A., Low Dielectric Polyimide Aerogels As Substrates for Lightweight Patch Antennas. *ACS Appl. Mater. Interfaces* **2012,** *4* (11), 6346-6353.

83.   Meador, M. A. B.; Alemán, C. R.; Hanson, K.; Ramirez, N.; Vivod, S. L.; Wilmoth, N.; McCorkle, L., Polyimide Aerogels with Amide Cross-Links: A Low Cost Alternative for Mechanically Strong Polymer Aerogels. *ACS Appl. Mater. Interfaces* **2015,** *7* (2), 1240-1249.

84.   Liaw, D.-J.; Wang, K.-L.; Huang, Y.-C.; Lee, K.-R.; Lai, J.-Y.; Ha, C.-S., Advanced polyimide materials: Syntheses, physical properties and applications. *Prog. Polym. Sci.* **2012,** *37* (7), 907-974.

85.   Vanherck, K.; Koeckelberghs, G.; Vankelecom, I. F. J., Crosslinking polyimides for membrane applications: A review. *Prog. Polym. Sci.* **2013,** *38* (6), 874-896.

86.   Ashton, P. R.; Königer, R.; Stoddart, J. F.; Alker, D.; Harding, V. D., Amino Acid Derivatives of β-Cyclodextrin. *J. Org. Chem.* **1996,** *61* (3), 903-908.

87.   Cryan, S.-A.; Holohan, A.; Donohue, R.; Darcy, R.; O'Driscoll, C. M., Cell transfection with polycationic cyclodextrin vectors. *Eur. J. Pharm. Sci.* **2004,** *21* (5), 625-633.

88.   Hbaieb, S.; Kalfat, R.; Chevalier, Y.; Amdouni, N.; Parrot-Lopez, H., Influence of the substitution of β-cyclodextrins by cationic groups on the complexation of organic anions. *Mater. Sci. Eng. C.* **2008,** *28* (5), 697-704.

89.   Kanagaraj, K.; Pitchumani, K., Solvent-free multicomponent synthesis of pyranopyrazoles: per-6-amino-β-cyclodextrin as a remarkable catalyst and host. *Tetrahedron Lett.* **2010,** *51* (25), 3312-3316.

90.   Nag, S.; Duarte, L.; Bertrand, E.; Celton, V.; Castro, M.; Choudhary, V.; Guegan, P.; Feller, J.-F., Ultrasensitive QRS made by supramolecular assembly of functionalized cyclodextrins and graphene for the detection of lung cancer VOC biomarkers. *J. Mater. Chem. B* **2014,** *2* (38), 6571-6579.

91.   Hirotsu, T.; Higashi, T.; Abu Hashim, I. I.; Misumi, S.; Wada, K.; Motoyama, K.; Arima, H., Self-Assembly PEGylation Retaining Activity (SPRA) Technology via a Host–Guest Interaction Surpassing Conventional PEGylation Methods of Proteins. *Mol. Pharm.* **2017,** *14* (2), 368-376.

92.   Pereira, G.; Huin, C.; Morariu, S.; Bennevault-Celton, V.; Guégan, P., Synthesis of Poly(2-methyl-2-oxazoline) Star Polymers with a β-Cyclodextrin Core. *Aust. J. Chem.* **2012,** *65* (8), 1145-1155.

93.   Wang, R.-Q.; Wei, X.-B.; Feng, Y.-Q., β-Cyclodextrin Covalent Organic Framework for Selective Molecular Adsorption. *Chem. Eur. J.* **2018,** *24* (43), 10979-10983.

94.   Zheng, Y.; Hashidzume, A.; Takashima, Y.; Yamaguchi, H.; Harada, A., Macroscopic Observations of Molecular Recognition: Discrimination of the Substituted Position on the Naphthyl Group by Polyacrylamide Gel Modified with β-Cyclodextrin. *Langmuir* **2011,** *27* (22), 13790-13795.

95.   Kakuta, T.; Takashima, Y.; Harada, A., Highly Elastic Supramolecular Hydrogels Using Host–Guest Inclusion Complexes with Cyclodextrins. *Macromolecules* **2013,** *46* (11), 4575-4579.

96.   Miura, Y.; Narumi, A.; Matsuya, S.; Satoh, T.; Duan, Q.; Kaga, H.; Kakuchi, T., Synthesis of well-defined AB20-type star polymers with cyclodextrin-core by combination of NMP and ATRP. *J. Polym. Sci. A* **2005,** *43* (18), 4271-4279.

97.   Duarte, L.; Nag, S.; Castro, M.; Zaborova, E.; Ménand, M.; Sollogoub, M.; Bennevault, V.; Feller, J.-F.; Guégan, P., Chemical Sensors Based on New Polyamides Biobased on (Z) Octadec-9-Enedioic Acid and β-Cyclodextrin. *Macromol. Chem. Phys.* **2016,** *217* (14), 1620-1628.

98.   Xie, K.; Liu, J. G.; Zhou, H. W.; Zhang, S. Y.; He, M. H.; Yang, S. Y., Soluble fluoro-polyimides derived from 1,3-bis(4-amino-2-trifluoromethyl- phenoxy) benzene and dianhydrides. *Polymer* **2001,** *42* (17), 7267-7274.

99.   da Silva Lacerda, V.; López-Sotelo, J. B.; Correa-Guimarães, A.; Hernández-Navarro, S.; Sánchez-Báscones, M.; Navas-Gracia, L. M.; Martín-Ramos, P.; Martín-Gil, J., Rhodamine B removal with activated carbons obtained from lignocellulosic waste. *J. Environ. Manage.* **2015,** *155*, 67-76.

100.   Zhu, X.; An, S.; Liu, Y.; Hu, J.; Liu, H.; Tian, C.; Dai, S.; Yang, X.; Wang, H.; Abney, C. W.; Dai, S., Efficient removal of organic dye pollutants using covalent organic frameworks. *AIChE J.* **2017,** *63* (8), 3470-3478.

101.   Sobrino, J.; Shafi, S., Timing and causes of death after injuries. *Proc. (Bayl. Univ. Med. Cent.)* **2013,** *26* (2), 120-123.

102.   Florence, C.; Haegerich, T.; Simon, T.; Zhou, C.; Luo, F., Estimated Lifetime Medical and Work-Loss Costs of Emergency Department–Treated Nonfatal Injuries — United States, 2013. *MMWR* **2015,** *64* (38), 1078-1082.

103.   Wedmore, I.; McManus, J. G.; Pusateri, A. E.; Holcomb, J. B., A special report on the chitosan-based hemostatic dressing. *J. Trauma Acute Care Surg.* **2006,** *60* (3), 655-658.

104.   Jayakumar, R.; Prabaharan, M.; Sudheesh Kumar, P. T.; Nair, S. V.; Tamura, H., Biomaterials based on chitin and chitosan in wound dressing applications. *Biotechnol. Adv.* **2011,** *29* (3), 322-337.

105.   Brown, M. A.; Daya, M. R.; Worley, J. A., Experience with Chitosan Dressings in a Civilian EMS System. *J. Emerg. Med.* **2009,** *37* (1), 1-7.

106.   Gegel, B.; Burgert, J.; Cooley, B.; MacGregor, J.; Myers, J.; Calder, S.; Luellen, R.; Loughren, M.; Johnson, D., The Effects of BleedArrest, Celox, and TraumaDex on Hemorrhage Control in a Porcine Model. *J. Surg. Res.* **2010,** *164* (1), 125-129.

107.   Lechner, R.; Helm, M.; Mueller, M.; Wille, T.; Friemert, B., Efficacy of Hemostatic Agents in Humans With Rotational Thromboelastometry: An in-vitro Study. *Mil. Med.* **2016,** *181* (8), 907-912.

108.   Zietlow, S.; Morris, D.; Berns, K.; Jenkins, D.; Zietlow, J., Prehospital Use of Hemostatic Bandages/Tourniquets; Translation From Military Experience to Implementation in Civilian Trauma Care. *Air Med. J.* **2014,** *33* (5), 209.

109.   Hickman, D. A.; Pawlowski, C. L.; Sekhon, U. D. S.; Marks, J.; Gupta, A. S., Biomaterials and Advanced Technologies for Hemostatic Management of Bleeding. *Adv. Mater.* **2017,** *30* (4), 1700859.

110.   Xu, H.; Fang, Z.; Tian, W.; Wang, Y.; Ye, Q.; Zhang, L.; Cai, J., Green Fabrication of Amphiphilic Quaternized β-Chitin Derivatives with Excellent Biocompatibility and Antibacterial Activities for Wound Healing. *Adv. Mater.* **2018,** *30* (29), 1801100.

111.   Pan, M.; Tang, Z.; Tu, J.; Wang, Z.; Chen, Q.; Xiao, R.; Liu, H., Porous chitosan microspheres containing zinc ion for enhanced thrombosis and hemostasis. *Mater. Sci. Eng. C.* **2018,** *85*, 27-36.

112.   Englehart, M. S.; Cho, S. D.; Tieu, B. H.; Morris, M. S.; Underwood, S. J.; Karahan, A.; Muller, J. P.; Differding, J. A.; Farrell, D. H.; Schreiber, M. A., A Novel Highly Porous Silica and Chitosan-Based Hemostatic Dressing Is Superior to HemCon and Gauze Sponges. *J. Trauma Acute Care Surg.* **2008,** *65* (4), 884-892.

113.   Szatmári, V., Chitosan hemostatic dressing for control of hemorrhage from femoral arterial puncture site in dogs. *J. Vet. Sci.* **2015,** *16* (4), 517-523.

114.   Wang, A. Y.; Rafalko, J.; MacDonald, M.; Ming, X.; Kocharian, R., Absorbable Hemostatic Aggregates. *ACS Biomater. Sci. Eng.* **2017,** *3* (12), 3675-3686.

115.   MacDonald, M. H.; Wang, A. Y.; Clymer, J. W.; Hutchinson, R. W.; Kocharian, R., An in vivo comparison of the efficacy of hemostatic powders, using two porcine bleeding models. *Med. Devices (Auckl.)* **2017,** *10*, 273-279.

116.   Jiang, X.; Wang, Y.; Fan, D.; Zhu, C.; Liu, L.; Duan, Z., A novel human-like collagen hemostatic sponge with uniform morphology, good biodegradability and biocompatibility. *J. Biomater. Appl.* **2017,** *31* (8), 1099-1107.

117.   Bennett, B. L.; Littlejohn, L., Review of New Topical Hemostatic Dressings for Combat Casualty Care. *Mil. Med.* **2014,** *179* (5), 497-514.

118.   Chen, C.; Liu, Y.; Wang, H.; Chen, G.; Wu, X.; Ren, J.; Zhang, H.; Zhao, Y., Multifunctional Chitosan Inverse Opal Particles for Wound Healing. *ACS Nano* **2018**.

119.   Zhang, Y.; Zhang, M., Three-dimensional macroporous calcium phosphate bioceramics with nested chitosan sponges for load-bearing bone implants. *J. Biomed. Mater. Res.* **2002,** *61* (1), 1-8.

120.   Torres-Rendon, J. G.; Femmer, T.; De Laporte, L.; Tigges, T.; Rahimi, K.; Gremse, F.; Zafarnia, S.; Lederle, W.; Ifuku, S.; Wessling, M.; Hardy, J. G.; Walther, A., Bioactive Gyroid Scaffolds Formed by Sacrificial Templating of Nanocellulose and Nanochitin Hydrogels as Instructive Platforms for Biomimetic Tissue Engineering. *Adv. Mater.* **2015,** *27* (19), 2989-2995.

121.   Sukul, M.; Ventura, R. D.; Bae, S. H.; Choi, H. J.; Lee, S. Y.; Lee, B. T., Plant-derived oxidized nanofibrillar cellulose-chitosan composite as an absorbable hemostat. *Mater. Lett.* **2017,** *197*, 150-155.

122.   Dey, A.; Kamat, A.; Nayak, S.; Danino, D.; Kesselman, E.; Dandekar, P.; Jain, R., Role of proton balance in formation of self-assembled chitosan nanoparticles. *Colloids Surf. B* **2018,** *166*, 127-134.

123.   Leonhardt, E. E.; Meador, M. A. B.; Wooley, K. L., β-Cyclodextrin-Derived Monolithic, Hierarchically Porous Polyimides Designed for Versatile Molecular Separation Applications. *Chem. Mater.* **2018,** *30* (18), 6226-6230.

124.   Berger, J.; Reist, M.; Mayer, J. M.; Felt, O.; Peppas, N. A.; Gurny, R., Structure and interactions in covalently and ionically crosslinked chitosan hydrogels for biomedical applications. *Eur. J. Pharm. Biopharm.* **2004,** *57* (1), 19-34.

125.   Lavertu, M.; Filion, D.; Buschmann, M. D., Heat-Induced Transfer of Protons from Chitosan to Glycerol Phosphate Produces Chitosan Precipitation and Gelation. *Biomacromolecules* **2008,** *9* (2), 640-650.

126.   Chenite, A.; Chaput, C.; Wang, D.; Combes, C.; Buschmann, M. D.; Hoemann, C. D.; Leroux, J. C.; Atkinson, B. L.; Binette, F.; Selmani, A., Novel injectable neutral solutions of chitosan form biodegradable gels in situ. *Biomaterials* **2000,** *21* (21), 2155-2161.

127.   Geng, X.; Kwon, O.-H.; Jang, J., Electrospinning of chitosan dissolved in concentrated acetic acid solution. *Biomaterials* **2005,** *26* (27), 5427-5432.

128.   Jayakumar, R.; Prabaharan, M.; Nair, S. V.; Tamura, H., Novel chitin and chitosan nanofibers in biomedical applications. *Biotechnol. Adv.* **2010,** *28* (1), 142-150.

129.   Schiffman, J. D.; Schauer, C. L., Cross-Linking Chitosan Nanofibers. *Biomacromolecules* **2007,** *8* (2), 594-601.

130.   Zhong, C.; Cooper, A.; Kapetanovic, A.; Fang, Z.; Zhang, M.; Rolandi, M., A facile bottom-up route to self-assembled biogenic chitin nanofibers. *Soft Matter* **2010,** *6* (21), 5298-5301.

131.   Rolandi, M.; Rolandi, R., Self-assembled chitin nanofibers and applications. *Adv. Colloid Interface Sci.* **2014,** *207*, 216-222.

132.   Lewis, K. M.; Atlee, H. D.; Mannone, A. J.; Dwyer, J.; Lin, L.; Goppelt, A.; Redl, H., Comparison of Two Gelatin and Thrombin Combination Hemostats in a Porcine Liver Abrasion Model. *J. Invest. Surg.* **2013,** *26* (3), 141-148.

133.   Huang, X.; Sun, Y.; Nie, J.; Lu, W.; Yang, L.; Zhang, Z.; Yin, H.; Wang, Z.; Hu, Q., Using absorbable chitosan hemostatic sponges as a promising surgical dressing. *Int. J. Biol. Macromol.* **2015,** *75*, 322-329.

134.   Luo, M.; Epps, T. H., Directed Block Copolymer Thin Film Self-Assembly: Emerging Trends in Nanopattern Fabrication. *Macromolecules* **2013,** *46* (19), 7567-7579.

135.   Marencic, A. P.; Register, R. A., Controlling Order in Block Copolymer Thin Films for Nanopatterning Applications. *Annu. Rev. Chem. Biomol. Eng.* **2010,** *1* (1), 277-297.

136.   Song, Q.; Jiang, S.; Hasell, T.; Liu, M.; Sun, S.; Cheetham, A. K.; Sivaniah, E.; Cooper, A. I., Porous Organic Cage Thin Films and Molecular-Sieving Membranes. *Adv. Mater.* **2016,** *28* (13), 2629-2637.

137.   Jeong, S.-J.; Kim, J. Y.; Kim, B. H.; Moon, H.-S.; Kim, S. O., Directed self-assembly of block copolymers for next generation nanolithography. *Mater. Today* **2013,** *16* (12), 468-476.

138.   Matsen, M. W.; Bates, F. S., Origins of Complex Self-Assembly in Block Copolymers. *Macromolecules* **1996,** *29* (23), 7641-7644.

139.   Park, S.; Lee, D. H.; Xu, J.; Kim, B.; Hong, S. W.; Jeong, U.; Xu, T.; Russell, T. P., Macroscopic 10-Terabit–per–Square-Inch Arrays from Block Copolymers with Lateral Order. *Science* **2009,** *323* (5917), 1030.

140.   Sun, G.; Cho, S.; Clark, C.; Verkhoturov, S. V.; Eller, M. J.; Li, A.; Pavía-Jiménez, A.; Schweikert, E. A.; Thackeray, J. W.; Trefonas, P.; Wooley, K. L., Nanoscopic Cylindrical Dual Concentric and Lengthwise Block Brush Terpolymers as Covalent Preassembled High-Resolution and High-Sensitivity Negative-Tone Photoresist Materials. *J. Am. Chem. Soc.* **2013,** *135* (11), 4203-4206.

141.   Sun, G.; Cho, S.; Yang, F.; He, X.; Pavía-Sanders, A.; Clark, C.; Raymond, J. E.; Verkhoturov, S. V.; Schweikert, E. A.; Thackeray, J. W.; Trefonas, P.; Wooley, K. L., Advanced photoresist technologies by intricate molecular brush architectures: Diblock brush terpolymer-based positive-tone photoresist materials. *J. Polym. Sci. A* **2015,** *53* (2), 193-199.

142.   Patton, D. L.; Advincula, R. C., A Versatile Synthetic Route to Macromonomers via RAFT Polymerization. *Macromolecules* **2006,** *39* (25), 8674-8683.

143.   Eller, M. J.; Verkhoturov, S. V.; Schweikert, E. A., Testing Molecular Homogeneity at the Nanoscale with Massive Cluster Secondary Ion Mass Spectrometry. *Anal. Chem.* **2016,** *88* (15), 7639-7646.

144.   Eller, M. J.; Vinjamuri, A.; Tomlin, B. E.; Schweikert, E. A., Molecular Colocalization Using Massive Gold Cluster Secondary Ion Mass Spectrometry. *Anal. Chem.* **2018,** *90* (21), 12692-12697.

145.   de Bettencourt-Dias, A.; Rossini, J. S. K., Ligand Design for Luminescent Lanthanide-Containing Metallopolymers. *Inorg. Chem.* **2016,** *55* (20), 9954-9963.

146.   Sanford, M. S.; Love, J. A.; Grubbs, R. H., A Versatile Precursor for the Synthesis of New Ruthenium Olefin Metathesis Catalysts. *Organometallics* **2001,** *20* (25), 5314-5318.

147.   Moses, J. E.; Moorhouse, A. D., The growing applications of click chemistry. *Chem. Soc. Rev.* **2007,** *36* (8), 1249-1262.

148.   Sun, D. T.; Peng, L.; Reeder, W. S.; Moosavi, S. M.; Tiana, D.; Britt, D. K.; Oveisi, E.; Queen, W. L., Rapid, Selective Heavy Metal Removal from Water by a Metal–Organic Framework/Polydopamine Composite. *ACS Cent. Sci.* **2018,** *4* (3), 349-356.

149.   Ito, K., Slide-Ring Materials Using Cyclodextrin. *Chem. Pharm. Bull.* **2017,** *65* (4), 326-329.

150.   Kato, K.; Inoue, K.; Kidowaki, M.; Ito, K., Organic−Inorganic Hybrid Slide-Ring Gels: Polyrotaxanes Consisting of Poly(dimethylsiloxane) and γ-Cyclodextrin and Subsequent Topological Cross-Linking. *Macromolecules* **2009,** *42* (18), 7129-7136.

151.   Kidowaki, M.; Zhao, C.; Kataoka, T.; Ito, K., Thermoreversible sol–gel transition of an aqueous solution of polyrotaxane composed of highly methylated α-cyclodextrin and polyethylene glycol. *ChemComm* **2006,** *39*, 4102-4103.

152.   Katsuno, C.; Konda, A.; Urayama, K.; Takigawa, T.; Kidowaki, M.; Ito, K., Pressure-Responsive Polymer Membranes of Slide-Ring Gels with Movable Cross-Links. *Adv. Mater.* **2013,** *25* (33), 4636-4640.

153.   Gao, T.; Jelle, B. P.; Ihara, T.; Gustavsen, A., Insulating glazing units with silica aerogel granules: The impact of particle size. *Appl. Energ.* **2014,** *128*, 27-34.

154.   Capelot, M.; Montarnal, D.; Tournilhac, F.; Leibler, L., Metal-Catalyzed Transesterification for Healing and Assembling of Thermosets. *J. Am. Chem. Soc.* **2012,** *134* (18), 7664-7667.

155.   Li, A.; Li, Z.; Zhang, S.; Sun, G.; Policarpio, D. M.; Wooley, K. L., Synthesis and Direct Visualization of Dumbbell-Shaped Molecular Brushes. *ACS Macro Lett.* **2012,** *1* (1), 241-245.

156.   Xia, Y.; Boydston, A. J.; Grubbs, R. H., Synthesis and Direct Imaging of Ultrahigh Molecular Weight Cyclic Brush Polymers. *Angew. Chem. Int. Ed.* **2011,** *50* (26), 5882-5885.

157.   Poelma, J. E.; Fors, B. P.; Meyers, G. F.; Kramer, J. W.; Hawker, C. J., Fabrication of Complex Three-Dimensional Polymer Brush Nanostructures through Light-Mediated Living Radical Polymerization. *Angew. Chem. Int. Ed.* **2013,** *52* (27), 6844-6848.